

**Testing general relativity using observations of gravitational
waves from the inspiral, merger and ringdown of
binary black holes**

A Thesis

Submitted to the
Tata Institute of Fundamental Research, Mumbai
for the degree of Doctor of Philosophy
in Physics

by

Abhirup Ghosh

International Centre for Theoretical Sciences
Tata Institute of Fundamental Research
Bangalore
April, 2019

Declaration

This thesis is a presentation of my original research work. Wherever contributions of others are involved, every effort is made to indicate this clearly, with due reference to the literature, and acknowledgement of collaborative research and discussions.

The work was done under the guidance of Professor Parameswaran Ajith, at the International Centre for Theoretical Sciences, Tata Institute of Fundamental Research, Bangalore.



Abhirup Ghosh

In my capacity as supervisor of the candidate's thesis, I certify that the above statements are true to the best of my knowledge.



Parameswaran Ajith

Date: 19 July, 2018

Abstract

This thesis describes a test of General Relativity (GR) in the highly relativistic, strong field regime of gravity using observations of gravitational waves from the inspiral, merger and ringdown of binary black holes (BBHs). The thesis further presents the results of this test on the first gravitational wave observations by Advanced LIGO and Virgo and shows that the observed signals are indeed consistent with the predictions of GR.

In chapters 1 and 2, we provide an overview of the topic of gravitational wave astronomy. Chapter 1 discusses aspects about the generation and detection of gravitational waves, promising sources for interferometric detectors, and information that can be extracted from the observed signals. We end the chapter by discussing all the gravitational wave observations that have been made by the advanced detectors till date, and a look at future detectors. Chapter 2 discusses how we infer the properties of a source from the observed signal and use these observations to test GR. We present an overview of the various tests of GR performed in the last 100 years, including the unique tests facilitated by gravitational wave observations.

In Chapter 3 we discuss the inspiral-merger-ringdown (IMR) consistency test, which involves inferring the mass and spin of the remnant black hole from the inspiral (low-frequency) and the post-inspiral (high-frequency) part of the observed signal independently, and checking for their consistency. Anticipating the large number of detections of BBHs expected in the near future, we show how constraints from a large number of events with modest signal to noise ratios can be combined to produce strong constraints on deviations from GR. Using kludge modified GR waveforms, we demonstrate how this test could identify certain types of deviations from GR if such deviations are present in the signal waveforms. We also study the robustness of this test against reasonable variations of different analysis param-

eters. Finally, Chapter 4 discusses results of the IMR consistency test on the gravitational wave observations, GW₁₅₀₉₁₄, GW₁₇₀₁₀₄ and GW₁₇₀₈₁₄, and how combining information from GW₁₅₀₉₁₄ and GW₁₇₀₁₀₄, has allowed us to put the tightest constraints yet from this test, on the possible deviations from the predictions of GR.

Contents

1	Introduction: Gravitational Waves	9
1.1	Gravitational Waves	9
1.2	Sources	12
1.2.1	Simple order-of-magnitude estimates	13
1.2.2	Burst sources	15
1.2.3	Spinning neutron stars	16
1.2.4	Binary systems	17
1.2.5	Stochastic sources	20
1.3	Detectors and Detection	21
1.3.1	Principle of operation of interferometric detectors	21
1.3.2	The response of a ground-based interferometer	23
1.3.3	Noise budget of the detector	26
1.3.4	Global network of detectors	27
1.3.5	Detection	29
1.4	Overview of LIGO/Virgo events	30
1.4.1	Science summary of observations	30
1.5	Future Prospects: Future Detectors	33
2	Bayesian Inference: Inferring Physics and Astrophysics from Gravitational Wave Observations	37
2.1	Bayesian Inference	37
2.1.1	Detector Data	37
2.1.2	Waveform models for binary black hole coales- cences	38
2.1.3	Parameter Estimation	41
2.1.4	Hypothesis testing	42
2.1.5	Algorithms	43
2.2	Testing General Relativity	44
2.2.1	Classical Tests of General Relativity	44
2.2.2	Binary pulsar tests of General Relativity	47

2.2.3	Strong field tests of General Relativity	47
2.2.4	Null tests of General Relativity in the strong field regime	48
3	The Inspiral-Merger-Ringdown Consistency Test	51
3.1	Method	52
3.1.1	Choice of priors	54
3.2	Simulations of GR signals in Gaussian noise	55
3.3	Simulations of modified GR signals in Gaussian noise	58
3.3.1	Generation of modified GR waveforms	58
3.3.2	Results from the simulations of modified GR signals	63
3.3.3	Caveats	65
3.4	Robustness of the consistency test	66
3.4.1	Cutoff frequency between the inspiral and merger- ringdown	68
3.4.2	Waveform approximant	69
3.4.3	Fit formulae for the mass and spin of the final black hole	70
3.4.4	Effects of spin precession and higher modes . .	71
3.4.5	Effect of splitting the signal in the frequency domain	72
3.5	Future work	74
3.5.1	Implementation of the consistency test in the time-domain	77
4	Gravitational Wave Observations by the Advanced Detec- tors and the Inspiral Merger Ringdown Consistency Test	81
4.1	GW ₁₅₀₉₁₄	83
4.2	GW ₁₇₀₁₀₄	88
4.3	GW ₁₇₀₈₁₄	90
5	Acknowledgements	93
6	Publications	95
A	Appendix	97
A.1	Calculation of the posterior of the parameters describ- ing deviations from GR	97

A.2	Calculation of joint posterior obtained from multiple observations	97
A.3	Definition of the Likelihood Function	100
B	Bibliography	107

1 | Introduction: Gravitational Waves

1.1 Gravitational Waves

In 1905, Albert Einstein published his theory of special relativity (SR) which postulated that the laws of physics are invariant in all inertial frames, and that information cannot travel at a speed faster than the speed of light in vacuum. In 1908, he took a step forward in generalising the principles of SR to all frames of reference (inertial and non-inertial), when he introduced the principle of equivalence which states: "At every spacetime point in an arbitrary gravitational field it is possible to choose a locally inertial coordinate system, such that, within a sufficiently small region of the point in question, the laws of nature take the same form as in unaccelerated Cartesian coordinate systems in the absence of gravitation" ¹. Finally in November 1915, Einstein published the full theory, called the theory of general relativity (GR), which predicts that gravity arises as a consequence of the interaction between the geometry of spacetime and its matter-energy content. This dynamical relationship is expressed through the Einstein's field equations ²:

$$G_{\alpha\beta} = 8\pi T_{\alpha\beta} \quad (1.1)$$

where the left-hand-side represents the geometry or the curvature of spacetime through the Einstein tensor, $G_{\alpha\beta} := R_{\alpha\beta} - \frac{1}{2}g_{\alpha\beta}R$ ($R_{\alpha\beta}$, R and $g_{\alpha\beta}$ are the Ricci tensor, the Ricci scalar and the metric tensor respectively) and the right-hand-side through the stress-energy tensor $T_{\alpha\beta}$, represents the matter-energy content of the universe. The indices α, β run over all four spacetime indices taking values 0, 1, 2, 3. This dynamical relationship is perhaps best expressed through John Wheeler's famous quote: "Spacetime tells matter how to move; matter tells spacetime how to curve".

¹ S Weinberg. Gravitation and cosmology. ed. John Wiley and Sons, New York, 1972

² Throughout this thesis, we would be working in natural units: $G = c = 1$, unless we explicitly specify. Here G is Newton's gravitational constant, and c is the speed of light in vacuum. In these units $1M_{\odot} \simeq 5 \times 10^{-6}s \simeq 1.5km$

One of the most remarkable predictions of GR is the existence of *gravitational waves* ³. For a weak gravitational field, spacetime is assumed to be 'nearly' flat and the metric $g_{\alpha\beta}$, a correction over the metric for flat Minkowskian spacetime $\eta_{\alpha\beta}$:

$$g_{\alpha\beta} = \eta_{\alpha\beta} + h_{\alpha\beta} \quad (1.2)$$

where,

$$|h_{\alpha\beta}| \ll 1 \quad (1.3)$$

This assumption leads one to the weak-field Einstein equations ⁴:

$$\square \bar{h}_{\alpha\beta} = -16\pi T_{\alpha\beta} \quad (1.4)$$

where $\bar{h}^{\alpha\beta}$ is the *trace-reversed form* of $h_{\alpha\beta}$, defined as:

$$\bar{h}^{\alpha\beta} := h_{\alpha\beta} - \frac{1}{2}\eta_{\alpha\beta}h \quad (1.5)$$

where h is the trace of the tensor $h_{\alpha\beta}$, $h := h^\alpha_\alpha$. In vacuum, where $T_{\alpha\beta} = 0$, the weak-field equations become:

$$\left(-\frac{\partial^2}{\partial t^2} + \nabla^2 \right) \bar{h}_{\alpha\beta} = 0 \quad (1.6)$$

This is the wave equation in three-dimensions, with a plane-wave solution:

$$\bar{h}_{\alpha\beta} = A_{\alpha\beta} \exp(ik_\alpha x^\alpha) \quad (1.7)$$

where k_α represents the direction of travel of the gravitational wave, and $A_{\alpha\beta}$ is a tensor which, while working in a specific gauge called the *transverse-traceless* (TT) gauge, can be shown to have only two independent physically important components A_{xx}^{TT} and A_{xy}^{TT} (for a wave propagating in z-direction) ⁵:

$$(A_{\alpha\beta}^{TT}) = \begin{bmatrix} 0 & 0 & 0 & 0 \\ 0 & A_{xx}^{TT} & A_{xy}^{TT} & 0 \\ 0 & A_{xy}^{TT} & -A_{xx}^{TT} & 0 \\ 0 & 0 & 0 & 0 \end{bmatrix} \quad (1.8)$$

It follows that a gravitational wave travelling in the z-direction has two independent components, h_{xx}^{TT} and h_{xy}^{TT} . In a Lorentz frame where two particles are initially at rest and separated in the x-direction by a distance ϵ just before a gravitational wave passes, choosing the

³ Albert Einstein. Approximative integration of the field equations of gravitation. *Sitzungsber. Preuss. Akad. Wiss. Berlin (Math. Phys.)*, 1916:688–696, 1916; and Albert Einstein. Über gravitationswellen. *Sitzungsberichte der Königlich Preussischen Akademie der Wissenschaften (Berlin)*, Seite 154-167., 1918

⁴ Bernard Schutz. *A first course in general relativity*. Cambridge university press, 2009

⁵ In the TT gauge, $A^{\alpha\beta}$ can be shown to be traceless (i.e. $A^\alpha_\alpha = 0$) as well as transverse to the direction of propagation of gravitational waves (i.e. $A_{\alpha 0} = A_{\alpha z} = 0$ for all α).

TT gauge leads to a coordinate system attached to the particles, and in such a frame the coordinate distance between the two particles does not change by the passage of gravitational waves. However the proper distance between the two particles:

$$\Delta l \approx [1 + \frac{1}{2}h_{xx}^{TT}(x=0)]\epsilon \quad (1.9)$$

does change by the passage of gravitational waves and is measurable. This is sometimes referred to as the 'stretching' of space. It follows from Eq. 1.9 that such a change between two freely falling particles is directly proportional to the initial separation ϵ , i.e, the larger the initial separation, the easier it is to detect the change. Eq. 1.9 also shows that Δl is proportional to h_{ij}^{TT} which is typically of the order of 10^{-21} or smaller for expected astrophysical sources, which is why detecting such signals has been such a challenge until the first decade of the 21st century.

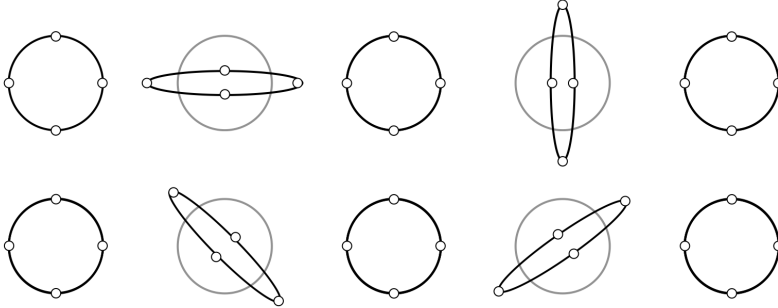


Figure 1.1: The two independent polarisations of a gravitational wave passing perpendicular to a ring of freely falling particles lying in the x - y plane. The *top panel* shows the case where $h_{xx}^{TT} \neq 0; h_{xy}^{TT} = 0$, i.e, '+' (plus) polarisation, while the *bottom panel* is when $h_{xy}^{TT} \neq 0; h_{xx}^{TT} = h_{yy}^{TT} = 0$, i.e., 'x' (cross) polarisation.

The effect of the passage of a gravitational wave can also be viewed as *tidal forces* on particles. Consider two particles separated by a vector $\vec{\xi}$, initially at rest before the passage of the gravitational wave in a local inertial frame. Then it can be shown that the passage of the wave is equivalent to the acceleration of one of the particles as measured in the local inertial frame whose motion initially coincided with the motion of the second particle. Thus the action of the gravitational wave on the first particle will appear to the second particle, like a force pushing it. This is called the *tidal force* associated with gravitational waves.

We can further show that if the initial separation $\vec{\xi} \rightarrow (0, \epsilon, 0, 0)$ is

in the x-direction, then:

$$\frac{\partial^2}{\partial t^2} \xi^x = \frac{1}{2} \epsilon \frac{\partial^2}{\partial t^2} h_{xx}^{TT} \quad (1.10)$$

$$\frac{\partial^2}{\partial t^2} \xi^y = \frac{1}{2} \epsilon \frac{\partial^2}{\partial t^2} h_{xy}^{TT} \quad (1.11)$$

and if the initial separation is in the y-direction, then:

$$\frac{\partial^2}{\partial t^2} \xi^y = \frac{1}{2} \epsilon \frac{\partial^2}{\partial t^2} h_{yy}^{TT} = -\frac{1}{2} \epsilon \frac{\partial^2}{\partial t^2} h_{xx}^{TT} \quad (1.12)$$

$$\frac{\partial^2}{\partial t^2} \xi^x = \frac{1}{2} \epsilon \frac{\partial^2}{\partial t^2} h_{xy}^{TT} \quad (1.13)$$

since $h_{xx}^{TT} = -h_{yy}^{TT}$. Now, consider a gravitational wave passing perpendicular to a ring of freely falling particles lying in the x-y plane. If $h_{xx}^{TT} \neq 0; h_{xy}^{TT} = 0$ then the proper distance of the ring from the centre of the ring changes as shown in the top panel of Fig. 1.1, and if $h_{xy}^{TT} \neq 0; h_{xx}^{TT} = h_{yy}^{TT} = 0$, the the ring moves as shown in the bottom panel of Fig. 1.1. These two independent states define the two independent *polarisations* of a gravitational wave. They are respectively called the '+' (plus) and 'x' (cross) polarisations, and are rotated 45° with respect to each other. We will return to the definition of these polarisation in Sec.1.3, when we discuss the detection of gravitational waves.

1.2 Sources

The typical magnitudes for the amplitudes of gravitational waves that can be expected on Earth from the most luminous sources in the universe, is what has primarily driven the effort of detection. The knowledge of these typical magnitudes come from our understanding of the sources of gravitational waves themselves. The Einstein's equations (Eq.1.1) are a set of second-order non-linear partial differential equations, and it is quite difficult to find exact analytical solutions for most sources of gravitational waves. In some cases, numerical methods can be employed, but are usually computationally expensive. An alternate approach for a gravitationally bound system, is to adopt an iterative analytical approximation scheme called the post-Newtonian approximation ⁶. In systems where the typical velocities inside a source are small compared to the speed of light, one can do a low-velocity expansion of the right-hand-side of Eq. 1.4

⁶ Luc Blanchet. Gravitational radiation from post-newtonian sources and inspiralling compact binaries. *Living Reviews in Relativity*, 17(1):2, 2014; Luc Blanchet, Thibault Damour, and Bala R Iyer. Gravitational waves from inspiralling compact binaries: Energy loss and waveform to second-post-newtonian order. *Physical Review D*, 51(10):5360, 1995; Eric Poisson. Gravitational waves from inspiraling compact binaries: The quadrupole-moment term. *Physical Review D*, 57(8):5287, 1998; Luc Blanchet, Thibault Damour, and Gilles Esposito-Farese. Dimensional regularization of the third post-newtonian dynamics of point particles in harmonic coordinates. *Physical Review D*, 69(12):124007, 2004; Thibault Damour and Alessandro Nagar. Improved analytical description of inspiralling and coalescing black-hole binaries. *Physical Review D*, 79(8):081503, 2009; KG Arun, Alessandra Buonanno, Guillaume Faye, and Evan Ochsner. Higher-order spin effects in the amplitude and phase of gravitational waveforms emitted by inspiraling compact binaries: Ready-to-use gravitational waveforms. *Physical Review D*, 79(10):104023, 2009; Alessandra Buonanno, Guillaume Faye, and Tanja Hinderer. Spin effects on gravitational waves from inspiraling compact binaries at second post-newtonian order. *Physical Review D*, 87(4):044009, 2013; and Alejandro Bohé, Guillaume Faye, Sylvain Marsat, and Edward K Porter. Quadratic-in-spin effects in the orbital dynamics and gravitational-wave energy flux of compact binaries at the 3pn order. *Classical and Quantum Gravity*, 32(19):195010, 2015

and show that gravitational waves are produced (to leading order) by a time-varying quadrupole moment of a source, Q_{ij} ⁷:

$$h_{ij}^{TT}(t, \mathbf{x}) = \frac{2}{r} \ddot{Q}_{ij}^{TT}(t - r) \quad (1.14)$$

where quantities are computed in the TT gauge, at a position \mathbf{x} , a distance r away from the source, the spatial gravitational wave tensor h_{ij}^{TT} at a time t is due to the state of the source at the retarded time $t - r$ and a dot indicates a time derivative. The quadrupole moment Q_{ij} , at the lowest post-Newtonian order, is the second moment of the mass distribution and depends only on the density ρ of the system, as:

$$Q_{ij} = \int \rho x_i x_j d^3x \quad (1.15)$$

1.2.1 Simple order-of-magnitude estimates

Amplitude⁸: Gravitational waves are produced (to leading order) by the time-varying quadrupole moment of the source. A spherically symmetric system does not produce gravitational waves. Hence the typical magnitudes of the gravitational wave amplitude can be related to the non-spherical component of the system, as:

$$h \sim \frac{2}{r} \ddot{Q}_{ij} \sim \frac{2}{r} (Mv^2)_{\text{nonsph}} \quad (1.16)$$

where $(Mv^2)_{\text{nonsph}}$ is twice the kinetic energy of the non-spherical component of the source. In an extreme limit, the non-spherical motions is due to the entire mass of the system. Then $(Mv^2)_{\text{nonsph}} = M(v^2)_{\text{nonsph}}$. We also know that the Newtonian potential $\phi_{\text{ext}} = M/r$. Thus we are able to put a bound on the ratio:

$$h/\phi_{\text{ext}} < 2v_{\text{nonsph}}^2 \leq 2\phi_{\text{int}} \quad (1.17)$$

where the last inequality is from the Virial theorem for self-gravitating bodies. Thus, we obtain the following bound on the amplitude of gravitational waves:

$$h \leq 2\phi_{\text{int}}\phi_{\text{ext}} \quad (1.18)$$

For a neutron star source ($\phi_{\text{int}} \sim 0.2$), in the Virgo cluster ($r \sim 18$ Mpc) and mass $\sim 1.4M_{\odot}$, the upper limit on $h \sim 10^{-21}$. These are typically the amplitudes of gravitational waves that the current

⁷Michele Maggiore. *Gravitational Waves: Volume 1: Theory and Experiments*, volume 1. Oxford university press, 2008

⁸This section presents a few order of magnitude calculations of the gravitational wave amplitude, frequency and luminosity. The treatment is heavily borrowed from [109]

generation of ground-based interferometric detectors are hunting for.

Frequency: The Newtonian formula for the natural frequency f_0 , of a self-gravitating body with a mean density $\bar{\rho}$, is:

$$f_0 = \sqrt{\bar{\rho}/4\pi} \quad (1.19)$$

This can be rewritten for a compact object with mass M and radius R , like a neutron star or a black hole:

$$f_0 \simeq 1\text{kHz} \left(\frac{10M_\odot}{M} \right) \quad (1.20)$$

Thus for neutron star systems, this natural frequency is usually of the order of a few kHz, while for stellar-mass black holes, they are from a few tens to a few hundred Hz. For super-massive black holes, the natural frequency is in the range of a few mHz. As we shall see in Sec.1.3.3, the ground-based interferometric detectors like Advanced LIGO and Virgo are most sensitive in the frequency band between about 10Hz to 1kHz, which make binaries of systems composed of neutron stars and/or black holes promising candidates for detection.

Luminosity: A gravitational wave carries energy and angular momentum away from a source. In the quadrupolar approximation, the luminosity L of a gravitational wave source is expressed through the Einstein quadrupole formula ⁹:

$$L = \frac{1}{5} \langle \ddot{Q}_{ij} \ddot{Q}^{ij} \rangle \quad (1.21)$$

The above expression is written in natural units, but in SI units, it must be multiplied by a factor $L_0 = c^5/G = 3.6 \times 10^{52}$ W. Even if the gravitational wave source emits radiation with a fraction of this luminosity, it will still be huge. The solar luminosity is 3.8×10^{26} W, a typical galaxy has luminosity close to 10^{37} W. All the stars in all the galaxies in the visible universe put together have a luminosity $\sim 10^{48}$ W. As comparison, the peak luminosity of the first detection, GW150914 was $\sim 3.6 \times 10^{49}$ W, more than ten times greater than the combined luminosity of every star and galaxy in the observable Universe. From Eq.1.14 and Eq.1.21 one finds that the apparent luminos-

⁹ Bernard Schutz. *A first course in general relativity*. Cambridge university press, 2009; Michele Maggiore. *Gravitational Waves: Volume 1: Theory and Experiments*, volume 1. Oxford university press, 2008; and B.S. Sathyaprakash and B.F. Schutz. *Physics, Astrophysics and Cosmology with Gravitational Waves*. *Living Rev. Relat.*, 12:2, 2009

ity far from the source is related to the gravitational wave amplitude as¹⁰:

$$\mathcal{F} \sim \frac{|\dot{h}|^2}{16\pi} \quad (1.22)$$

This can be used to write the gravitational wave amplitude h in terms of the rate of energy loss by the source, predominantly at some frequency f , as:

$$h \sim \frac{1}{\pi f r} \sqrt{\frac{E}{T}} \quad (1.23)$$

where the source at distance r emits energy E in time T . Since the energy can be assumed to be emitted at frequency f , we can write $\dot{h} = 2\pi f h$, and the apparent flux \mathcal{F} can be approximately written as $E/(4\pi r^2 T)$.

In summary, ground-based interferometric detectors are most likely to observe gravitational waves sources with amplitudes of 10^{-21} or smaller, emitted at frequencies between 10Hz - 1kHz at a fraction of the luminosity L_0 . Unfortunately this rules out man-made sources of gravitational waves, where even the most optimistic amplitudes are $\sim 10^{-43}$. Thus most of the sources of gravitational waves that are of relevance to such detectors are of astrophysical nature¹¹, and can be broadly classified in four categories, described below.

¹⁰ Bernard Schutz. *A first course in general relativity*. Cambridge university press, 2009

¹¹ Curt Cutler and Kip S Thorne. An overview of gravitational-wave sources. In *General Relativity and Gravitation*, pages 72–111. World Scientific, 2002; and B.S. Sathyaprakash and B.F. Schutz. Physics, Astrophysics and Cosmology with Gravitational Waves. *Living Rev. Relat.*, 12:2, 2009

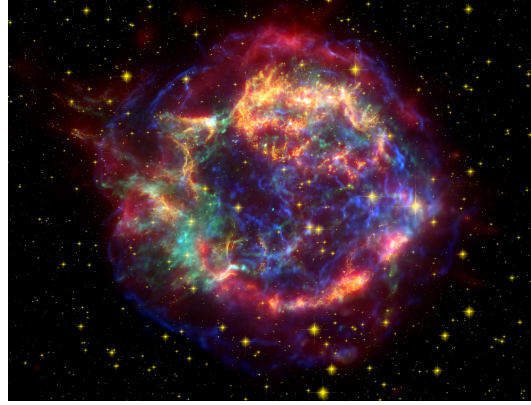
1.2.2 Burst sources

The end stages of stellar evolution involve the formation of neutron stars or black holes when a massive star exhausts all its fuel and collapses under the force of gravity. If such gravitational collapses are spherically asymmetric, then the source has a time-varying quadrupole moment and gravitational waves are produced. Alternatively the core-collapse of accreting compact objects could also produce gravitational waves. Such sources are called *burst sources*. Gravitational waves from a burst source are usually unmodelled because a lot of the physics behind the mechanism of a gravitational collapse is unknown. If we know the rate of emission of energy from such a source, a rough estimate of the amplitude of gravitational waves

emitted can be done using Eq.1.23:

$$h \sim 6 \times 10^{-21} \left(\frac{E}{10^{-7} M_{\odot}} \right)^{1/2} \left(\frac{1 \text{ms}}{T} \right)^{1/2} \left(\frac{1 \text{kHz}}{f} \right) \left(\frac{10 \text{kpc}}{r} \right) \quad (1.24)$$

where we have scaled the right-hand-side with respect to a burst source at a distance of 10 kpc, emitting $10^{-7} M_{\odot}$ equivalent of energy in 1 ms, at a frequency of 1 kHz. Attempts to observe such signals involve looking for excess power over the background during an extremely short period of time, because most of such sources are expected to be transient sources with a low event rate inside a supercluster like Virgo ¹².



¹² Matt Taylor, David Cinabro, Ben Dilday, Lluís Galbany, Ravi R Gupta, R Kessler, John Marriner, Robert C Nichol, Michael Richmond, Donald P Schneider, et al. The core collapse supernova rate from the sdss-ii supernova survey. *The Astrophysical Journal*, 792(2): 135, 2014

Figure 1.2: Chandra X-ray photograph of Cassiopeia A, the youngest supernova remnant in the Milky Way. Credit: NASA/CXC/MIT/UMass Amherst/M.D.Stage et al.

1.2.3 Spinning neutron stars

Another source of a time-varying quadrupole moment might be a "bump" or an asymmetry on the surface of a spinning neutron star. A neutron star of mass M , and radius R , spinning at a frequency f and with a bump of mass m on its surface is expected to spin down due to emission of gravitational waves. The bump is usually characterised through a fractional asymmetry defined as the ratio of the moment of inertia of the bump to the spherical moment of inertia of the entire neutron star: $\epsilon = mR^2 / (\frac{2}{5}MR^2) = \frac{5m}{2M}$. The "bump" can be treated as the non-spherical component of the neutron star, rotating at a frequency f about the axis. Hence it emits gravitational waves with a frequency $2f$, and Eq.1.17 gives us an estimate of the amplitude of radiation at a distance r :

$$h \sim (4/5)v_{\text{non sph}}^2 \epsilon M/r = (4/5)(2\pi Rf)^2 \epsilon M/r \quad (1.25)$$

and the luminosity (from Eq.1.21), as:

$$L \sim (16/125)(2\pi f)^6 \epsilon^2 M^2 R^4 \quad (1.26)$$

where, to make an order of magnitude estimate, we have assumed that the four independent components of Q_{ij} in Eq.1.21 all have comparable magnitudes. Since the energy emitted into gravitational waves is mostly extracted from the rotational kinetic energy of the star $\frac{1}{5}Mv^2$, the typical timescale for the spindown of the neutron star is:

$$t_{\text{spindown}} \sim \frac{1}{5}Mv^2/L \sim \frac{25}{32\pi} \epsilon^{-2} f^{-1} \left(\frac{M}{R}\right)^{-1} v^{-3} \quad (1.27)$$

where v is the rotational velocity of the neutron star. The typical spindown rates of neutron stars allow us to put upper bounds on the fractional asymmetries ϵ . For the Crab pulsar ¹³, latest results from Advanced LIGO place upper bounds on ϵ at $\sim 10^{-5}$, which, given the distance to the Crab pulsar is 2 kPc, should produce an amplitude for gravitational waves on Earth $\sim 10^{-25}$. Although this is much smaller than the typical amplitudes of $\sim 10^{21}$ that are expected for the burst or the transient sources, gravitational waves from spinning neutron stars can still be expected to be observed, because unlike transient sources which last for a fraction of a second, such sources produce gravitational waves for a long period of time, and consequently can have a long observation period. Such sources are thus called *continuous wave* sources.

¹³ Benjamin P Abbott, R Abbott, TD Abbott, MR Abernathy, F Acernese, K Ackley, C Adams, T Adams, P Addesso, RX Adhikari, et al. First search for gravitational waves from known pulsars with advanced ligo. *The Astrophysical Journal*, 839(1):12, 2017

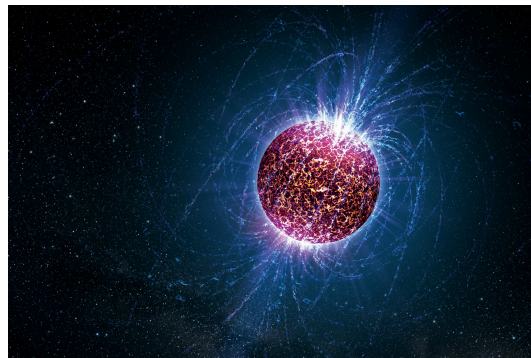


Figure 1.3: Artist's depiction of a super dense and compact neutron star (Casey Reed/Penn State University)

1.2.4 Binary systems

A binary system composed of two compact objects like white dwarves, neutron stars and/or black holes move around each other in circu-

lar/elliptical orbits. For initial rough estimates of the amplitude and luminosity of such sources, let us assume two objects of mass m in a circular orbit of radius R . Since their entire motion contributes to the non-spherical component of motion of the source¹⁴:

$$(Mv^2)_{\text{nonsph}} = Mv_{\text{nonsph}}^2 = M(\Omega R)^2 = \frac{M^2}{R} \quad (1.28)$$

where Ω is the orbital angular velocity and M is the total mass of the system. Following the simple-estimates prescription given above, we can obtain expressions for the gravitational wave amplitude and luminosity as:

$$h \sim 2 \frac{M}{r} \frac{M}{R} = \frac{2}{r} M^{5/3} \Omega^{2/3} \quad (1.29)$$

$$L \sim \frac{4}{5} \left(\frac{M}{R} \right)^{4/5} \quad (1.30)$$

where in the first equation we substitute for R in terms of the orbital angular velocity Ω to obtain the term on the right-hand-side. The second equation shows that if the gravitational wave source is highly relativistic and compact, then $M/R \sim 1$, and it radiates a significant amount of radiation as gravitational waves. Because of emission of radiation into gravitational waves, conservation of energy causes the orbit to shrink. Consequently, due to conservation of angular momentum, the objects start to move faster, i.e., the orbital angular frequency Ω increases, causing it to emit more radiation into gravitational waves. Hence, the backreaction due to gravitational waves leads to a run-away process in which the two objects spiral in with an increase in the frequency and the amplitude of gravitational waves emitted, with time. This is called the gravitational wave *chirp*, and has an associated timescale:

$$t_{\text{chirp}} = \frac{Mv^2}{2} / L \sim \frac{5M}{8} \frac{M^{-4}}{R} \quad (1.31)$$

For astrophysical binary systems with unequal masses, the above equations can be refined and rewritten in terms of a quantity called the *chirp mass* of the binary, defined as $\mathcal{M}_c := \frac{(m_1 m_2)^{3/5}}{(m_1 + m_2)^{1/5}}$ ¹⁵:

$$h \sim \frac{1}{r} \mathcal{M}_c^{5/3} \Omega^{2/3} \quad (1.32)$$

¹⁴ B.S. Sathyaprakash and B.F. Schutz. Physics, Astrophysics and Cosmology with Gravitational Waves. *Living Rev. Relat.*, 12:2, 2009

¹⁵ Benjamin P Abbott, R Abbott, TD Abbott, MR Abernathy, F Acernese, K Ackley, C Adams, T Adams, P Addesso, RX Adhikari, et al. Properties of the binary black hole merger gw150914. *Physical review letters*, 116(24):241102, 2016

The shrinking of the orbit, measured in terms of the rate of decay of the orbital period P_b , is:

$$\dot{P}_b = -\frac{192\pi}{5} \left(\frac{2\pi\mathcal{M}_c}{P_b} \right)^{5/3} \quad (1.33)$$

leading to a chirp time:

$$t_{\text{chirp}} = \frac{5M}{96\mu} \left(\frac{M}{R} \right)^{-4} \quad (1.34)$$

where $\mu := (m_1 m_2)/M^2$ is called the symmetric mass ratio of the system. As mentioned above, during the gravitational wave chirp, the orbit shrinks with a monotonic increase in the amplitude and frequency of the radiation emitted into gravitational waves. The inspiral proceeds till the two object come close enough to interact with each other and start to merge. A convenient scale to denote the end of the inspiral is when the distance between the compact objects is equal to the last stable orbit (LSO) $R = 6M$, which has a frequency:

$$f_{\text{LSO}} \sim 220 \left(\frac{20M_\odot}{M} \right) \text{Hz} \quad (1.35)$$

which is called the LSO frequency. A binary white dwarf system is expected to merge a lot before it can reach the LSO, because although white dwarves have masses similar to a neutron star, they are a lot less compact, with radii which are a few thousand kilometres. Gravitational waves from the inspiral of white dwarf binaries are expected to be in the mHz to a few Hz range, making them suitable candidates for space-based detectors rather than the current ground-based ones.

Binaries composed of more compact objects like neutron stars and/or black holes are able to reach the LSO without merging. Such coalescences occur at frequencies beyond the frequency at the LSO. Hence they are among the most luminous sources of gravitational waves in the universe. Such binaries of neutron stars and stellar-mass black holes are expected to have a frequency range from a few Hz to a few kHz, which fall in the sensitivity band of ground-based interferometric detectors. Also at design sensitivity the advanced LIGO and Virgo detectors will be searching for such binaries upto distances as far as 15 Gpc (for high stellar-mass black hole binaries), and are expected to observe systems at a rate of a few tens to a few hundreds per Gpc³ per year.¹⁶

¹⁶ Benjamin P Abbott et al. GW170104: Observation of a 50-solar-mass binary black hole coalescence at redshift 0.2. *Physical Review Letters*, 118:221101, 2017

There is another class of binary black hole mergers where the individual black holes have masses between $10^6 - 10^9 M_\odot$. Such black holes are called super-massive black holes and are expected to be present at the centre of most galaxies, including our own. Eq.1.35 shows that the frequency at the LSO scales inversely with the total mass of the system, and hence for the coalescence of two super-massive black holes, f_{LSO} is of the order of a few mHz to tens of mHz. This is supposed to be the frequency of operation of the space-based detectors, like LISA, for which the super-massive black hole binary coalescences are one of the most promising sources¹⁷.

¹⁷ Danzmann et al. 61

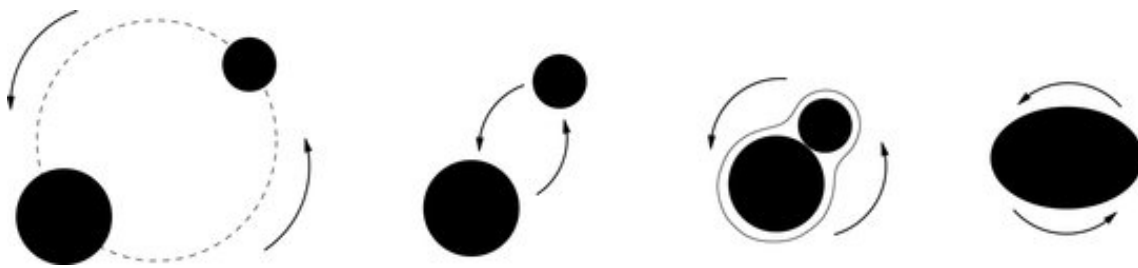


Figure 1.4: Stages of binary black hole coalescence: (from left to right) inspiral, plunge, merger, and ringdown. Courtesy: A. Taracchini/AEI

Quasi-normal modes of a black hole: After the two black holes merge, the remnant object sheds away its asymmetries through a spectrum of gravitational radiation in the form of exponentially damped sinusoids, called the *quasi-normal-modes* (QNMs), before settling down to a stable Kerr black hole. The spectrum of QNMs can be solved for using black hole perturbation theory¹⁸. For the ground-based detectors, the dominant QNM occurs at a frequency near the upper end of its sensitivity band (depending on the mass and spin of the remnant object), and it is possible to observe them for an especially loud signal. However, a space-based detector like LISA is a much better prospect to observe clear QNMs from the merger of super-massive black hole binaries. This phase of evolution of a compact binary coalescence (CBC) is called the *ringdown* (Fig.1.4).

¹⁸ CV Vishveshwara. Scattering of gravitational radiation by a schwarzschild black-hole. *Nature*, 227(5261):936, 1970

1.2.5 Stochastic sources

A stochastic signal arises from the indistinguishable overlap of gravitational waves from multiple sources mentioned above, arriving at the detector from all directions without any phase coherence. It is

also possible that a part of the stochastic signal is from the gravitational waves which originated at various energetic processes at the early universe. They are the quietest signals, but as we will see in Sec.1.4, bounds placed on the amplitude of this stochastic background from gravitational wave observations by Advanced LIGO-Virgo, make their detection a real possibility, in the upcoming years.

1.3 Detectors and Detection

The direct detection of gravitational waves involves measuring the tidal distortions mentioned at the end of Sec.1.1. The first attempts to measure gravitational waves were using resonant bar detectors by Josep Weber in 1960¹⁹. However limitations on the size of the bars and materials used, challenges in reducing thermal noise, and their narrow band nature provided severe constraints on the gravitational waves detectable by these bars. It soon became obvious that the way forward was an interferometric set-up and more time and money was invested into beam detectors from the late 1980s onward. Pulsar timing²⁰ and Cosmic Microwave Background (CMB) polarisation measurements are two other methods used in the search for gravitational waves. While pulsar timing looks for gravitational waves in the frequency range around nHz, CMB temperature perturbations are expected to be affected by gravitational waves in the frequency range $\sim 10^{-16}$ Hz. However, for the rest of this section we will focus on interferometric detectors.

¹⁹ Joseph Weber. Detection and generation of gravitational waves. *Physical Review*, 117(1):306, 1960

²⁰ G Hobbs, A Archibald, Z Arzoumanian, D Backer, M Bailes, NDR Bhat, M Burgay, S Burke-Spolaor, D Champion, I Cognard, et al. The international pulsar timing array project: using pulsars as a gravitational wave detector. *Classical and Quantum Gravity*, 27(8):084013, 2010

1.3.1 Principle of operation of interferometric detectors

The basic principle of operation of beam detectors, including interferometers, involve time-of-flight measurements using light. Since the speed of light c is a constant in vacuum, one can measure proper distances by having light (or electromagnetic radiation) reflect off the distant object, and measure the total time of flight Δt . The distance to the object is then just $c\Delta t/2$. We now consider the simple experiment where we have laser light being bounced off two freely falling objects and a gravitational wave passes through this system, such that the angle between the direction of propagation of light and the plane gravitational wave is θ . Since the two objects are freely falling, we can use the TT coordinate system, and let us assume that in this

coordinate system the wave just has a '+' polarisation $h_+(t)$. We need two clocks in this experiment: the first one records the departure times of each photon t and the second clock records their return times t_f . If the proper distance between the freely falling objects in the absence of a gravitational wave is L , then the effect of the gravitational wave would be to change the proper distance between the two objects, and hence rate at which the photons return as a function of the rate at which they leave the source. In linearised theory, this is given by:

$$\frac{dt_f}{dt} = 1 + \frac{1}{2}(1 + \cos\theta)[h_+(t + (1 - \cos\theta)L) - h_+(t)] \quad (1.36)$$

Since $h_+(t)$ is the amplitude of the gravitational wave when it leaves the emitter, $h_+(t + (1 - \cos\theta)L)$ would be the amplitude of the wave when the photon reaches the receiver. Thus, the time-of-flight is only dependent on the amplitudes of the gravitational wave at the emitter and receiver. Measurements in this arrangement, of-course depends on the stability of the clocks. The most stable atomic clocks can measure time to within an accuracy of 1 part in 10^{16} seconds²¹, which would not be sufficient to measure gravitational waves with amplitudes smaller than $h \sim 10^{-15}$. This problem is overcome by using an interferometric set up. A Michelson interferometer is a set up where a beam of light is split into two (at a beam-splitter S) and sent down two perpendicular arms. At the end of each arm, the beam reflects back off mirrors (M_1 and M_2), and made to recombine at the splitter. The two beams have a fixed phase difference when they leave the beam-splitter, and hence on recombination, they form an interference pattern, which can be observed at the detector. If the two beams were $\pi/2$ out of phase at the beam-splitter, then when they recombine they undergo destructive interference, and produce a dark spot at the detector. Hence in the case of the Michelson interferometer, one of the arms behaves like a clock, and variations in the length of the other arm are measured with respect to it. This makes interferometers one of the most natural instruments to observe gravitational waves.

If we have an interferometer lying in the x-y plane with its two perpendicular arms along the positive x- and y-axes respectively, and

²¹ John W Armstrong. Low-frequency gravitational wave searches using spacecraft doppler tracking. *Living Reviews in Relativity*, 9(1):1, 2006

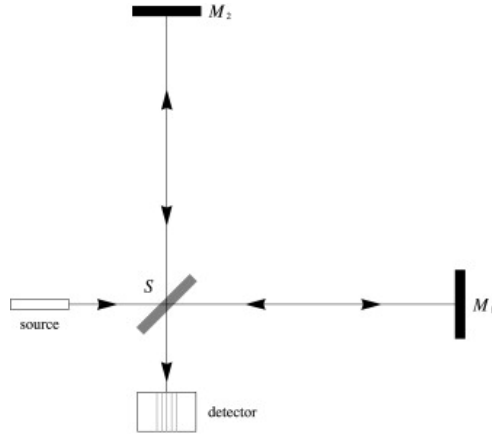


Figure 1.5: A basic Michelson interferometer set up. Picture courtesy [92]

the corner station at the origin, and the gravitational waves with just a '+' polarisation $h_+(t)$ travelling in the z -direction, as shown in the top panel of Fig. 1.1, during one cycle of the gravitational wave, the x -arm will get shortened while the y -arm will be stretched, and get reversed during the next cycle. These differential changes in the arm-lengths will be measured using the time-of-flight method explained above. However, a gravitational wave with just a 'x' polarisation $h_\times(t)$ travelling in the z -direction, will affect the two arms identically, and hence the interferometer will not see the wave.

1.3.2 The response of a ground-based interferometer

Interferometers measure the differential changes between the arm-lengths caused by the passage of a gravitational wave. We have seen in Eq. 1.9 that such changes are exaggerated farther away the end-mirrors are. Thus, modern ground-based interferometric detectors are made several kilometres long (for eg, the advanced LIGO detectors²² are 4 km long, the advanced Virgo detector²³ is 3 km long) and the space-based detectors (for eg, LISA²⁴) are meant to be millions of kilometres apart. These lengths are still much smaller than the wavelength of a gravitational waves, and hence for $L \ll \lambda_{GW}$, one can rewrite Eq. 1.36 as:

$$\frac{dt_f}{dt} = 1 + \sin^2\theta L \dot{h}_+(t) \quad (1.37)$$

At this point, let us move to a more general tensorial representation and introduce basis vectors to define the radiation and detector frames respectively, and the transformation between them. Consider

²² Junaid Aasi, BP Abbott, Richard Abbott, Thomas Abbott, MR Abernathy, Kendall Ackley, Carl Adams, Thomas Adams, Paolo Addesso, RX Adhikari, et al. Advanced ligo. *Classical and quantum gravity*, 32(7):074001, 2015

²³ F Acernese, M Agathos, K Agatsuma, D Aisa, N Allemandou, A Allocca, J Amarni, P Astone, G Balestri, G Ballardini, et al. Advanced virgo: a second-generation interferometric gravitational wave detector. *Classical and Quantum Gravity*, 32(2):024001, 2014

²⁴ Karsten Danzmann, LISA Study Team, et al. Lisa: Laser interferometer space antenna for gravitational wave measurements. *Classical and Quantum Gravity*, 13(11A):A247, 1996

\hat{e}_x and \hat{e}_y to be the unit vectors along the x- and y-arms of the detector. If \hat{N} be the unit vector in the direction of propagation of the wave, then let us define the basis vectors in the radiation frame as \hat{e}_x^R and \hat{e}_y^R , where \hat{e}_x^R lies in the plane formed by \hat{N} and \hat{e}_x , and \hat{e}_y^R is orthogonal to \hat{e}_x^R and \hat{N} [c.f Fig.1.6]. In this generalised picture, the

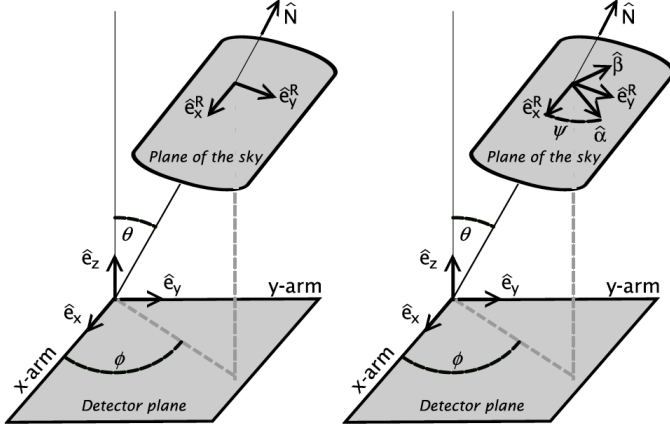


Figure 1.6: The relative orientation of the sky and detector frames (left panel) and the effect of a rotation by the angle ψ in the sky frame (right panel). (Figure and caption courtesy figure 3 in [109])

full waveform has the tensor representation:

$$\mathbf{h}(t) = h_+(t)\mathbf{e}_+ + h_\times(t)\mathbf{e}_\times \quad (1.38)$$

where $\{\mathbf{e}_+, \mathbf{e}_\times\}$ are the polarisation tensors associated with the basis vectors \hat{e}_x^R and \hat{e}_y^R , defined as:

$$\mathbf{e}_+ = (\hat{e}_x^R \otimes \hat{e}_x^R - \hat{e}_y^R \otimes \hat{e}_y^R) \quad (1.39)$$

$$\mathbf{e}_\times = (\hat{e}_x^R \otimes \hat{e}_y^R + \hat{e}_y^R \otimes \hat{e}_x^R) \quad (1.40)$$

We can then rewrite Eq.1.37 to express the rate of the return times of the photons along the x- and y-arms as:

$$\left(\frac{dt_f}{dt}\right)_{\text{x-arm}} = 1 + L\hat{e}_x \cdot \dot{\mathbf{h}} \cdot \hat{e}_x \quad (1.41)$$

$$\left(\frac{dt_f}{dt}\right)_{\text{y-arm}} = 1 + L\hat{e}_y \cdot \dot{\mathbf{h}} \cdot \hat{e}_y \quad (1.42)$$

where a dot represents a derivative with respect to time. Thus the difference in the times taken for a photon to travel down the two

arms can be expressed as:

$$\left(\frac{d\delta t_f}{dt}\right) = \left(\frac{dt_f}{dt}\right)_{\text{x-arm}} - \left(\frac{dt_f}{dt}\right)_{\text{y-arm}} = L(\hat{e}_x \cdot \dot{\mathbf{h}} \cdot \hat{e}_x - \hat{e}_y \cdot \dot{\mathbf{h}} \cdot \hat{e}_y) \quad (1.43)$$

If we define the detector tensor $\mathbf{d} = L(\hat{e}_x \otimes \hat{e}_x - \hat{e}_y \otimes \hat{e}_y)$, then the different return time rate can be expressed as an invariant:

$$\left(\frac{d\delta t_f}{dt}\right) = \mathbf{d} : \dot{\mathbf{h}} \quad (1.44)$$

where $\mathbf{d} : \dot{\mathbf{h}}$ denotes the Euclidean scalar product of the tensor \mathbf{d} and $\dot{\mathbf{h}}$. Integrating the above equation gives us the difference in the return times between a photon travelling along the x- and y-arms of the interferometer, and this is exactly equal to the differences in the path-lengths covered by the photon from time-of-flight measurements. Hence, the differential change in the armlengths $\delta L(t)$ is:

$$\delta L(t) = \frac{1}{2} \mathbf{d} : \mathbf{h} \quad (1.45)$$

Finally making our observations independent of the detector frame (because different detectors can have different orientations), and using the more universal astronomical reference frame, we rotate the plane of the sky by an angle ψ , called the polarisation angle, and choose a new set of basis vectors to define the plane of the sky $\hat{\alpha}$ and $\hat{\beta}$. This transformation is explained in the right-hand panel of Fig.1.6. In this new basis, the polarisation tensors are redefined as:

$$\epsilon_+ = (\hat{\alpha} \otimes \hat{\alpha} - \hat{\beta} \otimes \hat{\beta}) \quad (1.46)$$

$$\epsilon_\times = (\hat{\alpha} \otimes \hat{\beta} + \hat{\beta} \otimes \hat{\alpha}) \quad (1.47)$$

with the transformation equations being:

$$\epsilon_+ = \mathbf{e}_+ \cos 2\psi + \mathbf{e}_\times \sin 2\psi \quad (1.48)$$

$$\epsilon_\times = -\mathbf{e}_+ \sin 2\psi + \mathbf{e}_\times \cos 2\psi \quad (1.49)$$

So, finally, we can write:

$$\frac{\delta L(t)}{L} = F_+(\theta, \phi, \psi) h_+ + F_\times(\theta, \phi, \psi) h_\times \quad (1.50)$$

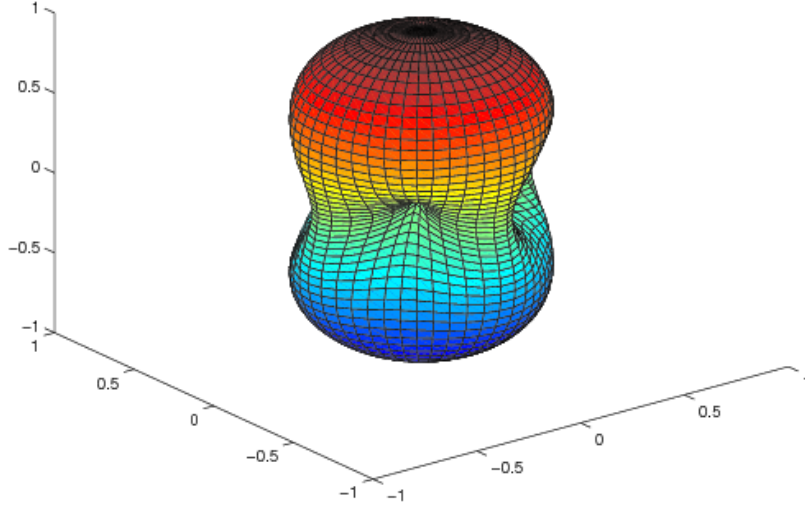


Figure 1.7: The antenna pattern of an interferometric detector (left panel) with the arms in the x-y plane and oriented along the two axes. The response F for waves coming from a certain direction is proportional to the distance to the point on the antenna pattern in that direction. Caption and figure courtesy: Fig.4 in [109]

where $\{F_+(\theta, \phi, \psi), F_\times(\theta, \phi, \psi)\}$ are called the antenna pattern functions of the detector, expressed in terms of the sky position of the source as (in the detector-centred coordinate system):

$$F_+(\theta, \phi, \psi) = \frac{1}{2}(1 + \cos^2\theta)\cos 2\phi\cos 2\psi - \cos\theta\sin 2\phi\sin 2\psi,$$

$$F_\times(\theta, \phi, \psi) = \frac{1}{2}(1 + \cos^2\theta)\cos 2\phi\sin 2\psi + \cos\theta\sin 2\phi\cos 2\psi$$

We carry over these definitions to the next chapter, where we redefine the left-hand-side of Eq.1.50 as the detector strain $h(t) = \frac{\delta L(t)}{L}$.

1.3.3 Noise budget of the detector

Another thing we learn from Eq. 1.9 is that even with kilometre scale interferometers, for realistic source of gravitational waves (discussed in detail in Sec. 1.2), gravitational wave detection demands the measurement of differential displacements $\sim 10^{-18}$ m. There are several noise sources that produce differential displacements in the detector that are of this scale. Hence one would need to isolate the effect of such noise sources before a gravitational waves can be detected. The major contribution to the noise budget of ground-based interferometric detectors comes from seismic noise and thermal noise (due to vibration of the mirrors and the suspending system, as well as the substrate and coating of the mirrors) towards the low-frequency

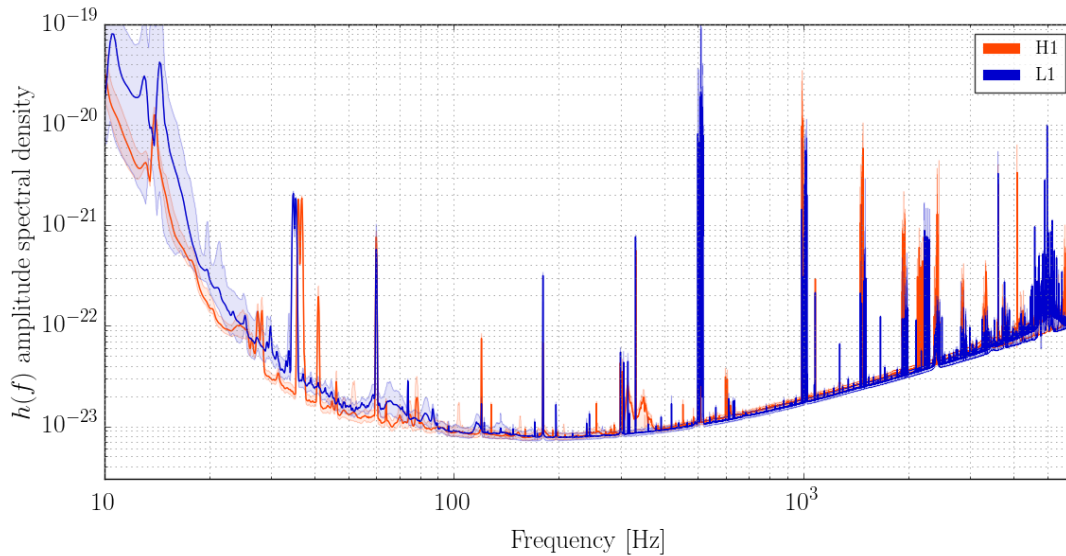


Figure 1.8: The average measured strain-equivalent noise, or sensitivity, of the Advanced LIGO detectors during the time analysed to determine the significance of GW150914 (Sept 12 - Oct 20, 2015). Hanford (H1) is shown in red, Livingston (L1) in blue. The solid traces represent the median sensitivity and the shaded regions indicate the 5th and 95th percentile over the analysis period. The narrowband features in the spectra are due to known mechanical resonances, mains power harmonics, and injected signals used for calibration. [Caption and figure, courtesy: <https://lsc.ligo.org/events/GW150914/>]

end. Hence advanced LIGO at design sensitivity is expected to have a lower frequency cut-off of around 10Hz. At high frequencies, the noise budget is limited due to shot noise arising because of the quantum nature of the photons in the laser beam. Thus, the sensitivity of the detectors span a broadband bucket from around 10Hz to a few kHz, with maximum sensitivity of around 10^{-23} around 200 Hz.

1.3.4 Global network of detectors

The LIGO and Virgo detectors went through two major stages of development. There was an initial version of the LIGO and Virgo detectors, appropriately called *initial LIGO* and *initial Virgo*, which searched for gravitational waves between 2001 and 2010. They were accompanied by a 600 m detector near Hanover, Germany called GEO600²⁵, and a smaller 300 m detector in Japan called TAMA300²⁶ in this search. In 2007, the initial detectors stopped operation and underwent a period of upgrade to their current advanced configurations. The two LIGO detectors went through installation and commissioning between 2010 and 2014, and started taking science quality data from September, 2015. The first observing run lasted till January, 2016, after which there was another break for further upgrades to the detectors. The advanced LIGO detectors conducted their second observing run from December, 2016 to August 23, 2017, running for a period of around 6 months. During the last month of their operation, they were joined by the advanced Virgo detector,

²⁵ Benno Willke, P Ajith, B Allen, P Aufmuth, C Aulbert, S Babak, Ramachandran Balasubramanian, BW Barr, S Berukoff, A Bunkowski, et al. The geo-hf project. *Classical and Quantum Gravity*, 23(8):S207, 2006

²⁶ KIMIO Tsubono. 300-m laser interferometer gravitational wave detector (tama300) in japan. In *First Edoardo Amaldi conference on gravitational wave experiments*, pages 112–114. World Scientific, 1995

that started taking science quality data from August 1, 2017. The detections of GW170814 and GW170817 were made by a three-detector network. After August 23, 2017, both the detectors have been shut down for about a year, during which they will undergo upgrades in their configurations before the start of the third observing run²⁷. In the meantime, a fourth gravitational waves detector called KAGRA²⁸, is under construction in Japan, and expected to start taking science-quality data from 2019. A fifth detector, LIGO India²⁹ will come up in India with the same configuration as the LIGO detectors in the US, in the early 2020s, and become part of a global network of gravitational waves detectors.

A global network is vital for improved sky localisation and parameter estimation. Gravitational wave detectors locate a source in the sky through the method of triangulation. As we have seen in Sec.1.3, the sensitivity of each detectors is dependent on its antenna pattern functions, which means that detectors are more sensitive towards gravitational waves coming from certain directions than others. Analogous to how GPS triangulation works, we need atleast three detectors to localise the position of a gravitational wave source in the sky. Further, since the basic principle for triangulation is measuring the relative time-delays between the arrival times of the signal at the various detectors, farther apart the detectors are, better is the angular sky resolution. The left plot of Fig.1.9 shows the light travel times between the different detector sites. It highlights the advantage of having a detector in India, which would lead to the longest possible baseline with a light travel time of over 30 ms from the two LIGO sites in the US. The effect of these long baselines on the sky localisation is highlighted in the right plot Fig.1.9, which shows the sky localisation of the first gravitational wave detection, GW150914 with the two advanced LIGO detectors that were operational at that point of time, versus what it could have been if there was a third detector in India at the same time.

Furthermore, the addition of gravitational wave detectors adds to the strength with which a signal is detected, something that will become clearer in Chap.2. This would allow us to better infer the properties of the source producing the signal, i.e., better parameter estimation. Finally, a global network of multiple detectors would allow us to extract the polarisations of gravitational waves. An overview

²⁷ <https://www.ligo.caltech.edu/news/ligo20170825>

²⁸ Yoichi Aso, Yuta Michimura, Kentaro Somiya, Masaki Ando, Osamu Miyakawa, Takanori Sekiguchi, Daisuke Tatsumi, Hiroaki Yamamoto, KAGRA Collaboration, et al. Interferometer design of the kagra gravitational wave detector. *Physical Review D*, 88(4):043007, 2013

²⁹ Bala Iyer, T Souradeep, CS Unnikrishnan, S Dhurandhar, S Raja, A Sengupta, IndIGO Consortium, et al. Ligo-india. Report No. LIGO-M1100296 (*Indian Initiative in Gravitational-wave Observations*, 2011), 2011; and CS Unnikrishnan. Indigo and ligo-india: Scope and plans for gravitational wave research and precision metrology in india. *International Journal of Modern Physics D*, 22(01):1341010, 2013

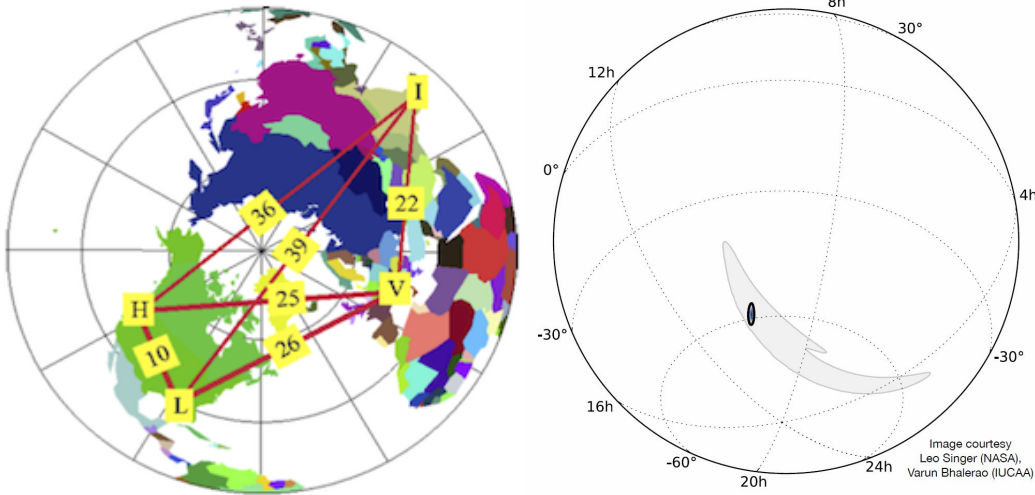


Figure 1.9: *Left Plot:* Baselines of a future global detector network projected onto the globe. H,L,V, and I indicate the sites for the LIGO detectors in Hanford and Livingston, Virgo detector in Italy and the proposed LIGO-India detector in India. The light-travel time (in milliseconds) of each baseline is also shown (Picture courtesy: B. S. Sathyaprakash). *Right Plot:* Improvement in the localisation of GW150914 by adding LIGO India. The small oval represents the size of the search area if LIGO India had been operating at the time of the detection. (Caption courtesy: <https://www.ligo.caltech.edu/news/ligo20160404>)

on future detectors is given in Sec.1.5.

1.3.5 Detection

The observation of gravitational waves relies heavily on the accuracy of waveforms describing the source. Such waveform templates are constructed using a combination of modelling using GR and input from astrophysics. The process of detection involves cross-correlating these templates with the data in a process called *matched-filtering*³⁰ to obtain candidates for actual gravitational wave detections. Among the various sources of gravitational waves, CBCs composed of black holes are the best-modelled sources in GR, because black holes can be approximated as point-particles in GR. For binary neutron star systems or neutron star-black hole binaries, the finite size of a neutron star needs to be taken into account, which leads to tidal disruptions when the compact objects come close. Matter effects need to be included in the modelling of gravitational radiation from such binaries through the equation of state $p(\rho)$ of the neutron star (where p is the pressure and ρ is the density) which is an active area of research. For other sources, like the gravitational collapse of a star, a lot of the physics governing the underlying process is still unknown, and their descriptions require us to make various assumptions about the source with input from astrophysics, particle physics and hydrodynamics.

Once an confident observation is made, one then uses well-established

³⁰ Sathyaprakash and Schutz 109

techniques of parameter estimation (described in more detail in Chapt.2) to infer properties of the source ³¹. This information is then used to extract scientific information from these observations, among them being to make statements about the validity of GR in the strong field regime of gravity, a topic we will discuss in detail in Sec. 2.2.

The information carried by gravitational waves is completely independent from the electromagnetic or the neutrino windows. In some cases information from multiple windows of observation complement each other to give us the most complete picture of the source. This is called *multi-messenger astronomy*. However, in some cases, gravitational waves have advantages over other messengers. Gravitational waves interact weakly with matter, as mentioned above, and hence they undergo lesser scattering with intervening matter than other messengers. This allows them to travel unchanged over long distances, and carry information from rare events which can then be extracted and used to reconstruct the science summary of the observation, including statements on theoretical physics, nuclear physics, astrophysics, cosmology etc, as we shall see in Sec.1.4.

1.4 Overview of LIGO/Virgo events

On September 14, 2015, gravitational waves from the coalescence of two stellar-mass black holes were observed by the twin detectors of the Advanced LIGO network at Hanford and Livingston, in the United States ³². This event, called GW150914, was followed by the observation of four other binary black hole mergers ³³, a binary black hole candidate ³⁴ and a binary neutron star merger ³⁵. Among them, the latest binary black hole merger (GW170814) ³⁶ and the binary neutron star event were observed in association with the Advanced Virgo detector in Cascina, Italy. These observations have established the beginning of an exciting new era of astronomy using gravitational waves.

1.4.1 Science summary of observations

The observation of GW150914 was not just the first direct detection of gravitational waves on Earth, it was also the first direct detection of a binary black hole merger. The two black holes had masses $(36, 29)M_{\odot}$ and the final remnant object had a mass of $62M_{\odot}$.

³¹ Benjamin P Abbott, R Abbott, TD Abbott, MR Abernathy, F Acernese, K Ackley, C Adams, T Adams, P Addesso, RX Adhikari, et al. Properties of the binary black hole merger gw150914. *Physical review letters*, 116(24):241102, 2016

³² Benjamin P Abbott et al. Observation of gravitational waves from a binary black hole merger. *Physical review letters*, 116(6):061102, 2016

³³ Abbott et al. 12, 11, 16, 17, 18

³⁴ Abbott et al. 11

³⁵ Abbott et al. 19

³⁶ Abbott et al. 18

These were the most massive stellar-mass black holes observed till date. Prior to GW150914, measurements of stellar-mass black holes in galactic x-ray binaries suggested masses in the range $10 - 15M_{\odot}$ ³⁷. However, since then, the observations of five other binary black hole mergers and a candidate for a binary black hole merger have established that there exists a population of black holes in the mass range $\sim 20 - 70M_{\odot}$. While GW150914 is the heaviest merger that we have seen so far, GW170608 is possibly the lightest, with the secondary black hole having a mass $7_{-2}^{+2}M_{\odot}$, which is quite close to the proposed mass-gap between neutron stars and black holes³⁸. The latest published LIGO-Virgo results suggest that, given the observations so far, we can expect an intrinsic rate of $9 - 240$ binary black hole mergers per Gpc³ per year³⁹. In the upcoming years, as the sensitivity of the advanced detectors increase, their volume reach would also increase making them sensitive to a greater number of binary black hole mergers. Hence the expected rates of detection of binary black hole merger events by Advanced LIGO and Virgo in its third and subsequent observing runs, is also expected to increase. The high intrinsic merger rates also suggest that this population of relatively high-mass binary black hole systems would create a stochastic gravitational wave background, with amplitude higher than previously expected. Analyses using just binary black hole mergers⁴⁰ predicted an energy density spectrum in the most sensitive part of the Advanced LIGO-Virgo band for stochastic gravitational waves, around 25 Hz, to be $\Omega_{GW}(f = 25\text{Hz}) \sim 1.1 \times 10^{-9}$, which is potentially detectable in the next few years of operation of the advanced detectors.

The observations of gravitational wave events also allow us to infer about the formation channels and astrophysical environments of these binaries. There are two broad formation channels for stellar-mass black holes observed by LIGO and Virgo: dynamical assembly in dense stellar clusters or isolated evolution in galactic fields through a common envelope formation. There is an alternative to stellar-evolution models, which states that such binaries could have formed from primordial black holes⁴¹. Important information about the evolution of the binary and hence, its formation channel, would come from the measurements of the spins of the compact objects in the binary. Binaries formed in dense stellar environments are

³⁷ J Casares. J. casares and pg jonker, space sci. rev. 183, 223 (2014). *Space Sci. Rev.*, 183:223, 2014

³⁸ Will M Farr, Niharika Sravan, Andrew Cantrell, Laura Kreidberg, Charles D Bailyn, Ilya Mandel, and Vicky Kalogera. The mass distribution of stellar-mass black holes. *The Astrophysical Journal*, 741(2):103, 2011; and Feryal Özel, Dimitrios Psaltis, Ramesh Narayan, and Jeffrey E McClintock. The black hole mass distribution in the galaxy. *The Astrophysical Journal*, 725(2):1918, 2010

³⁹ Benjamin P Abbott, R Abbott, TD Abbott, MR Abernathy, F Acernese, K Ackley, C Adams, T Adams, P Addesso, RX Adhikari, et al. The rate of binary black hole mergers inferred from advanced ligo observations surrounding gw150914. *The Astrophysical journal letters*, 833(1):L1, 2016

⁴⁰ BP Abbott, Richard Abbott, TD Abbott, MR Abernathy, Fausto Acernese, Kendall Ackley, Carl Adams, Thomas Adams, Paolo Addesso, RX Adhikari, et al. Gw150914: Implications for the stochastic gravitational-wave background from binary black holes. *Physical review letters*, 116(13):131102, 2016

⁴¹ Simeon Bird, Ilias Cholis, Julian B Munoz, Yacine Ali-Haïmoud, Marc Kamionkowski, Ely D Kovetz, Alvise Raccanelli, and Adam G Riess. Did ligo detect dark matter? *Physical review letters*, 116(20):201301, 2016

more likely to have isotropic individual spins, while binaries formed through isolated evolution are expected to have individual spins aligned with the orbital angular momentum. Unfortunately, current gravitational wave observations have not been able to put strong constraints on the individual spins of the two black holes. This is because, the spins play a sub-dominant role in orbital evolution and thus their estimation becomes more difficult. All the measurements so far indicate that the initial black holes had spins consistent with zero. However, observations do provide a hint that there is a possibility that the spins might be misaligned which might favour an evolution channel through dynamical capture over isolated evolution. The wide range of masses for the initial black holes also tell us that they were formed from progenitors with a wide range of metallicities, i.e., the fractional mass of the star in elements heavier than hydrogen and helium. Stars lose mass through stellar winds. This mass-loss is proportional to its metallicity. Thus, it follows that heavier black holes are formed from stars with lower metallicity, which resulted in lower mass-loss in stellar winds before collapsing to form a black hole. The progenitors of GW170608⁴² could have contained relatively large amounts of heavier elements, compared to the progenitors of the black holes that led to GW150914⁴³. Finally, these observations also allowed us to perform the first strong-field tests of GR in the highly relativistic regime, which is described in more detail in Sec.2.2.3.

The observation of GW170817 was a singularly unique case. The signal was observed by the advanced LIGO-Virgo detector network with a combined SNR of 32, the loudest gravitational wave signal observed till date, and was consistent with a binary neutron star merger at a distance of 40 Mpc. However, 1.7 seconds after the gravitational wave trigger, a gamma-ray burst was observed by NASA's Fermi-GBM telescope, which was later established to have a common source with the gravitational wave signal, originating in the galaxy NGC-4993. Information from both gravitational and electromagnetic windows, involving the 3 gravitational wave detectors and over 70 electromagnetic observatories from around the world and in space, were combined to give the most complete description of the source and helped usher in the era of *multi-messenger astronomy*. The observation of GW170817 allowed us, for the first time, to mea-

⁴² Benjamin P Abbott et al. Gw170608: Observation of a 19-solar-mass binary black hole coalescence. *arXiv:1711.05578*, 2017

⁴³ BP Abbott, R Abbott, TD Abbott, MR Abernathy, F Acernese, K Ackley, C Adams, T Adams, P Addesso, RX Adhikari, et al. Astrophysical implications of the binary black hole merger gw150914. *The Astrophysical Journal Letters*, 818(2):L22, 2016

sure the cosmic expansion rate using gravitational waves⁴⁴. Schutz, in 1986⁴⁵, proposed a unique method of determining the Hubble constant, which measures the expansion rate of the universe, given information about the redshift and the distance to a source. Gravitational wave observations allow us to determine the distance to the source, while electromagnetic observations provide us with redshift information. Thus, for the case of GW170817, we could combine information about the luminosity distance d_L to the source from the gravitational wave observation with the redshift measurements of the galaxy NGC-4993, to get first estimates on the Hubble constant H_0 at $70.0_{8.0}^{+12.0} \text{ km s}^{-1} \text{ Mpc}^{-1}$ from multi-messenger astronomy. The observation of GW170817 also allowed us to make statements on the neutron star radii and equation of state, as previously discussed in Sec.1.3.5. Results seem to indicate that a more compact object with smaller radii is preferred, thus favouring softer equations of state over stiffer equations of state. A more detailed discussion is present in ⁴⁶. The detection of GW170817 also allowed us to revise our estimates on the amplitude of the stochastic background, which was earlier estimated just for binary black hole mergers. Now including the contribution to the stochastic background from binary neutron star mergers as well, the amplitude of the total astrophysical stochastic background is predicted at $\sim 1.8 \times 10^{-9}$ (with 90% confidence) ⁴⁷.

1.5 Future Prospects: Future Detectors

The current generation of advanced ground-based interferometric detectors are expected to be followed by a third-generation of ground-based interferometric detectors, set to come up near the late 2020s-early 2030s. These third-generation detectors, like the Einstein Telescope ⁴⁸ and the Cosmic Explorer ⁴⁹, are expected to be 10 times more sensitive than the current detectors (at design sensitivity) and thus will have ~ 1000 -fold increase in their volume reach. These detectors will be able to observe events more frequently at much higher signal-to-noise ratios (SNRs) than the second generation detectors. The increased observation rates will lead us to make more precise estimates of merger-rates of events in the universe and constrain possible deviations from GR by combining information from multiple observations. The increased SNRs will allow us to infer the proper-

⁴⁴ LIGO Scientific Collaboration, Virgo Collaboration, 1M2H Collaboration, Dark Energy Camera GW-EM Collaboration, DES Collaboration, DLT40 Collaboration, Las Cumbres Observatory Collaboration, VINROUGE Collaboration, MASTER Collaboration, et al. A gravitational-wave standard siren measurement of the hubble constant. *Nature*, 551(7678):85–88, 2017
⁴⁵ Bernard F Schutz. Determining the hubble constant from gravitational wave observations. *Nature*, 323(6086):310, 1986

⁴⁶ Benjamin P Abbott et al. Gw170817: observation of gravitational waves from a binary neutron star inspiral. *Physical Review Letters*, 119(16):161101, 2017; and BP Abbott, R Abbott, TD Abbott, F Acernese, K Ackley, C Adams, T Adams, P Addesso, RX Adhikari, VB Adya, et al. Gw170817: Measurements of neutron star radii and equation of state. *arXiv preprint arXiv:1805.11581*, 2018

⁴⁷ Benjamin P Abbott, R Abbott, TD Abbott, F Acernese, K Ackley, C Adams, T Adams, P Addesso, RX Adhikari, VB Adya, et al. Gw170817: implications for the stochastic gravitational-wave background from compact binary coalescences. *Physical review letters*, 120(9):091101, 2018

⁴⁸ Punturo et al. 105

⁴⁹ Dwyer et al. 66

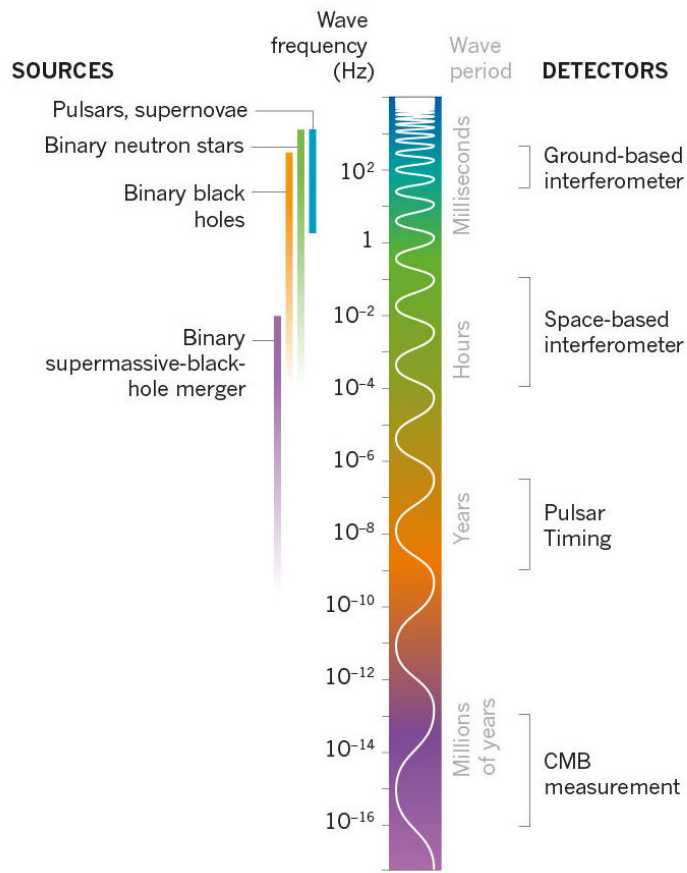


Figure 1.10: Gravitational wave spectrum. On the left of the illustration are listed the various gravitational waves sources in the increasing order of the frequency of gravitational waves wave emission. On the right, are listed the various detection methods for gravitational waves in the difference frequency bands. Figure courtesy: "How gravitational waves could solve some of the Universe's deepest mysteries" , B.Schutz (<https://www.nature.com/articles/d41586-018-04157-6>)

ties of the gravitational wave sources better than we can do now, and then use that information to constrain astrophysical formation scenarios. These detectors will also be able to see much further out into the universe as compared to the second-generation detectors which have a distance reach of about 15 Gpc for high-mass black holes, or roughly redshifts of ~ 2 . This will allow us to conduct more accurate cosmological studies related to the measurement of the Hubble constant and the expansion of the universe. The third-generation detectors are also expected to have sensitivities that reach as low as 1 Hz, allowing us the chance to perhaps observe intermediate mass black holes (IMBHs) with masses between stellar-mass black holes and super-massive black holes. There are also plans to have a space-based gravitational waves detector, called the Laser Interferometer Space Antenna (LISA)⁵⁰, a joint European Space Agency and NASA project, which will observe gravitational waves in the range $10^{-4} - 10^{-1}$ Hz. LISA will consist of three spacecrafts in an equilateral triangle (arm length $\sim 10^6$ km) with freely falling test masses and lasers bouncing off each other, orbiting the Earth. Referring to Fig. 1.10, we see that the most promising source of gravitational waves for LISA would be the merger of super-massive black hole binaries. The future of gravitational wave astronomy, that was born with the detection of GW150914 and established through the subsequent detections, is truly bright and exciting.

⁵⁰ Karsten Danzmann, LISA Study Team, et al. Lisa: Laser interferometer space antenna for gravitational wave measurements. *Classical and Quantum Gravity*, 13(11A):A247, 1996

Summary

The existence of gravitational waves is one of the most exciting predictions of Einstein's theory of general relativity. In the 100 years since their prediction, the pursuit of the observation of gravitational waves has led to remarkable developments in our knowledge about the source of these gravitational waves, as well as ground-breaking technical developments in building instruments that could detect them. This culminated in the first direct observation of gravitational

waves on Earth using the Advanced LIGO detectors in September, 2015. The five subsequent observations of compact binary coalescences by the Advanced LIGO-Virgo detector network have firmly established the field of gravitational waves and multi-messenger astronomy. Over the coming years, the detectors, which have just finished two full science runs, are expected to improve their sensitivity, as well as grow in number. We have just opened a new window onto the universe whose scientific potential takes us a step further in better understanding our universe.

2 | Bayesian Inference: Inferring Physics and Astrophysics from Gravitational Wave Observations

2.1 Bayesian Inference

The first step to extracting scientific information from a gravitational wave observation is understanding the nature of the source that produced it. The properties of the source are estimated within the framework of Bayesian inference. This knowledge can then be used, among other things, to test if GR is indeed the correct theory to describe such gravitational wave sources. This chapter is broadly divided into two parts. The first part describes, in detail, Bayesian inference and its various components, while the second part deals with the area of testing GR, in general, and testing GR using gravitational wave observations, in particular.

2.1.1 Detector Data

The twin detectors of the Advanced LIGO network in the US at Hanford, Washington and Livingston, Louisiana, and the Advanced Virgo detector in Italy, record differential changes in length, $\delta L(t)$ between their two arms. Given the length of each arm of the detector L , the gravitational wave *strain*, as introduced at the end of Sec.1.3.2, can be written as ¹:

$$h(t) = \frac{\delta L(t)}{L} = F_+(\theta, \phi, \psi)h_+(t) + F_\times(\theta, \phi, \psi)h_\times(t) \quad (2.1)$$

where h_+, h_\times are the two independent polarisation amplitudes of the gravitational wave, and $\{F_+, F_\times\}$ are the detector antenna pattern response functions defined in Sec.1.3.2, and depends on the sky

¹ B.S. Sathyaprakash and B.F. Schutz. Physics, Astrophysics and Cosmology with Gravitational Waves. *Living Rev. Relat.*, 12:2, 2009

position and the polarisation of the gravitational wave source. The interferometer noise $n(t)$ described in Sec. 1.3.3, is assumed to be a stationary, ergodic Gaussian random process with zero mean and a PSD, $S_n(f)$, defined as:

$$\langle \tilde{n}^*(f) \tilde{n}(f') \rangle = \frac{1}{2} S_n(f) \delta(f - f') \quad (2.2)$$

and as shown in Fig. 1.8. Here, $\tilde{n}(f)$ is the Fourier transform of $n(t)$, the angular brackets in Eq. 2.2 define an ensemble average and $\delta(f - f')$ is the Dirac delta function.

The actual astrophysical gravitational wave strain $h(t)$ however differs from the measured strain $h^M(t)$. The interferometer records its response $d(t)$ to the passage of a gravitational wave, as changes in the intensity of the interfering laser beams at the point where they recombine – the photodiode of the gravitational wave readout port ². This is related to the Fourier transform of the astrophysical strain $\tilde{h}(f)$ through the response function $R(f)$ as:

$$\tilde{h}(f) = \frac{1}{L} R(f) \tilde{d}(f) \quad (2.3)$$

where $\tilde{d}(f)$ is the Fourier transform of $d(t)$. In order to get $\tilde{h}(f)$ from $\tilde{d}(f)$, one requires an appropriate model for the response function $R(f)$. The specific model of $R(f)$ that is used for interferometer calibration has its associated uncertainties, introducing an error in the calibrated $\tilde{h}(f)$ signal. We model these calibration errors using a complex function in frequency domain with amplitude $\delta A(f; \vec{\theta}^{\text{cal}})$ and phase $\delta \phi(f; \vec{\theta}^{\text{cal}})$ as:

$$\tilde{h}^M(f) = \tilde{h}(f) [1 + \delta A(f; \vec{\theta}^{\text{cal}})] \exp[i \delta \phi(f; \vec{\theta}^{\text{cal}})] \quad (2.4)$$

where $\tilde{h}^M(f)$, $\tilde{h}(f)$ are the Fourier transforms of $h^M(t)$, $h(t)$ respectively, and $\vec{\theta}^{\text{cal}}$ is the set of calibration parameters ³. From here on, whenever we will refer to strain, we will be referring to the measured strain $h^M(t)$, and hence for convenience in writing notation, drop the superscript M and refer to it as just $h(t)$.

²BP Abbott, R Abbott, TD Abbott, MR Abernathy, K Ackley, C Adams, P Addesso, RX Adhikari, VB Adya, C Affeldt, et al. Calibration of the advanced ligo detectors for the discovery of the binary black-hole merger gw150914. *Physical Review D*, 95(6): 062003, 2017

³BP Abbott, R Abbott, TD Abbott, MR Abernathy, K Ackley, C Adams, P Addesso, RX Adhikari, VB Adya, C Affeldt, et al. Calibration of the advanced ligo detectors for the discovery of the binary black-hole merger gw150914. *Physical Review D*, 95(6): 062003, 2017

2.1.2 Waveform models for binary black hole coalescences

A gravitational wave signal from a binary black hole coalescence (in a quasi-circular orbit) may be completely described in GR using the

following parameters:

- Component masses m_1 and m_2 , where $m_1 \geq m_2$ (by convention). During the early inspiral phase, the evolution of the binary, at the leading order, depends only on a specific combination of the component masses called the *chirp mass* \mathcal{M}_c (mentioned earlier in Sec.1.2.4):

$$\mathcal{M}_c := (m_1 m_2)^{(3/5)} (m_1 + m_2)^{(-1/5)} \quad (2.5)$$

Hence, information about the masses is sometimes re-parametrised in terms of the chirp mass \mathcal{M}_c , along with the symmetric mass ratio η or the asymmetric mass ratio q defined as:

$$\eta := \frac{m_1 m_2}{(m_1 + m_2)^2} \quad (2.6)$$

$$q := m_1 / m_2 \quad (2.7)$$

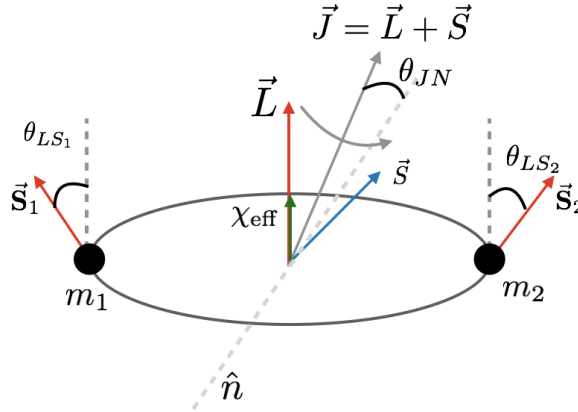


Figure 2.1: Orbital parameters of a binary black hole system

- Component spins vectors \mathbf{S}_1 and \mathbf{S}_2 . Information about the spins of the individual black holes shed light on the astrophysical formation scenarios of such binary black hole systems as mentioned in Sec.1.4. However, they are difficult to determine because of the sub-dominant nature of their role in orbital dynamics. We can instead measure a mass-weighted combination of the components of the spins in the direction of the orbital angular momentum of the system, \vec{L} , called the *effective spin* parameter ⁴:

$$\chi_{\text{eff}} := \frac{m_1 a_1 (\hat{L} \cdot \hat{S}_1) + m_2 a_2 (\hat{L} \cdot \hat{S}_2)}{m_1 + m_2} \quad (2.8)$$

where \hat{L} and \hat{S}_i are the unit vectors in the direction of the \vec{L} and the

⁴ Thibault Damour. Coalescence of two spinning black holes: An effective one-body approach. *Physical Review D*, 64 (12):124013, 2001

individual spins S_i , with $i = 1$ for the primary black hole and $i = 2$ for the secondary black hole; $a_i = |cS_i/Gm_i^2|$ is the dimensional spin magnitude with a range $[0, 1]$. The in-plane components of the spin lead to the precession of the orbit. The precession of the system is characterised through an *effective precession* parameter χ_p ⁵, defined as:

$$\chi_p := \max\left(\chi_{1\perp}, \frac{3+4q}{4+3q}q\chi_{2\perp}\right) \quad (2.9)$$

where $\chi_{i\perp}$ are the magnitudes of the components of the dimensionless spins which are perpendicular to orbital angular momentum \vec{L} , and q is the asymmetric mass ratio defined earlier.

- The position of the source. This is defined through the luminosity distance d_L , right ascension α and the declination δ .
- The orientation of the source. This is defined through the inclination of the source ι , which is the angle between the orbital angular momentum \vec{L} and the line of sight \hat{n} , and the polarisation ψ (as defined in ⁶), the orientation of the projection of the orbital angular momentum onto the plane of the sky. In the absence of precession, the inclination ι is equal to θ_{JN} (Fig. 2.1).
- The time of coalescence t_c and the phase ϕ_c at t_c , called the phase at coalescence.

Hence a spinning binary black hole system in a quasi-circular orbit is completely described in GR by this set of 15 parameters. We need to add the parameters describing calibration uncertainties to this as well. Let us denote the complete parameter set by ξ . Hence the strain h due to the passage of a gravitational wave is a function of ξ , i.e., $h(t; \xi)$ (time-domain waveform) or $\tilde{h}(f; \xi)$ (frequency-domain waveform). There are various models available that describe the evolution of a binary black hole system to various levels of accuracy. Some of these waveforms are implemented in the LIGO Algorithms Library (LAL), in a submodule called LALSimulation, and are of two broad classes: a phenomenological class of waveforms, and a second class based on the effective one-body formalism calibrated to numerical relativity simulations.

⁵ Patricia Schmidt, Mark Hannam, and Sascha Husa. Towards models of gravitational waveforms from generic binaries: A simple approximate mapping between precessing and non-precessing inspiral signals. *Phys. Rev. D*, 86: 104063, 2012. DOI: 10.1103/PhysRevD.86.104063

⁶ Warren G Anderson, Patrick R Brady, Jolien DE Creighton, and Eanna E Flanagan. Excess power statistic for detection of burst sources of gravitational radiation. *Physical Review D*, 63(4):042003, 2001

2.1.3 Parameter Estimation

Given the detector data d , one can adopt a Bayesian framework to estimate the parameter set ξ . Bayes' theorem states that the posterior probability distribution of a parameter set $\xi := \{\xi_i\}$ of a model hypothesis \mathcal{H} , given data d and any other information I , is:

$$P(\xi|d, \mathcal{H}, I) = \frac{P(\xi|\mathcal{H}, I) \mathcal{L}(d|\xi, \mathcal{H}, I)}{P(d|\mathcal{H}, I)}, \quad (2.10)$$

where $P(\xi|\mathcal{H}, I)$ is the *prior* probability of the parameter set ξ given \mathcal{H} and I , while $\mathcal{L}(d|\xi, \mathcal{H}, I)$ is called the *likelihood* function, which is the probability of observing the data d , given ξ , \mathcal{H} and I . What appears in the denominator is a normalization constant $P(d|\mathcal{H}, I) := \int P(\xi|\mathcal{H}, I) \mathcal{L}(d|\xi, \mathcal{H}, I) d\xi$, called the marginal likelihood, or the *evidence* of the hypothesis \mathcal{H} .

If our hypothesis \mathcal{H} is that the data contains a gravitational wave signal described by a GR waveform model $h(\xi)$ and stationary Gaussian noise described by the PSD $S_n(f)$, then, as described in appendix A of 7, the likelihood function can be defined as:

$$\mathcal{L}(d|\xi, \mathcal{H}, I) \propto \exp \left[-\frac{1}{2} \langle d - h(\xi) | d - h(\xi) \rangle \right], \quad (2.11)$$

where $\langle \cdot | \cdot \rangle$ is the following noise-weighted inner product

$$\langle B|C \rangle := 2 \int_{f_{\text{low}}}^{f_{\text{cut}}} \frac{\tilde{B}^*(f)\tilde{C}(f) + \tilde{B}(f)\tilde{C}^*(f)}{S_n(f)} df. \quad (2.12)$$

Above, $\tilde{B}(f)$ denotes the Fourier transform of $B(t)$ and a $*$ denotes complex conjugation. The limits of integration f_{low} and f_{cut} are dictated by the bandwidth of the detector sensitivity, the bandwidth of the signal, as well as the cutoff frequencies in our calculations (described in Chap.3). Owing to the large dimensionality of the parameter set ξ , the posterior distribution $P(\xi|d, \mathcal{H}, I)$ in Eq. (2.10) is computed by stochastically sampling the parameter space using techniques such as Markov-Chain Monte Carlo (MCMC)⁸ or nested sampling⁹. The submodule inside LAL which implements Bayesian inference is called LALInference¹⁰. Two of the samplers currently implemented in LALInference are discussed below, an MCMC based algorithm called LALInferenceMCMC and a Nested Sampling based algorithm called LALInferenceNest.

⁷ Curt Cutler and Eanna E. Flanagan. Gravitational waves from merging compact binaries: How accurately can one extract the binary's parameters from the inspiral wave form? *Phys. Rev. D*, 49:2658–2697, 1994. DOI: 10.1103/PhysRevD.49.2658

⁸ Phil Gregory. *Bayesian Logical Data Analysis for the Physical Sciences: A Comparative Approach with Mathematica® Support*. Cambridge University Press, 2005

⁹ John Skilling et al. Nested sampling for general bayesian computation. *Bayesian analysis*, 1(4):833–859, 2006

¹⁰ J. Veitch et al. Parameter estimation for compact binaries with ground-based gravitational-wave observations using the LALInference software library. *Phys. Rev. D*, 91(4):042003, February 2015. DOI: 10.1103/PhysRevD.91.042003

As we have seen above, a gravitational wave signal from a binary black hole signal is completely described by the parameter set ξ . Hence $P(\xi|d, \mathcal{H}, I)$ is a multi-dimensional probability distribution. The posterior probability distribution over a subset of this multi-dimensional parameter set can be obtained by marginalising over the remaining *nuisance* parameters:

$$P(\xi_1|d, \mathcal{H}, I) = \int d\xi_2 d\xi_3 d\xi_4 \dots P(\xi|d, \mathcal{H}) \quad (2.13)$$

Eq. 2.13 gives us the marginalised one-dimensional posterior probability distribution over the parameter ξ_1 by integrating over the contributions of the remaining parameters.

2.1.4 Hypothesis testing

For the case of parameter estimation, we assumed that our binary black hole system is completely described using our hypothesis or *model*, which is GR. Given the data, Bayesian inference also allows us to compare this hypothesis with the predictions of gravitational waves in an alternate theory of gravity. Let us call GR as \mathcal{H}_0 and the alternate theory or hypothesis as \mathcal{H}_1 . One proceeds to do the problem of model selection by comparing the *evidences* $P(d|\mathcal{H}, I)$ for both hypotheses, defined as:

$$Z = P(d|\mathcal{H}, I) = \int P(\xi|\mathcal{H}, I) \mathcal{L}(d|\xi, \mathcal{H}, I) d\xi \quad (2.14)$$

through the computation of the odds ratio O_{01} :

$$O_{01} = \frac{P(\mathcal{H}_0|d, I)}{P(\mathcal{H}_1|d, I)} = \frac{P(\mathcal{H}_0|I) Z_0}{P(\mathcal{H}_1|I) Z_1} \quad (2.15)$$

where $P(\mathcal{H}_i|I)$ is the prior, and Z_i is the evidence on hypothesis \mathcal{H}_i , $i = 0$ is GR and $i = 1$ is some alternate theory of gravity.

Sometimes, one might just be interested in checking the implicit truth of \mathcal{H}_0 . In that case, we assume \mathcal{H}_1 to be the hypothesis where \mathcal{H}_0 is false: $\mathcal{H}_1 = \bar{\mathcal{H}}_0$, and proceed to do model selection. Such a model selection problem is called a *null-hypothesis* testing. We will see later that in the absence of reliable predictions of gravitational waves in many alternate theories of gravity, most of the current strong field tests are *null tests*, i.e., they are hypothesis testing problems with the null hypothesis, GR.

MCMC

Markov chain Monte Carlo algorithms generate the desired samples by constructing a kind of random walk in the model parameter space such that the probability for being in a region of this space is proportional to the posterior density for that region¹¹. The random walk is accomplished using a Markov chain, whereby the new sample, ξ_{i+1} , depends on the previous sample ξ_i according to an entity called the transition kernel, $p(\xi_{i+1}|\xi_i)$. The remarkable property of $p(\xi_{i+1}|\xi_i)$ is that after an initial burn-in period (which is discarded) it generates samples of ξ with a probability density equal to the desired posterior $P(\xi|d)$. The simplest MCMC algorithm is the *Metropolis-Hastings* algorithm, where a proposed value for ξ_{i+1} , say Y , is picked from a *proposal distribution* $q(Y|\xi_i)$ (can have almost any form), and *accepted* on the basis of the Metropolis ratio:

$$r = \frac{p(Y|D, I)q(\xi_i|Y)}{p(\xi_i|D, I)q(Y|\xi_i)} \quad (2.16)$$

where the *acceptance probability* $\alpha(\xi_i, Y)$ is defined as:

$$\alpha(\xi_i, Y) = \min(1, r) \quad (2.17)$$

A slightly more advanced version of the above algorithm involving parallel-tempering is implemented in LALInference, and is called LALInferenceMCMC.

Nested Sampling^{12,13}

We have seen above that parameter estimation requires sampling of the likelihood function over a parameter space which might be as large as 15-dimensional. This is computationally expensive. Similarly, for hypothesis-testing, we need to compute the evidence, which involves an integral over a large-dimensional space. Nested sampling is an algorithm that allows us to efficiently obtain both quantities. As mentioned earlier the evidence can be written as:

¹¹ Phil Gregory. *Bayesian Logical Data Analysis for the Physical Sciences: A Comparative Approach with Mathematica® Support*. Cambridge University Press, 2005

¹² John Skilling et al. Nested sampling for general bayesian computation. *Bayesian analysis*, 1(4):833–859, 2006

¹³ This section on the Nested Sampling algorithm is heavily influenced by Prof. Chris Van Den Broek's lecture notes, from the Summer school on gravitational wave astronomy at ICTS, in June 2016.

$$P(d|\mathcal{H}, I) := \int P(\xi|\mathcal{H}, I) \mathcal{L}(d|\xi, \mathcal{H}, I) d\xi \quad (2.18)$$

$$= \int \pi(\xi) \mathcal{L}(\xi) d\xi \quad (2.19)$$

Nested sampling computes evidence by rewriting the above integration in terms of a single scalar mass X , defined as the fraction of volume with likelihood greater than some values λ :

$$X(\lambda) := \int \int \dots \int_{\mathcal{L}(\xi) > \lambda} \pi(\xi) d\xi \quad (2.20)$$

Thus, an element of prior mass is defined as:

$$dX = \pi(\xi) d\xi \quad (2.21)$$

Since the prior is normalised, X lies in the interval $[0, 1]$, where the lower bound $X = 0$ corresponds to the surface which does not enclose any point with a higher likelihood, i.e., $\lambda = \mathcal{L}_{max}$, while the upper bound $X = 1$ corresponds to the surface enclosing all points with a higher likelihood, i.e., $\lambda = \mathcal{L}_{min}$. The evidence can now be rewritten as:

$$Z := \int \pi(\xi) \mathcal{L}(\xi) d\xi = \int \tilde{\mathcal{L}}(X) dX \quad (2.22)$$

from which the posterior can be trivially obtained as:

$$\tilde{P}(X) = \frac{\tilde{\mathcal{L}}(X)}{Z} \quad (2.23)$$

Thus the idea behind the nested sampling algorithm is to construct the function $\tilde{\mathcal{L}}(X)$ by progressively finding locations in parameter space with higher likelihood and thus, progressively smaller prior mass and then use the above formulae to compute the evidence and then the posterior probability distribution.

2.2 Testing General Relativity

2.2.1 Classical Tests of General Relativity

When Einstein published his theory of GR, he also suggested three possible experimental verifications of the predictions of the theory. These three tests are collectively called the *classical* tests of GR^{14,15}.

¹⁴ S Weinberg. Gravitation and cosmology. ed. John Wiley and Sons, New York, 1972

¹⁵ These tests are also called the solar system tests of GR.

- Perihelion precession of the orbit of Mercury:** Following the Kepler's laws of planetary motion, Mercury orbits the Sun in an elliptical orbit, where the point of closest approach is called the perihelion (Fig.2.2). In Newtonian classical mechanics, the perihelion of a planet's orbit is expected to precess because of the gravitational interaction with other planets as well as due to solar oblateness. However, the precession of the perihelion of Mercury deviates from the predictions of Newtonian theory by an amount measured at $43.11'' \pm 0.45$ per century. This precession can only be explained in GR on account of Mercury moving in the curved spacetime of the Sun. When Einstein published his theory, he computed this precession which came out to be $42''$, in excellent agreement with observation¹⁶. The predicted value has since been recalculated to a remarkable degree of agreement in the last 100 years with observations using radar measurements.

¹⁶ Albert Einstein. Die grundlage der allgemeinen relativitätstheorie. *Annalen der Physik*, 354(7):769–822, 1916

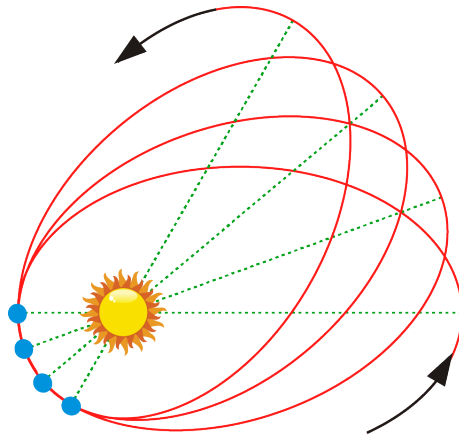


Figure 2.2: The point of closest approach to the Sun is called the perihelion, and occurs in a certain direction (green dashed lines). Over time, an orbit pivots slowly - it precesses - changing the direction to perihelion. Caption and figure courtesy <https://writescience.wordpress.com/2015/02/07/gravity-04-testing-the-new-gravity>

- Gravitational lensing by the sun:** In GR, light travels along the null geodesic from the source to the observer. In the presence of a massive object or *lens*, spacetime gets curved and the light, in travelling through this curved spacetime, gets bent around the intervening object on its way from the source to the observer. This phenomenon is called *gravitational lensing*. The greater the mass of the lens, greater is the deflection of light. In 1915, the most massive object in the vicinity of the Earth that could have been used to measure lensing was the Sun. So Einstein had calculated the deflection of light from stars near the vicinity of the surface of the Sun. This was experimentally verified during an expedition led by

Arthur Eddington to the island of Principe, off the west coast of Africa, during the total solar eclipse of May, 1919. The blocking of the sunlight allowed him to compare the positions of certain stars close to the rim of the sun, with their positions in the absence of the sun, and find remarkable agreement with the predictions of GR for their angular displacements due to gravitational lensing. The publishing of Eddington's results ¹⁷ was the first definitive experimental proof of GR and launched Einstein into worldwide fame.

- **Gravitational redshift of spectral lines:** The prediction of the gravitational redshift of spectral lines is a consequence of the Equivalence Principle, predicted by Einstein in 1907, which states: "At every spacetime point in an arbitrary gravitational field it is possible to choose a locally inertial coordinate system, such that, within a sufficiently small region of the point in question, the laws of nature take the same form as in unaccelerated Cartesian coordinate systems in the absence of gravitation" ¹⁸. The Doppler shift in the spectral lines of the source can be written as:

$$\frac{\Delta\nu}{\nu} = \phi(x_2) - \phi(x_1) \quad (2.24)$$

where $\phi(x)$ is the Newtonian potential at a point x in the gravitational field, and (x_1, x_2) are two points at the surface of the source, and far from it, respectively. This Doppler shift in the spectral lines was first observed for the case of white dwarf Sirius B and Eridani B, by J. Adams, 1925 ¹⁹, and has since been confirmed for many different sources in the universe.

Among the notable terrestrial tests performed to verify the gravitational redshift of spectral lines were a series of experiments performed between 1959 and 1965 by Pound, Rebka and Snider, which ushered in an era of *precision* tests of relativity. The Pound-Rebka experiment of 1959 ²⁰ involved measurements of the Doppler shift in the wavelength of ⁵⁷Fe gamma-ray photons generated with the Mossbauer effect, over a vertical height of 22.5 metres as the photons travelled between two sources situated at the top and bottom of Harvard University's Jefferson tower. The accuracy of this experiment was around 1%, which was made better by an improved experiment by Pound and Snider in 1965 ²¹. Subse-

¹⁷ Mr C Davidson. IX. a determination of the deflection of light by the sun's gravitational field, from observations made at the total eclipse of may 29, 1919. *Phil. Trans. R. Soc. Lond. A*, 220(571-581):291-333, 1920

¹⁸ S Weinberg. Gravitation and cosmology. ed. John Wiley and Sons, New York, 1972

¹⁹ Norriss S Hetherington. Sirius b and the gravitational redshift-an historical review. *Quarterly Journal of the Royal Astronomical Society*, 21:246-252, 1980

²⁰ Robert V Pound and Glen A Rebka Jr. Gravitational red-shift in nuclear resonance. *Physical Review Letters*, 3(9):439, 1959

²¹ Robert V Pound and JL Snider. Effect of gravity on nuclear resonance. *Physical Review Letters*, 13(18):539, 1964

quent redshift experiments using hydrogen maser clocks on rockets which compared its rates with identical clocks on the ground helped achieve precision of less than 0.007%²².

2.2.2 Binary pulsar tests of General Relativity

The first indirect evidence of the existence of gravitational waves was observed in the binary pulsar system PSR B1913+16, discovered by Russell Hulse and Joseph Taylor in 1974²³. Binary pulsars are systems of neutrons stars/white dwarfs, where atleast one of them emit a strong beam of electromagnetic radiation that passes through our line of sight. The pulses are regular to a remarkable experimental precision making pulsars one of the best clocks in the universe. The pulses help us to measure the time period of revolution P_b , of the binary pulsar system, and using the post-Newtonian approximation, one can infer all the properties of the binary system, including the masses of the two stars and the orbital parameters. Now, as we have seen in Sec.1.2.4, such systems are expected to emit radiation in the form of gravitational waves, which leads to the shrinking of the orbit, leading to a decay in the orbital period given by Eq.1.33. Assuming a representative value of $1.4M_\odot$ for the mass of the neutron star, the relativistic prediction of the rate of decay of the orbit \dot{P}_b is -2.4×10^{-12} . This is in remarkable agreement with observation which has measured the decay to be $(2.4184 \pm 0.0009) \times 10^{-12}$ ²⁴. In fact, the decay in the orbital period of the PSR B1913+16 system was studied over a period of over 30 years²⁵. For the discovery of this system and providing the first experimental evidence for the existence of gravitational waves, Russell Hulse and Joseph Taylor were awarded the Nobel Prize in Physics, in 1992²⁶.

2.2.3 Strong field tests of General Relativity

One fact common to all the tests mentioned up till this point, is that they all describe tests of GR in the weak field regime. The strength of the gravitational field around a source can be characterised by the compactness of the source $\epsilon \sim M/R$, where M, R are the mass and radius of the compact source. Binaries of neutron stars and/or black holes are the most compact sources of gravitational waves, with compactness ranging from 0.2 to 0.5. Compared to compactness of

²² Robert FC Vessot, Martin W Levine, Edward M Mattison, EL Blomberg, TE Hoffman, GU Nystrom, BF Farrel, Rudolph Decher, Peter B Eby, CR Baugher, et al. Test of relativistic gravitation with a space-borne hydrogen maser. *Physical Review Letters*, 45 (26):2081, 1980

²³ R. A. Hulse and J. H. Taylor. Discovery of a pulsar in a binary system. *The Astrophysical Journal*, 195: L51, jan 1975. ISSN 0004-637X. DOI: 10.1086/181708. URL <http://adsabs.harvard.edu/doi/10.1086/181708>

²⁴ Joel M Weisberg, Joseph H Taylor, and Lee A Fowler. Gravitational waves from an orbiting pulsar. *Scientific American*, 245(4):74-83, 1981; Joseph H Taylor and Joel M Weisberg. Further experimental tests of relativistic gravity using the binary pulsar psr 1913+ 16. *The Astrophysical Journal*, 345:434-450, 1989; and Joel M Weisberg, David J Nice, and Joseph H Taylor. Timing measurements of the relativistic binary pulsar psr b1913+ 16. *The Astrophysical Journal*, 722(2):1030, 2010

²⁵ Joel M Weisberg and Joseph H Taylor. Relativistic binary pulsar b1913+ 16: Thirty years of observations and analysis. *arXiv preprint astro-ph/0407149*, 2004

²⁶ RA Hulse and JH Taylor Jr. Nobel prize press release, 1993

$\epsilon \sim 10^{-6}$ for the binary pulsar systems (e.g., the Hulse-Taylor Pulsar) or $\sim 10^{-8}$ for the Mercury-Sun system, $\epsilon \sim 1$ describes regions of strong field gravity. Furthermore, during the final stages of coalescence, the compact objects move at highly relativistic speeds of upto $\sim 0.5c$ (bottom panel of Fig. 4.1). Hence, the observations of CBCs can be used to test GR, for the first time, in the highly relativistic and strong field regimes of gravity.

2.2.4 Null tests of General Relativity in the strong field regime

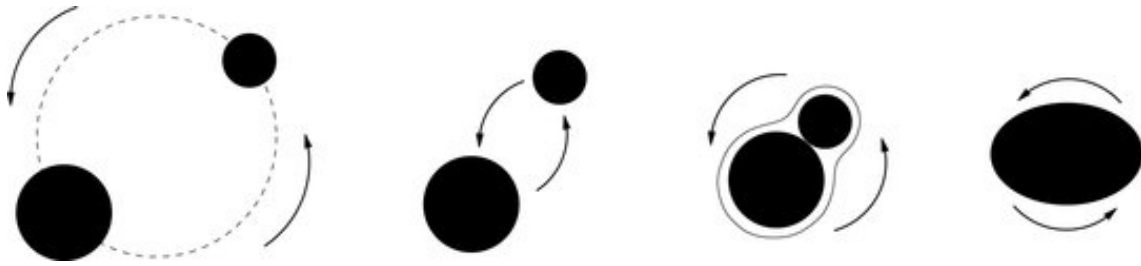


Figure 2.3: Stages of black-hole binary coalescence: (from left to right) inspiral, plunge, merger, and ringdown. Courtesy: A. Taracchini/AEI

A binary black hole coalescence evolves over three phases as shown in the figure: an *inspiral*, where the two black holes move around each other in a gravitationally bound orbit, and spiral in due to the emission of gravitational waves, the *merger* when a common horizon is formed, and *ringdown* when the recently merged object radiates away its asymmetries through a spectrum of QNMs and settles down to a stable Kerr black hole. Several strong-field tests of GR have already been performed using the above observations of CBCs²⁷. Since not many alternative theories of gravity have reliable predictions of gravitational waves from binary black hole mergers, most of the current strong-field tests are "null tests" of GR. A handful of tests have been performed to check the consistency of the observed signals with those predicted by GR. In particular, due to the large masses of the black holes in GW150914, the observed signal consists of signatures from the inspiral and merger of the two black holes and the subsequent ringdown of the final black hole. This allowed us to perform several consistency tests making use of one or more phases of the coalescence: The first involved testing the consistency between the mass and spin of the final remnant, determined from the low-frequency (inspiral) and high-frequency (post-inspiral) parts of the observed signal²⁸. The second involved testing the consistency of

²⁷ Abbott et al. 14, 11, 16, 18, 25

²⁸ Abhirup Ghosh, Archisman Ghosh, Nathan K Johnson-McDaniel, Chandra Kant Mishra, Parameswaran Ajith, Walter Del Pozzo, David A Nichols, Yanbei Chen, Alex B Nielsen, Christopher PL Berry, et al. Testing general relativity using golden black-hole binaries. *Physical Review D*, 94(2):021101, 2016

the data after the peak of the observed signal (corresponding to the merger) with a quasi-normal mode (QNM) spectrum predicted by GR²⁹. The third involved bounding deviations from the GR predictions of the post-Newtonian (PN) coefficients describing the inspiral (and from phenomenological parameters describing the merger and ringdown) using parametrized waveform models³⁰. The fourth involved constraining the amount of dispersion in the observed gravitational wave signal and converting it to a bound on the mass of the graviton³¹. In addition, the residuals after subtracting the best fit GR signal have been found to be consistent with detector noise.

Additional tests of GR were performed using the subsequent GW observations. The large distance of GW170104 allowed us test whether gravitational waves get dispersed (i.e. components with different frequencies travel at different speeds) as it travels over billions of light years from the source to us³². It can be shown, by assuming a simple model for the dispersion, motivated by some alternate theories of GR which predict such dispersion, that the results are indeed consistent with the gravitational wave signal GW170104 not being dispersed. The three-detector observation of GW170814 allowed us to study the polarisation of gravitational waves for the first time.³³ The joint observation of the binary neutron star merger, GW170817 in both the gravitational wave and electromagnetic windows had important implications on fundamental physics³⁴: put a bound on the speed of gravity, as well as further test Lorentz invariance and the Equivalence Principle. Within the statistical uncertainties, these investigations provided no evidence for deviations from GR. Some of the tests, described about the binary black hole coalescences have been repeated for multiple LIGO-Virgo events, and combining the results from multiple events allowed us to improve the constraints on certain departures from GR predictions³⁵.

In this thesis, we will describe in detail, the first test mentioned above that checks for the consistency of the properties of the remnant estimated from the inspiral and merger–ringdown parts of the observed signal, which we call the *inspiral–merger–ringdown* (IMR) *consistency test*³⁶. This thesis will provide further details of the formulation and implementation of this test that was used to constrain certain departures from GR using the LIGO events GW150914 and GW170104³⁷.

²⁹ Vishveshwara 126, Press 104, Chandrasekhar and Detweiler 51, Berti et al. 38

³⁰ Yunes and Pretorius 137, Mishra et al. 94, Agathos et al. 29

³¹ Clifford M. Will. Bounding the mass of the graviton using gravitational wave observations of inspiralling compact binaries. *Phys. Rev. D*, 57:2061, 1998. DOI: 10.1103/PhysRevD.57.2061

³² Saeed Mirshekari, Nicolás Yunes, and Clifford M Will. Constraining lorentz-violating, modified dispersion relations with gravitational waves. *Physical Review D*, 85(2):024041, 2012; A Samajdar et al. *In Preparation*, 2018; and Anuradha Samajdar and KG Arun. Projected constraints on the dispersion of gravitational waves using advanced ground-and space-based interferometers. *Physical Review D*, 96(10):104027, 2017

³³ All previous detections had been two-detector and did not yield much information about the polarisation of the gravitational waves, since the two LIGO detectors are almost identically oriented.

³⁴ BP Abbott, R Abbott, TD Abbott, F Acernese, K Ackley, C Adams, T Adams, P Addesso, RX Adhikari, VB Adya, et al. Gravitational waves and gamma-rays from a binary neutron star merger: Gw170817 and grb 170817a. *The Astrophysical Journal Letters*, 848(2):L13, 2017

³⁵ Abbott et al. 14, 11, 16

³⁶ Abhirup Ghosh, Archisman Ghosh, Nathan K Johnson-McDaniel, Chandra Kant Mishra, Parameswaran Ajith, Walter Del Pozzo, David A Nichols, Yanbei Chen, Alex B Nielsen, Christopher PL Berry, et al. Testing general relativity using golden black-hole binaries. *Physical Review D*, 94(2):021101, 2016

³⁷ Benjamin P Abbott et al. Gw170104: Observation of a 50-solar-mass binary black hole coalescence at redshift 0.2. *Physical Review Letters*, 118:221101, 2017

Summary

Observation of gravitational waves from CBCs allow us to infer the properties of the source. This has in turn, allowed us to test Einstein's theory of general relativity, for such compact objects, in the highly dynamical strong-field regime of gravity. In the absence of reliable predictions of gravitational waves in alternate theories of gravity, most strong field tests consider GR as a null hypothesis and confirm that observations are consistent with the predictions of GR for a binary black hole merger in a quasi-circular orbit. These tests have indeed been performed on actual observation of gravitational waves by Advanced LIGO-Virgo and show no evidence for deviations from GR.

3 | The Inspiral-Merger-Ringdown Consistency Test

The IMR consistency test was developed based on the original idea by Hughes and Menou¹ proposed in the context of the space-based LISA observatory.² The key idea is to infer the mass and spin of the remnant black hole, using two different parts of the observed signal, and then to compare these independent estimates. We first estimate the initial masses and spins from the inspiral (low-frequency) part of the signal, which allows us to infer the mass and spin of the final black hole making use of fitting formulae calibrated to numerical relativity (NR) simulations of binary black holes. Next, we estimate the same parameters independently from the merger-ringdown (high-frequency) part of the signal and then compare the two estimates. If the signal is correctly described by the merger of a (quasicircular) binary of Kerr black holes in GR, which is implicit in the waveform models that we use to estimate the parameters and the fitting formulae that went in, one should expect the two estimates to be consistent with each other. On the other hand, if there is a departure from GR, depending on the exact nature of the departure, it can manifest as a discrepancy between the two estimates. In particular, if the energy and angular momentum radiated during the merger regime (where the gravity is extremely strong and nonlinear) differ significantly from the GR predictions for these quantities, one could expect a discrepancy between the two estimates in the final mass and spin.

The original idea by Hughes and Menou was to estimate the parameters purely from the early inspiral (well described by the PN approximation to GR) and the late ringdown (well described by a spectrum of QNMs). According to this, we would estimate the parameters of the binary from the early inspiral signal (where any departure from GR is presumably small) and use these estimates to

¹ Scott A. Hughes and Kristen Menou. Golden binaries for LISA: Robust probes of strong-field gravity. *Astrophys. J.*, 623:689, 2005. DOI: 10.1086/428826

² See also, Nakano, Tanaka and Nakamura for a recent study in the context of a ground-based detector.

Hiroyuki Nakano, Takahiro Tanaka, and Takashi Nakamura. Possible golden events for ringdown gravitational waves. *Phys. Rev. D*, 92(6): 064003, 2015. DOI: 10.1103/PhysRevD.92.064003

predict the properties of the remnant black hole, which could be estimated independently from the QNM ringdown. However, such a test will be possible only using a small number of *golden* events, where both the early inspiral and late ringdown are observed with high SNRs. While such a test might be possible in the future using LISA or third generation ground-based instruments, such tests are unlikely to be possible using the current generation of gravitational wave observatories. Meanwhile, Advanced LIGO is expecting to observe several hundred binary black hole events of moderate SNR in the coming years. Hence, tests of GR in the near future are going to progress through building evidence by combining multiple events. Our formulation of the test is geared in this direction. Indeed, the transition from inspiral regime to merger regime does not happen at a precise time or frequency. We use some reasonable choice of a cut-off frequency to separate the signal to the low-frequency (inspiral) and high-frequency (merger–ringdown) parts. As part of our studies, we show that the test is robust against variations of this cutoff frequency that still give large enough SNRs for parameter estimation in both the low- and high-frequency portions independently.

3.1 Method

Using the Bayesian framework described in the previous chapter, we start by computing the joint posterior probability distribution on the initial masses and dimensionless spins $P(m_1, m_2, \mathbf{a}_1, \mathbf{a}_2 | d)^3$ of the binary black hole system (with $m_1 \geq m_2$ by convention). This is done by marginalizing the posterior over the remaining parameters describing the signal. Assuming quasicircular inspirals, fitting formulae calibrated to NR simulations then give us predictions of the mass M_f and dimensionless spin magnitude a_f of the final (remnant) black hole as functions of the initial masses and spins,

$$M_f = M_f(m_1, m_2, \mathbf{a}_1, \mathbf{a}_2), \quad a_f = a_f(m_1, m_2, \mathbf{a}_1, \mathbf{a}_2), \quad (3.1)$$

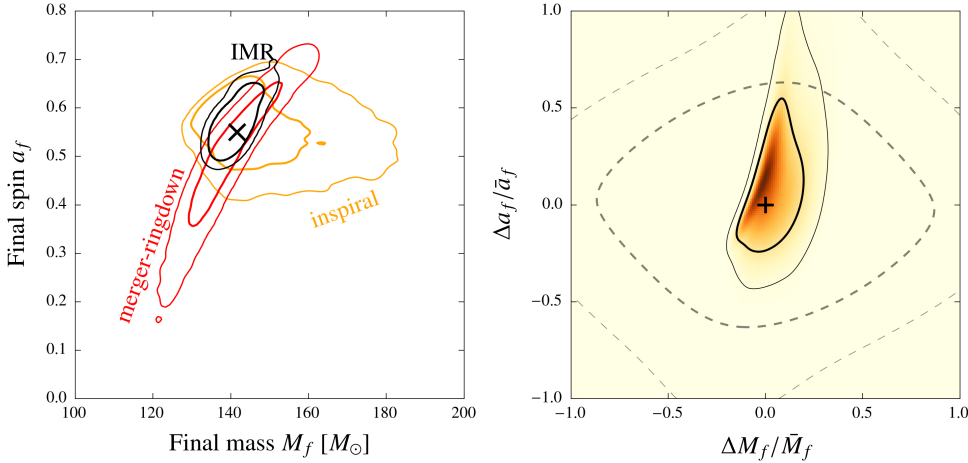
which allow us to obtain the posteriors $P(M_f, a_f | d)$ of the final mass and spin.

First, we estimate the posterior $P_{\text{IMR}}(M_f, a_f | d)$ using the full observed signal. We choose to demarcate the inspiral and post-inspiral parts of the signal using the $m = 2$ mode gravitational wave fre-

³ Here onwards, we drop \mathcal{H}, I from the posteriors to simplifying the notation. Also, unless otherwise noted, the masses we consider are the ones in the detector frame, including the cosmological redshift [89].

quency f_{ISCO} of the innermost stable circular orbit (ISCO) of the remnant Kerr black hole⁴, with mass and spin given by the median values of $P_{\text{IMR}}(M_f, a_f | d)$. We estimate the same parameters from the data containing only the inspiral (low-frequency) part of the observed signal; that is, by setting $f_{\text{cut}} = f_{\text{ISCO}}$ in Eqs. (2.11) and (2.12). This allows us to compute the posterior distribution $P_{\text{I}}(M_f, a_f | d)$ of the mass and spin of the remnant purely from the inspiral part of the signal. Similarly, using only the merger–ringdown (high-frequency) part of the observed signal [by setting $f_{\text{low}} = f_{\text{ISCO}}$ in Eqs. (2.11) and (2.12)], we can get yet another estimate of the posterior $P_{\text{MR}}(M_f, a_f | d)$ of the mass and spin of the remnant. If the observed signal is well described by GR, the two independent estimates $P_{\text{I}}(M_f, a_f | d)$ and $P_{\text{MR}}(M_f, a_f | d)$ have to be consistent with each other as well as with the estimate $P_{\text{IMR}}(M_f, a_f | d)$ using the full data (see, e.g., the left plot in Fig. 3.1).

⁴James M. Bardeen, William H. Press, and Saul A Teukolsky. Rotating black holes: Locally nonrotating frames, energy extraction, and scalar synchrotron radiation. *Astrophys. J.*, 178:347, 1972. DOI: 10.1086/151796



To quantify the consistency of the observed signal with a binary black hole system predicted by GR, we define two parameters that describe the fractional difference between the two estimates of the remnant’s mass and spin

$$\epsilon := \frac{\Delta M_f}{\bar{M}_f}, \quad \sigma := \frac{\Delta a_f}{\bar{a}_f}, \quad (3.2)$$

where

$$\Delta M_f := M_f^{\text{I}} - M_f^{\text{MR}}, \quad \Delta a_f := a_f^{\text{I}} - a_f^{\text{MR}}, \quad (3.3)$$

Figure 3.1: The left panel shows the 68% and 95% credible regions of the posterior distributions $P_{\text{I}}(M_f, a_f)$ and $P_{\text{MR}}(M_f, a_f)$ of the (redshifted) mass and spin of the final black hole estimated from the inspiral and merger–ringdown parts of a simulated GR signal, respectively. Also shown is the posterior $P_{\text{IMR}}(M_f, a_f)$ estimated from the full IMR signal. The simulated GR signal (using SEOBNRv2_ROM_DoubleSpin [106, 117]) is from a binary black hole with $(m_1, m_2) = (60.7, 86.7)M_{\odot}$, and aligned spins $(a_1, a_2) = (0.65, -0.77)$ at a distance of 860 Mpc, observed by the 3-detector Advanced LIGO–Virgo network. The corresponding value of the final mass and spin is indicated by a black cross. The right panel shows the posterior $P(\epsilon, \sigma)$ on the parameters $\epsilon := \Delta M_f / \bar{M}_f$ and $\sigma := \Delta a_f / \bar{a}_f$ that describe the deviation from GR for the same case as the left panel. Dashed lines show the 68% and 95% isoprobability contours of the prior used to compute the posterior, which corresponds to a uniform prior in component masses. The posterior is consistent with the GR value, which is marked by a ‘+’ sign.

and

$$\bar{M}_f := \frac{M_f^I + M_f^{\text{MR}}}{2}, \quad \bar{a}_f := \frac{a_f^I + a_f^{\text{MR}}}{2}. \quad (3.4)$$

In the absence of departures from GR, we expect the posterior $P(\epsilon, \sigma | d)$ of $\{\epsilon, \sigma\}$ to be consistent with zero (within the expected statistical fluctuations due to noise).⁵ Appendix A.1 describes the calculation of $P(\epsilon, \sigma | d)$ from the posteriors $P_I(M_f, a_f | d)$ and $P_{\text{MR}}(M_f, a_f | d)$. An example of the posterior distribution $P(\epsilon, \sigma | d)$ from a simulated GR signal is shown in Fig. 3.1 (right plot).

Finally, if we assume that $\{\epsilon, \sigma\}$ take the same values in multiple events, the posterior from one event could be treated as the prior for computing the posterior for the second event (see Sec. 3.3.3 for a discussion on the validity of this assumption). Such a combined posterior can more sensitively identify certain deviations from GR. In practice, the posteriors $P_j(\epsilon, \sigma | d_j)$ from N such observations can be combined to produce an overall posterior in the following way:

$$P(\epsilon, \sigma | \{d_j\}) = P(\epsilon, \sigma) \prod_{j=1}^N \frac{P_j(\epsilon, \sigma | d_j)}{P_j(\epsilon, \sigma)}, \quad (3.5)$$

where $P(\epsilon, \sigma)$ is the overall prior distribution on ϵ and σ and $P_j(\epsilon, \sigma)$ is the prior distribution used to compute the posterior $P_j(\epsilon, \sigma | d_j)$. Appendix A.2 gives a more complete derivation (along with the necessary caveats) of Eq.3.5.

3.1.1 Choice of priors

Given our poor understanding of the astrophysical distribution of source parameters (such as the component masses and spins), we use uninformative priors for the parameter estimation⁶. Sources are assumed to be uniformly distributed in volume and isotropically oriented. We use uniform priors in component masses $m_{1,2} \in [1, 300]M_\odot$, where $m_1 \geq m_2$, and a uniform prior in the spin magnitudes $|a_{1,2}| \in [0, 0.98]$. We use isotropic priors on the spin orientation when precessing templates are used in the parameter estimation. When nonprecessing templates are used, the priors are set in such a way that the dimensionless spin projection $a_{1,2} \cdot \hat{\mathbf{L}}$ onto the orbital angular momentum \mathbf{L} has a uniform distribution in $[-0.98, 0.98]$. These choices induce a non-uniform prior in $\{\epsilon, \sigma\}$, which is shown by the dashed contours in Fig. 3.1 (right panel).

⁵ We used the full IMR posteriors for M_f and a_f to normalize the fractional parameters in Paper I [72]. We have switched to using the average of the inspiral and merger-ringdown posteriors here so that we only are using posteriors from the two independent measurements, and not mixing in ones from the case where the parameters describing the inspiral and merger-ringdown parts of the waveform are not allowed to vary independently.

⁶ J. Veitch et al. Parameter estimation for compact binaries with ground-based gravitational-wave observations using the LALInference software library. *Phys. Rev. D*, 91(4):042003, February 2015. DOI: 10.1103/PhysRevD.91.042003; and Benjamin P Abbott, R Abbott, TD Abbott, MR Abernathy, F Acernese, K Ackley, C Adams, T Adams, P Addesso, RX Adhikari, et al. Properties of the binary black hole merger gw150914. *Physical review letters*, 116(24):241102, 2016

3.2 Simulations of GR signals in Gaussian noise

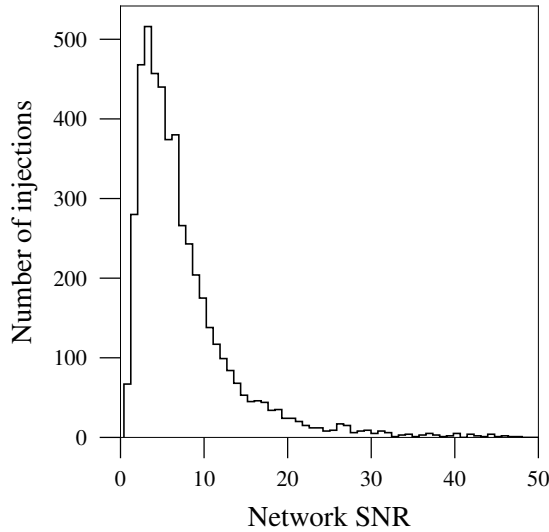


Figure 3.2: Distribution of SNR of Gaussian noise simulations of gravitational wave signals from binary black hole coalescences uniformly distributed in a comoving four-volume between redshifts $[0, 2]$, initial source-frame component masses and component spin magnitudes uniformly distributed between $[10, 80]M_{\odot}$, and $[0, 0.98]$.

First, we estimate the expected constraints that we can place on parameters describing deviations from GR, when the actual signals are well described by GR. We inject simulated gravitational wave signals modelling inspiral, merger and ringdown of binary black holes (based on GR, modelled by the SEOBNRv2_ROM_DOUBLESPIN approximant⁷) into coloured Gaussian noise with the design power spectrum of the Advanced LIGO detectors in the high-power, zero-detuning configuration⁸. Although we perform the analysis assuming the 3-detector Advanced LIGO–Virgo network, for simplicity, we assume that Advanced Virgo has the same noise power spectrum as the Advanced LIGO detectors. All detectors are assumed to have a low frequency cutoff $f_{\text{low}} = 10$ Hz. We simulate a population of binary black holes that is uniformly distributed in comoving four-volume in the redshift interval $z = [0, 2]$, with isotropic orientations (see Section II C of⁹ for more details). Binaries have (source-frame) component masses uniformly distributed in the range $m_{1,2}^s = [10, 80]M_{\odot}$ and component spin magnitudes uniformly distributed in the range $[0, 0.98]$. The gravitational wave signals are redshifted so that the effective masses describing the signal in the detector frame become $m_{1,2} = m_{1,2}^s(1 + z)$. Black hole spins are always assumed to be aligned/antialigned with the orbital angular momentum, as is required by the waveform model used. This is not

⁷Michael Pürrer. Frequency domain reduced order model of aligned-spin effective-one-body waveforms with generic mass-ratios and spins. *Phys. Rev. D*, 93(6):064041, 2016. DOI: 10.1103/PhysRevD.93.064041; and Andrea Taracchini et al. Effective-one-body model for black-hole binaries with generic mass ratios and spins. *Phys. Rev. D*, 89(6):061502(R), 2014. DOI: 10.1103/PhysRevD.89.061502

⁸D. H. Shoemaker. Advanced LIGO anticipated sensitivity curves. Technical Report LIGO-T0900288, 2010. <https://dcc.ligo.org/LIGO-T0900288/public>

⁹Archisman Ghosh, Walter Del Pozzo, and Parameswaran Ajith. Estimating parameters of binary black holes from gravitational-wave observations of their inspiral, merger and ringdown. *Phys. Rev. D*, 94(10):104070, 2016. DOI: 10.1103/PhysRevD.94.104070

an overly restrictive assumption, because the spin components along the orbital angular momentum have the dominant effect on the binary's dynamics and gravitational wave emission¹⁰. Fig. 3.2 shows the distribution of the network SNR of the injected population of binaries. For our analysis, we consider signals with network SNR greater than 8 for both the inspiral and merger–ringdown parts, using the Kerr ISCO frequency to split the signal.¹¹ In addition, we only consider binaries with total redshifted mass less than $150M_{\odot}$, so that the observed signals contain imprints of the inspiral, merger and ringdown. Hence, starting from an initial population of 5000 injections, the final analysis is performed on around 150 events which survive the above thresholds on SNR and total redshifted mass.

On the injections that pass the SNR and mass thresholds, we perform the analysis described in Sec. 3.1, using SEOBNRv2_ROM_DOUBLESPIN as our template for parameter estimation and the final mass and spin fits from Healy *et al.*¹². Parameter estimation using LALInferenceNest is performed using priors that are uniform in component masses in the interval $m_{1,2} \in [1, 300]M_{\odot}$ and component (aligned/antialigned) spins in the interval $[0, 0.98]$. This corresponds to a non-uniform prior in the deviation parameters $\{\epsilon, \sigma\}$ that is centred around the GR value of $\{0, 0\}$. See Fig. 3.1 for an example result. The left panel shows the estimated posterior distributions of the final mass and spin from the inspiral and post-inspiral parts of the data, along with that estimated from the full data. The right panel shows the posterior distribution on the parameters describing deviations from GR, along with the prior used for computing this posterior.

Constraints on the deviations expected from single observations of binary black holes by second-generation ground-based detectors are expected to be modest, due to the large statistical errors from the relatively small SNRs expected for most systems (see, e.g., Fig. 3.2). However, the constraints can be improved by combining the likelihoods of $\{\epsilon, \sigma\}$ from multiple events¹³. Fig. 3.3 shows the combined posteriors $P(\epsilon, \sigma)$ as a function of the number of simulated events. The constraints on the deviation parameters $\{\epsilon, \sigma\}$ become narrower when multiple events are combined. These constraints are within the reach of Advanced LIGO–Virgo observations in the next few years¹⁴.

From the posterior distribution $P(\epsilon, \sigma)$, one can obtain the credible level corresponding to the GR value of the deviation parameters,

¹⁰ Patricia Schmidt, Mark Hannam, and Sascha Husa. Towards models of gravitational waveforms from generic binaries: A simple approximate mapping between precessing and non-precessing inspiral signals. *Phys. Rev. D*, 86: 104063, 2012. DOI: 10.1103/PhysRevD.86.104063

¹¹ Here, for simplicity, we use the Kerr ISCO frequency computed from the injected values of masses and spins to split the signal. In an actual observation, we use the median estimate of the Kerr ISCO frequency estimated from the observed IMR signal.

¹² James Healy, Carlos O. Lousto, and Yosef Zlochower. Remnant mass, spin, and recoil from spin aligned black-hole binaries. *Phys. Rev. D*, 90(10): 104004, 2014. DOI: 10.1103/PhysRevD.90.104004

¹³ We expect the combined errors to go down roughly as $N^{-1/2}$, where N is the number of events while the individual errors to go down as ρ^{-1} , where ρ is the SNR of the event. Thus, combined constraints from N events with roughly same SNR should be comparable to the constraints from a single event with an SNR of $\rho N^{1/2}$.

¹⁴ Abbott et al. 11, 7

i.e., $\{\epsilon, \sigma\} = \{0, 0\}$. The credible level for a certain set of parameters $\{\epsilon_0, \sigma_0\}$ is the total probability enclosed within an isoproability contour passing through $\{\epsilon_0, \sigma_0\}$:

$$\text{credible level} = \int_{\{\epsilon, \sigma\} \text{ where } P(\epsilon, \sigma) > P(\epsilon_0, \sigma_0)} P(\epsilon, \sigma) d\epsilon d\sigma. \quad (3.6)$$

See, e.g., Eq. (42) in ¹⁵ for a general definition. The area enclosed within the isoproability contour is the credible area (or credible interval in 1 dimension). A lower credible level for the GR parameters indicates a greater agreement with GR. However, this GR credible level is not expected to be zero even when the data is correctly described by GR, because the peak of posterior on the deviation parameters $\{\epsilon, \sigma\}$ is randomly shifted away from $\{0, 0\}$ in the presence of noise.

If the parameter values $\{\epsilon, \sigma\}$ were sampled from the prior distribution used to compute their posterior, we would expect the p credible interval of the posterior to include the true value approximately p of the time, for the case of an appropriately chosen prior ¹⁶. However, for the GR injections that we performed, we do not expect the true value of $\{\epsilon = 0, \sigma = 0\}$ to be found at credible level p for a fraction p of events. This is because of our prior distribution for $\{\epsilon, \sigma\}$ does not match the intrinsic distribution (which would be a delta function): we are allowing for the possibility of mismatches between inspiral and merger–ringdown even though this is not the case for the injected GR signals. To demonstrate this for our set of GR injections, in Fig. 3.4 we show the fraction of events for which the (true) GR point is found within the p credible region. From Fig. 3.4, we see the true GR value is often near the peak of the distribution, meaning that it is found within the p credible region for more than a fraction p of events.¹⁷ In order to make a frequentist statement about the significance of the measurement of non-zero ϵ or σ (how common such a deviation is if GR were correct), a similar study would need to be done for the region of mass and spin space of interest in order to calibrate expectations.

¹⁵J. Veitch et al. Parameter estimation for compact binaries with ground-based gravitational-wave observations using the LALInference software library. *Phys. Rev. D*, 91(4):042003, February 2015. DOI: 10.1103/PhysRevD.91.042003

¹⁶Gauri Sankar Datta and Trevor J Sweeting. Probability matching priors. *Handbook of statistics*, 25:91–114, 2005; and Samantha R. Cook, Andrew Gelman, and Donald B. Rubin. Validation of software for bayesian models using posterior quantiles. *J. Comp. Graph. Stat.*, 15(3):675–692, 2006. DOI: 10.1198/106186006X136976

¹⁷For the marginalised ϵ distribution, we see that the true GR value is approximately found within the p credible interval a fraction p of the time. In this case, the scatter due to noise is sufficient to balance the mismatch in the prior used.

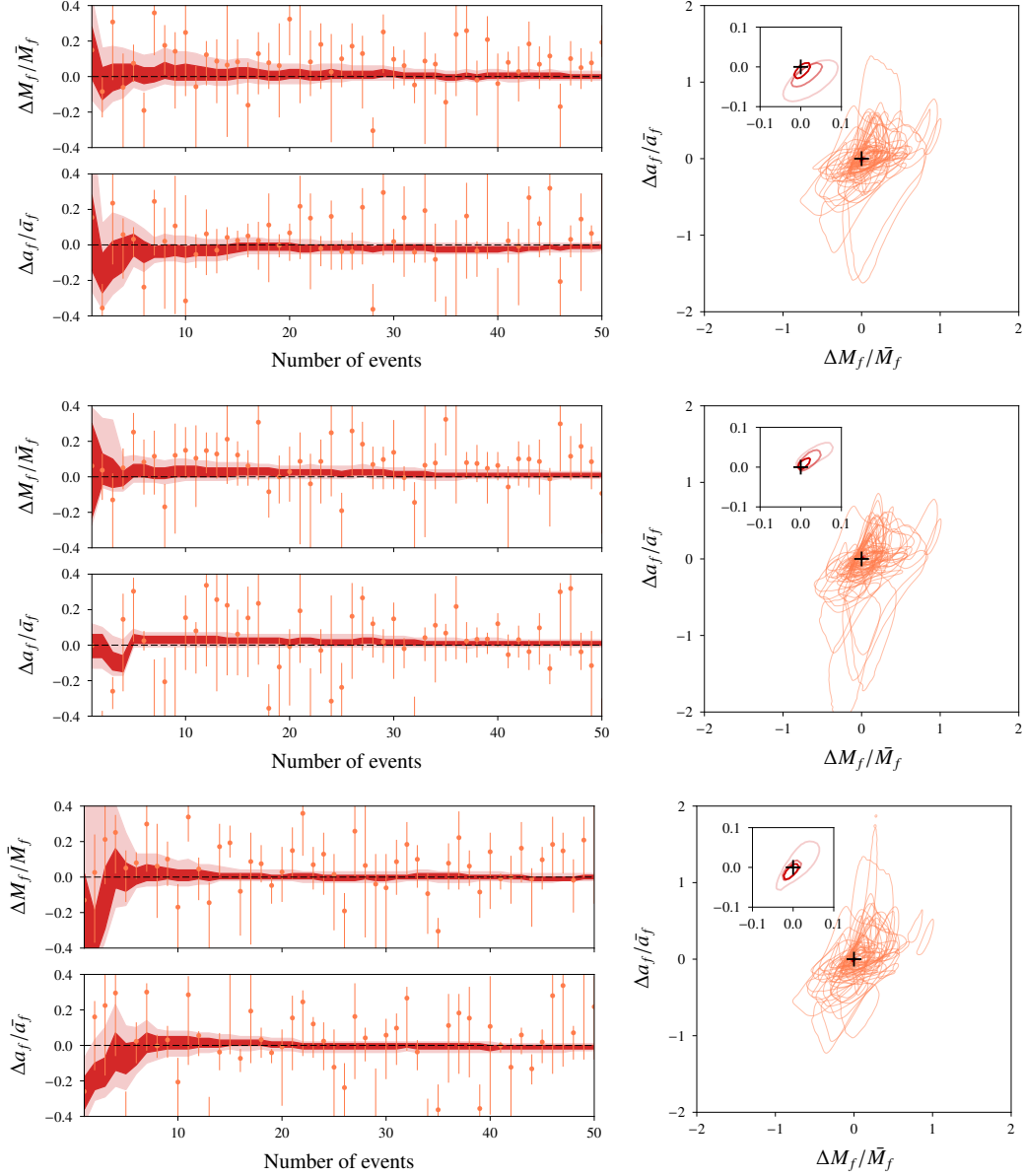


Figure 3.3: *Left*: In each plot shaded regions show the 68% and 95% credible intervals on the combined posteriors on $\epsilon := \Delta M_f / \bar{M}_f$, $\sigma := \Delta a_f / \bar{a}_f$ from multiple observations of GR signals, plotted against the number of binary black hole observations. The GR value ($\epsilon = \sigma = 0$) is indicated by horizontal dashed lines. The mean value of the posterior from each event is shown as an orange dot along with the corresponding 68% credible interval as an orange vertical line. Posteriors on ϵ are marginalized over σ , and vice versa. *Right*: The thin orange contours show the 68% credible regions of the individual posteriors on the ϵ, σ computed from the same events. The GR value ($\epsilon = \sigma = 0$) is indicated by the black + sign. *Right inset*: The red contours show the 68% credible regions on the combined posterior from 5, 10 and 25 events (with increasing shades of darkness). The GR value ($\epsilon = \sigma = 0$) is indicated by the black + sign. Different rows correspond to different catalogs of 50 randomly chosen events from a total of ~ 100 simulated events.

3.3 Simulations of modified GR signals in Gaussian noise

3.3.1 Generation of modified GR waveforms

We also test the sensitivity of our pipeline towards certain kinds of deviations from GR, using signals that differ slightly from the predictions of GR. Specifically, we generate kludge modified GR waveforms that are qualitatively similar to binary black hole waveforms in GR, but differ in their energy and angular momentum loss as a function of frequency. These waveforms are similar enough to GR binary black hole waveforms that they would likely be detected with a standard detection pipeline, as we discuss below. However, we demon-

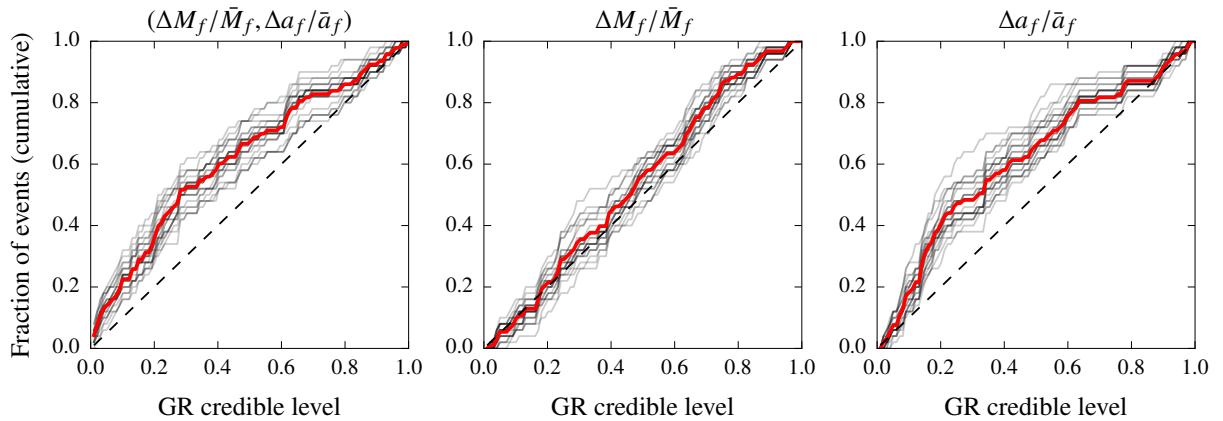


Figure 3.4: A p vs p plot for the deviation parameters ($\epsilon := \Delta M_f / \bar{M}_f$, $\sigma := \Delta a_f / \bar{a}_f$) computed from the set of GR injections described in section 3.2. In each plot, the horizontal axis indicates a credible level, and the vertical axis indicates the fraction of events with the deviation parameters below the given credible level. In each plot, the gray lines are computed for 50 different subsets of the full population of ~ 100 events, and the red line correspond to the same computed using all the ~ 100 events. The left plot corresponds to credible intervals computed from the 2-dimensional posteriors $P(\epsilon, \sigma | d)$, while the middle and right plots correspond to marginalized posteriors on ϵ and σ , respectively. The diagonal lines indicate the case where the Bayesian credible levels match the frequentist confidence levels.

strate that the consistency test described in this chapter is able to identify such deviations from GR by combining the posteriors from multiple observations.

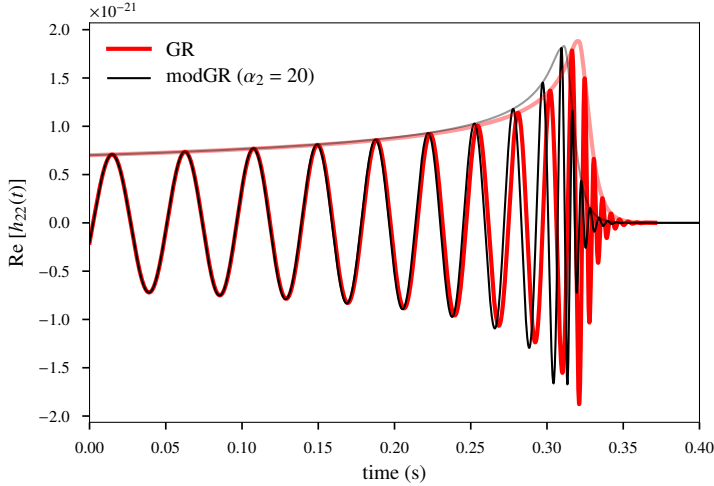
We start from the nonspinning effective one-body (EOB) waveform model given in ¹, which is available as Matlab code at IHES ², and modify the gravitational wave flux to yield our kludge modified GR waveform. Specifically, we multiply all the modes of the waveform that first enter the flux at second PN order [i.e. $O(v^4/c^4)$, where v is the binary’s orbital velocity], viz the $(\ell, m) = (3, \pm 2)$, $(4, \pm 4)$, and $(4, \pm 2)$ modes, by a constant factor $\sqrt{\alpha_2}$, so that their contributions to the flux are multiplied by α_2 . This also modifies the flux at 3PN and all higher PN orders. We start with the modes that first enter at 2PN rather than the ones that first enter at 1PN since the latter modes vanish for equal-mass nonspinning binaries, and we still want a nonvanishing modification in this limit.

We retain the termination condition for the inspiral–plunge phase of the waveform used the original code. This uses the maximum of the orbital frequency (calculated from the EOB Hamiltonian) to mark the termination of the calculation of the inspiral–plunge waveform (by evolving the EOB Hamilton equations) and the start of the matching to the QNMs used to model the merger and ringdown. This termination condition coincides with crossing the light ring in the extreme mass-ratio limit. We also keep the next-to-quasicircular parameters set to the values determined from NR simulations that are already given in the code. Additionally, we keep all the other parameters set to their default values, except for a parameter that keeps

¹ Thibault Damour, Alessandro Nagar, and Sebastiano Bernuzzi. Improved effective-one-body description of coalescing nonspinning black-hole binaries and its numerical-relativity completion. *Phys. Rev. D*, 87(8):084035, 2013. DOI: 10.1103/PhysRevD.87.084035

² <http://eob.ihes.fr>; we used the “1202” version of the code

one from probing unphysical regions of the EOB potential while the EOB equations are solved numerically. This was necessary to change in order to compute waveforms for higher mass ratios, even without other modifications to the code.



With these choices, we find that the waveforms look similar to a GR waveform up to the values of $\alpha_2 = 20$ we consider here. This is illustrated in Fig. 3.5 for an equal-mass binary; the unequal-mass waveforms we consider in the next subsection also look similar to GR waveforms. Additionally, we have checked that this modification to the waveform does not induce any excess eccentricity: The eccentricity of the modified waveforms is small, and the same size as the eccentricities of the unmodified waveforms ($\lesssim 10^{-5}$ for the initial frequencies we are considering).³

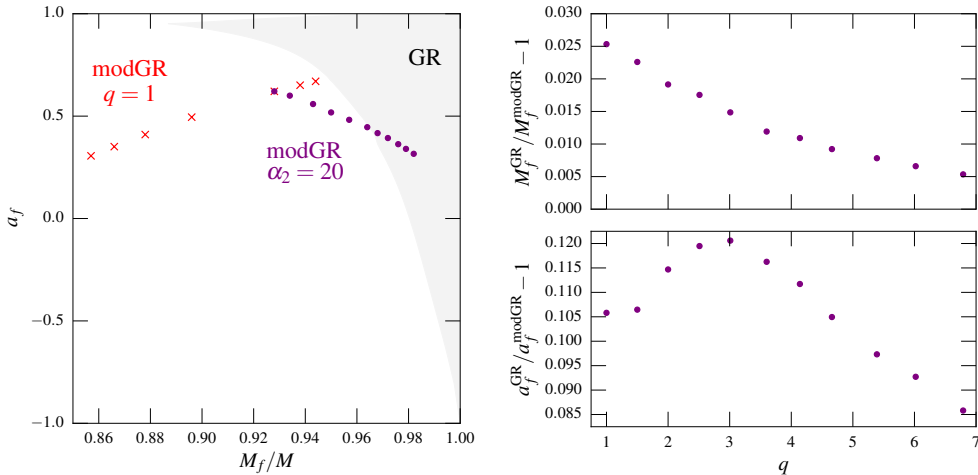


Figure 3.5: The real part (darker lines) and amplitude (lighter lines) of the (2,2) mode gravitational waveform form an equal-mass nonspinning binary black hole computed using the IHES EOB code with no modification (GR) and with our modification to the flux with $\alpha_2 = 20$ (modGR). For this illustration, we have taken the total mass to be $100M_\odot$, the distance to be 1 Gpc, and have aligned the waveforms at $t = 0$, which we have taken to correspond to a (2,2) mode frequency of 20 Hz.

³We estimate the eccentricity of the waveforms as in section IV C of [65] [Eq. (4.13) and following], though with two additional higher-order PN terms added to the fitting function, since the eccentricity is small. The results did not change upon adding a third additional PN term. Since this estimate only uses the leading-order gravitational wave effects, it does not need to be modified to account for the modification to the flux, which only starts at 2PN.

Figure 3.6: *Left*: The final mass and spin allowed by GR (shaded region), as calculated from the fits from [77], as well as the values for the kludge waveforms with a mass ratio of $q = 1$ and $\alpha_2 \in \{5, 10, 20, 100, 200, 300, 400\}$ (crosses, with α_2 increasing from right to left), as well as $\alpha_2 = 20$ and q from 1 to 6.8 in roughly steps of 0.5 (circles, with q increasing from left to right). The $\alpha_2 = 20$ points are taken from the injection set. *Right*: The fractional differences between the final mass and spin for the kludge waveforms with $\alpha_2 = 20$, as a function of the mass ratio q .

Since the final mass and spin in the original EOB waveform are set by a fit to NR results, we replace this determination by demanding self-consistency of the radiated energy and angular momentum. That is, we choose the final mass and spin by minimizing the difference between the final mass and spin used to obtain the merger-ringdown part of the model and the final mass and spin obtained from energy and angular momentum balance using the initial energy and angular momentum and the radiated energy and angular momentum (calculated from the waveform). Here we are able to obtain fractional disagreements of less than $\sim 10^{-4}$ between the final mass and spin calculated from the radiated energy and angular momentum and those used to compute the merger-ringdown part of the signal. These fractional disagreements are considerably better than the agreement of these quantities for the original IHES EOB waveform for some mass ratios, and much smaller than the differences in radiated energy and angular momentum between the different waveforms we consider. We compute the energy and angular momentum loss using multipoles up to $\ell = 7$, since we are only able to fit for the ringdown up to $\ell = 7$, the highest ℓ for which the tabulated QNM results used in the code are available⁴. We take the standard GR expressions for the radiated energy and angular momentum to still be valid for this modified gravity waveform; these expressions indeed remain valid for a significant number of modified theories⁵. We find that the final mass and spin falls outside the region allowed in GR in many cases, though there is a region of overlap for $\alpha_2 = 20$ and mass ratio $q := m_1/m_2 \gtrsim 4$; see Fig. 3.6. We also plot the fractional difference in the final mass and spin between GR and the kludge waveforms with $\alpha_2 = 20$ in this figure, and see that the fractional difference in the final spin is significantly larger than the fractional difference in the final mass.

In addition to enhanced energy and angular momentum fluxes, these kludge modified GR waveforms have an enhanced linear momentum flux. This leads to larger gravitational wave recoils than one obtains for nonspinning systems in GR, where the maximum is only $\sim 180 \text{ km s}^{-1}$ (see, e.g.,⁶). For the $\alpha_2 = 20$ deviation we consider here, the maximum recoil is $\sim 440 \text{ km s}^{-1}$.⁷ We do not include any potential effects (e.g., the Doppler shifts discussed in⁸) from these enhanced recoils, which are still small (at most $\sim 10^{-3}$ times the

⁴Emanuele Berti, Vitor Cardoso, and Andrei O. Starinets. Quasinormal modes of black holes and black branes. *Class. Quantum Grav.*, 26:163001, 2009. DOI: 10.1088/0264-9381/26/16/163001; and <http://www.phy.olemiss.edu/~berti/qnms.html>

⁵Leo C. Stein and Nicolas Yunes. Effective Gravitational Wave Stress-energy Tensor in Alternative Theories of Gravity. *Phys. Rev. D*, 83:064038, 2011. DOI: 10.1103/PhysRevD.83.064038

⁶Healy and Lousto⁷⁶

⁷The original IHES EOB waveform model (without deviations) already has a maximum recoil of $\sim 350 \text{ km s}^{-1}$.

⁸Gerosa and Moore⁷¹

speed of light).⁹

We have not changed the QNM spectrum of the final black hole in these kludge modified gravity waveforms for simplicity. However, one expects the QNM spectrum to be modified in any alternative theory that predicts a different gravitational wave energy loss for a binary black hole, even those for which the unperturbed Kerr metric is a solution of the field equations, since the behavior of perturbations of Kerr will generically be different in an alternative theory (see, e.g.,¹⁰). Extending this analysis to the case where one modifies the QNM spectrum would be a useful additional check of the consistency test presented here, though the requisite catalogs of QNMs are not yet available, even for the case of a Kerr–Newman black hole, which could be used as a stand-in for a modified gravity black hole: See, however, Dias *et al.*¹¹ for some recent results that could be used to obtain such a QNM catalogue.

⁹ Enhanced recoils were not an issue for the larger deviation considered in Paper I because the recoil vanishes, by symmetry, for the equal-mass nonspinning system considered there.

¹⁰ Barausse and Sotiriou 36

¹¹ Oscar J. C. Dias, Mahdi Godazgar, and Jorge E. Santos. Linear Mode Stability of the Kerr–Newman Black Hole and Its Quasinormal Modes. *Phys. Rev. Lett.*, 114(15):151101, 2015. DOI: 10.1103/PhysRevLett.114.151101

$m_1 (M_\odot)$	$m_2 (M_\odot)$	D_L (Mpc)	Optimal SNR	PyCBC SNR	Reduced χ^2	Re-weighted SNR
139.1	69.5	5625.8	8.1	8.6	0.76	8.6
88.1	14.7	803.5	14.3	14.0	0.78	14.0
40.8	46.8	787.0	21.6	21.7	0.81	21.7

We only inject the $(2, \pm 2)$ modes of the waveform here, since these are the only modes included in the waveform model we use for the test, as well as for the injections in Sec. 3.2. The modifications to the higher modes appear in the $(2, \pm 2)$ modes by their effect on the waveform’s phasing, since the higher modes are used to compute the modified energy flux. We have run the test on two GR injections with higher modes in Sec. 3.4.4, and found that the inclusion of higher modes does not bias the test in those cases.

Finally, almost all of our modified GR signals will be confidently detected by the standard matched-filter based searches for binary black holes, which include the chi-squared discriminatory test¹². To

Table 3.1: The table shows the parameters of some of the injected modified GR signals (D_L is the luminosity distance) and how well the PyCBC pipeline is able to detect these injected signals in a single detector search (LIGO Livingston). Optimal SNR is the optimal SNR available in the injection, PyCBC SNR is the matched filter SNR extracted by the PyCBC pipeline, and re-weighted SNR is the chi-squared weighted SNR defined in equation (6) of [122]. The optimal SNR is computed using the detector’s noise power spectrum (it is defined by $\langle h|h \rangle^{1/2}$, for a signal h), while the matched filter SNR is a statistical variable computed using a specific noise realization, which is why the PyCBC SNR can be larger than the optimal SNR.

¹² Bruce Allen. A chi**2 time-frequency discriminator for gravitational wave detection. *Phys. Rev. D*, 71:062001, 2005. DOI: 10.1103/PhysRevD.71.062001

demonstrate this, we have run the PyCBC¹³ matched filter based detection pipeline on these injections (using a single GR template from the SEOBNRv2_ROM_DOUBLESPIN family, corresponding to the parameters of the simulated modGR signal). We see that the chi-squared weighted SNR recovered by the detection pipeline is close to the optimal SNR of the signal (see table 3.1 and Fig. 3.7 for some examples). The SNR maximized over the full template bank is expected to be even larger than this, practically ensuring confident detections.

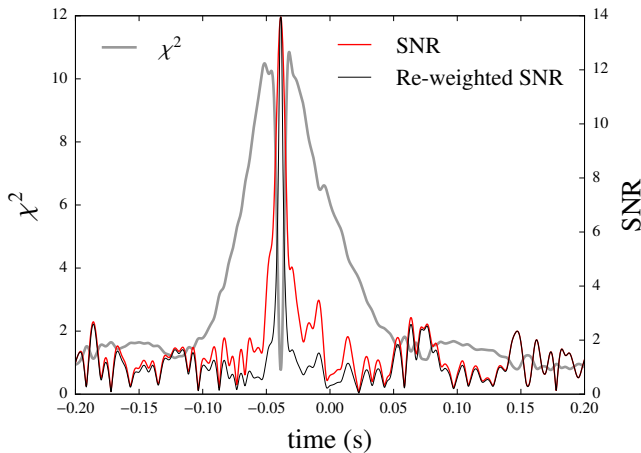


Figure 3.7: Time series of the matched filter SNR, the reduced χ^2 and re-weighted SNR from an injected modified GR waveform, corresponding to the second entry in table 3.1. The re-weighted SNR is the PyCBC detection statistic and is defined in equation (3) of [122]. The injected signal is located in the data at around time -0.05 s in the plot. This is very similar to the analogous plot for GW150914 given in figure 8 of [6], indicating that this modified GR signal would be found by the PyCBC search in a similar way to a genuine GR signal.

3.3.2 Results from the simulations of modified GR signals

Here we demonstrate that the IMR consistency test is able to identify (at least certain types of) deviations from GR by performing our analysis on a population of simulated signals using the modified GR waveforms described above. In Paper I, we have demonstrated the ability of this test to identify a relatively large modification to the binary's energy flux ($\alpha_2 = 400$). Such a deviation from GR was easily detectable with high confidence from a single observation of moderate SNR. Here we consider the ability of the test to discern much smaller deviations from GR by combining results from multiple observations. Specifically, we consider the same population of binary parameters considered to simulate the GR case in Sec. 3.2 except that the waveforms are generated with a modification of the GR energy flux as described in Sec. 3.3.1. Also, for simplicity, we consider binary black holes with zero spins, since the EOB waveform family that we employ to produce modified GR waveforms is a nonspin-

¹³Samantha A. Usman et al. The PyCBC search for gravitational waves from compact binary coalescence. *Class. Quantum Grav.*, 33(21):215004, 2016. DOI: 10.1088/0264-9381/33/21/215004

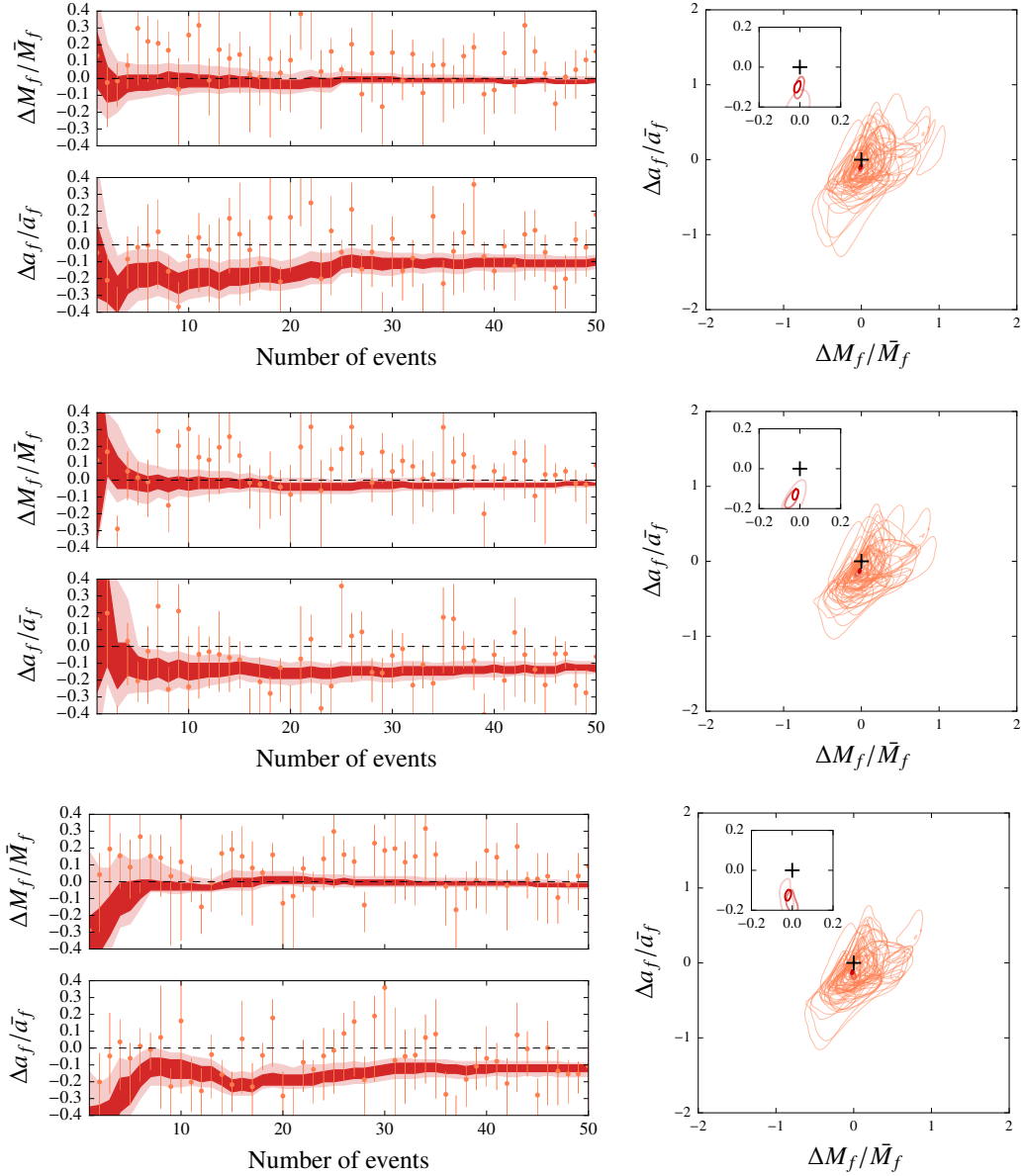


Figure 3.8: Same as figure 3.3 except that the test is performed on simulated signals containing a modification from GR described in section 3.3.2. The combined posteriors from multiple observations show a clear departure from the GR predictions (horizontal dashed lines on the left plots and the plus sign on the right plots).

ning model¹⁴. However, we still perform parameter estimation using the same SEOBNRv2_ROM_DOUBLESPIN aligned-spin model employed in Sec. 3.2.

Modified GR waveforms for binaries with different mass ratios (as well as distances, sky locations, and other extrinsic parameters) were constructed using the prescription presented in Sec. 3.3.1, with deviation parameter $a_2 = 20$. An example of a modified GR waveform (along with the corresponding GR waveform from the same binary) is shown in Fig. 3.5. Although such a modified GR waveforms appears similar to a GR waveform, we show below that the IMR consistency test is able to identify deviations from GR by combining multi-

¹⁴Thibault Damour, Alessandro Nagar, and Sebastiano Bernuzzi. Improved effective-one-body description of coalescing nonspinning black-hole binaries and its numerical-relativity completion. *Phys. Rev. D*, 87(8): 084035, 2013. DOI: 10.1103/PhysRevD.87.084035; and <http://eob.ihes.fr>; we used the “1202” version of the code

ple events. Fig. 3.8 shows the joint posteriors on the parameters that describe deviations from GR. It can be seen that, although individual posteriors are unable to identify deviations from GR, the combined posteriors show a clear departure from the GR predictions, even for the relatively small deviation that we consider.¹⁵ We also see that the combined posterior on $\sigma := \Delta a_f / \bar{a}_f$ differs significantly more from 0 than does the combined posterior on $\epsilon := \Delta M_f / \bar{M}_f$. This might be expected, due to the larger fractional differences from GR in the final spin seen in Fig. 3.6.

3.3.3 Caveats

The way that we combine the posteriors from multiple events implicitly assumes that $\{\epsilon, \sigma\}$ take the same values in multiple events. This is certainly true if the true theory is GR, when they are always zero, but is not necessarily true for all modified theories of gravity. If the $\{\epsilon, \sigma\}$ values induced by the true theory are strongly dependent on the intrinsic parameters of the black holes (such as their masses and spins), then the combined posteriors from multiple events *may* not converge to a non-zero value. Hence, this test (like any other test of GR) is not sensitive to *all* kinds of possible deviations from GR. However, if the deviation is only weakly dependent on the intrinsic parameters, it is a reasonable assumption that the values of $\{\epsilon, \sigma\}$ observed by LIGO-Virgo will be clustered in a small range, due to the rather narrow range of masses ($\sim 10\text{--}80M_\odot$) of black hole binaries employed in this test (and hence the reasonably narrow range of length scales probed by these black holes).¹⁶ This is the case for simulations presented in Sec. 3.3. Here the modification from GR has a dependence on the intrinsic parameters (see, e.g., Fig. 3.6); still, $\{\epsilon, \sigma\}$ estimates from individual posteriors tend to cluster around a reasonably small range of values, and the combined posteriors converge to a non-zero value in Fig. 3.8. On the other hand, if the deviation is a strong function of the intrinsic parameters, then combining the posteriors of the entire population may not be the most sensitive method of detecting the deviation. One possibility to address this would be to combine the posteriors of subsets of detections with similar inferred parameters. Such combined posteriors from different regions of the parameter space (e.g., low-mass or high-mass) will

¹⁵ Taking $\alpha_2 = 20$ corresponds to multiplying the 2PN term in the frequency domain phase expression by a factor of ~ 0.4 for equal masses, with the factor decreasing monotonically to ~ -4.5 for a mass ratio of 7 (the largest mass ratio in the detected population).

¹⁶ One might also worry about the spin-dependence of possible deviations. However, if the size of the deviation is controlled by the maximum curvature outside the horizons of the black holes, the spin only changes the length scale given by the curvature at the horizon of a Kerr black hole by a factor of $2\sqrt{2} \simeq 2.8$; see, e.g., Eq. (5.47) of [100] for the expression for the Kretschmann scalar in Kerr, whose inverse fourth root gives the length scale we are considering. This neglects possible propagation effects, though even in that case LIGO is not expected to detect binaries with orders of magnitude different distances.

provide us some indication of the nature of the deviation as a function of some scales (e.g., curvature). We leave such studies as future work.

Note that, in Fig. 3.8, the fractional difference in the final spin has the opposite sign to what might naïvely be expected, given that the modGR waveforms correspond to smaller final spins than their GR counterparts. Since most of the angular momentum loss comes during the merger and ringdown, it seems reasonable that the inspiral values for the final mass and spin would be close to their GR values for the system’s mass ratio, while those inferred from the ringdown would correspond to the true values used to construct the waveform. However, such an interpretation is possible only when the parameters are estimated from only the *early* inspiral and *late* ringdown parts of the waveform. Such a test would require both the early inspiral and late ringdown to be observed with high SNR. While such tests might be possible in the future, currently we are limited by the moderate SNRs of the observed signals, and hence are forced to include the late inspiral and merger parts in our analysis. For the case of the modGR waveforms that we use, the estimated parameters from the inspiral part are biased (typically to more massive, asymmetric binaries) which correspond to a smaller value of the final spin, as compared to the same estimated from the post-inspiral part, producing the observed sign in the fractional difference in the final spin.

3.4 Robustness of the consistency test

We also test the robustness of the IMR consistency test to the choice of various parameters used in the analysis, for example, the cutoff frequency used to demarcate the division between the low-frequency (inspiral) and high-frequency (merger–ringdown) parts of the waveform, the choice of the particular approximant waveform, and the fitting formula for the mass and spin of the final black hole, etc. For this we use a simulated GR signal with waveform approximant SEOBNRV2_ROM_DOUBLESPIN (except in Sec. 3.4.3 where we use approximant IMRPHENOMPv2¹⁷ and in Sec. 3.4.4 where we use NR waveforms). We also study the effect of neglecting higher modes and spin precession on the IMR consistency test. These are performed by injecting NR waveforms from the publicly available Simulating eX-

¹⁷ Hannam et al. 75, Khan et al. 88, Bohé et al. 44

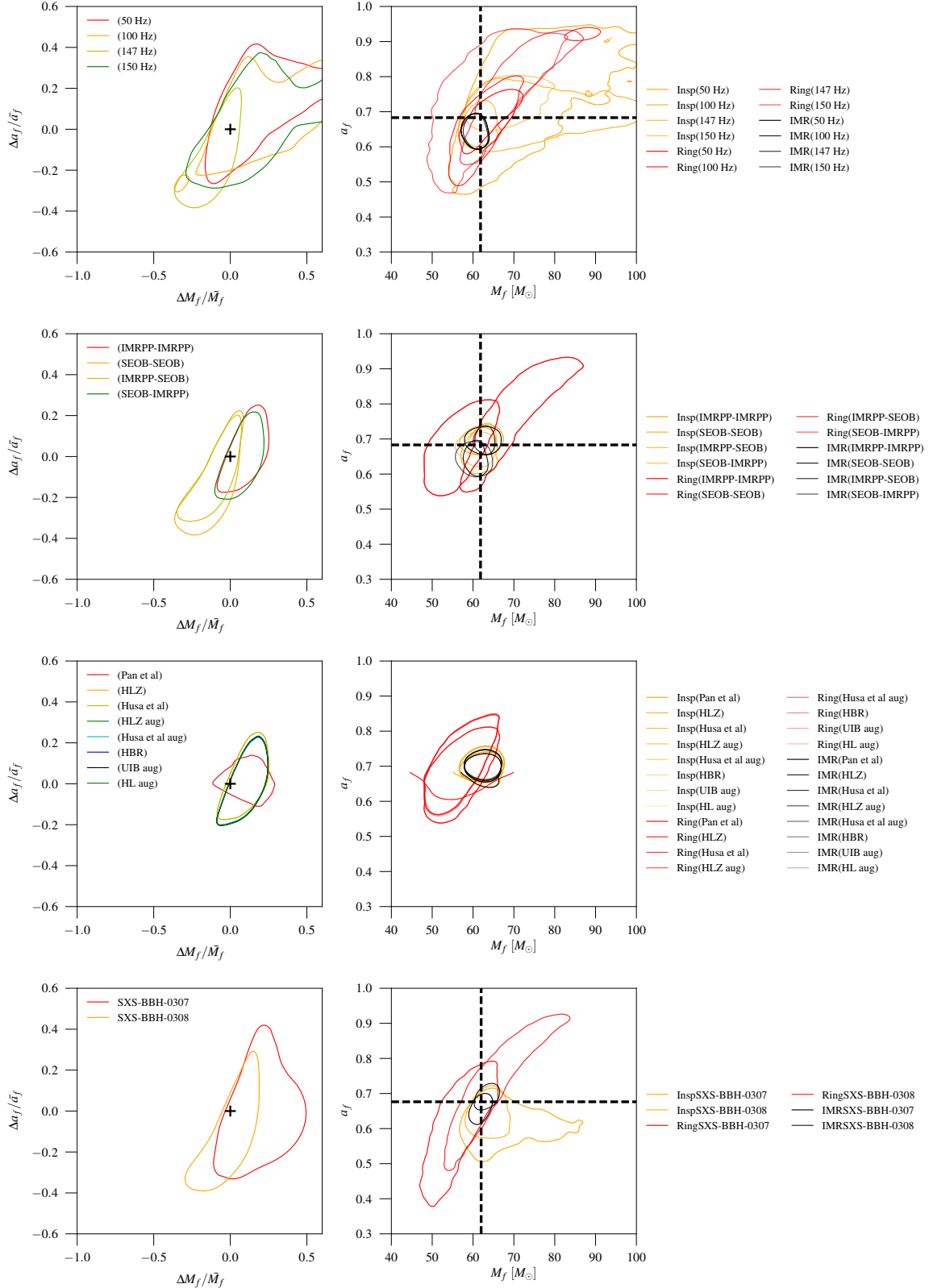


Figure 3.9: Robustness studies against the choice of cutoff frequency (top row), approximants (second row), fitting formulae (third row) and effects of higher modes and precession (bottom row). Left panels show the 68% credible region of the posterior distributions $P(\epsilon, \sigma)$. The GR value is marked by a + sign. Right panels show the 68% credible region of the posterior distributions $P_i(M_f, a_f)$, $P_{MR}(M_f, a_f)$ and $P_{IMR}(M_f, a_f)$ of the mass and spin of the final black hole estimated from the inspiral, merger-ringdown parts and the full IMR signal for each simulated case, respectively. In the second panel, the parentheses in the legend carry a combination of labels; the first label refers to the waveform family used to perform the injection and recovery of the inspiral portion, while the second label refers to the same for the merger-ringdown portion. In the third panel, the contours for the five fits that include the contributions from in-plane spins to the final spin (HLZ aug [77], Husa *et al.* aug [84], HBR [80], UIB aug [86] and HL aug [76]; "aug" denotes augmentation following [87]) lie almost on top of each other, thus making the individual contours indistinguishable. The same is true for the contours for the purely aligned-spin fits (HLZ [77] and Husa *et al.* [84]). The nonspinning Pan *et al.* [98] fit has a distinct contour.

treme Spacetimes (SXS) catalog¹⁸. All these studies are performed assuming a binary black hole signal with parameters close to that of the first LIGO event GW150914 — masses $m_1 = 36M_\odot$, $m_2 = 29M_\odot$ and aligned spins, $a_{1,z} = -0.32$, $a_{2,z} = 0.58$, with optimum sky position and orientation, producing an optimal SNR of 25 in the Advanced LIGO Hanford–Livingston and Advanced Virgo network. These studies demonstrate the robustness of the IMR consistency test only for the case of signals with parameters similar to that of GW150914, that is, with moderate mass ratios. If we observe signals with large mass ratios and large, misaligned spins in the future, the robustness of the IMR consistency test will need to be reinvestigated. Also, these robustness studies have been restricted to the case of single events: when a large number of events are combined to produce precise constraints on the deviations from GR, we will have to worry about even small systematic errors affecting our analysis. Such studies have to be performed in the near future, in anticipation of the large number of binary black hole signals that Advanced LIGO is expected to observe.

¹⁸ URL <http://www.black-holes.org/waveforms/>. SXS Gravitational Waveform Database

3.4.1 Cutoff frequency between the inspiral and merger–ringdown

There is no well defined transition frequency (or time) between the inspiral and post-inspiral (merger–ringdown) parts of the waveform¹⁹. We have chosen the ISCO frequency of the final Kerr black hole with mass and spin inferred from the full IMR waveform at this cutoff frequency. Increasing this cutoff frequency will increase (decrease) the SNR of the inspiral (post-inspiral) part and hence will improve (worsen) the parameter estimation from the inspiral (post-inspiral) analysis, thus affecting our statistical errors. There thus is likely an optimal choice for the cutoff frequency as far as the test’s sensitivity to a given deviation from GR is concerned. However, if our analysis is free from major systematic errors, the two independent estimates always have to be consistent with each other when it is applied to a binary black hole coalescence in GR. Here we illustrate that our analysis produces consistent results for reasonable choices of the cutoff frequency.

The ISCO frequency of a Kerr black hole with mass $M_f = 62M_\odot$ and dimensionless spin $a_f = 0.68$ (remnant of the merger of two

¹⁹ Alessandra Buonanno, Gregory B. Cook, and Frans Pretorius. Inspiral, merger and ring-down of equal-mass black-hole binaries. *Phys. Rev. D*, 75:124018, 2007. DOI: 10.1103/PhysRevD.75.124018

black holes with masses $m_1 = 36M_\odot$, $m_2 = 29M_\odot$ and aligned spins, $a_{1,z} = -0.32$, $a_{2,z} = 0.58$) is 146.4 Hz. We repeat the analysis with 4 different choices of the cutoff frequency in the interval 50–150 Hz. The results are shown in Fig. 3.4 (top panels). It can be seen that, while the spread of the posteriors (that is, the statistical errors) depends on the choice of the cutoff frequency, the inspiral and post-inspiral estimates are always consistent with each other. Also, the posteriors on the parameters describing deviations from GR are always consistent with zero, indicating the robustness of the test against the specific choice of the cutoff frequency.

3.4.2 *Waveform approximant*

The Bayesian inference described in Sec. 3.1 is performed by employing semi-analytical gravitational waveforms (computed by a combination of analytical and numerical relativity) as the GR model. The inherent assumption is that these are faithful representations of the actual signals produced by nature. However, depending on the particular methods used to construct these waveforms, there can be minor differences between different gravitational waveform families (approximants). Here, we demonstrate the robustness of the IMR consistency test employing two IMR waveform families, namely, the non-precessing spin reduced-order EOB model SEOB-NRV2_ROM_DOUBLESPIN²⁰ and the precessing single effective-spin phenomenological model IMRPHENOMPv2²¹. The systematic errors of these models in the vicinity of GW150914 and their effects on parameter estimation were studied in²².

Fig. 3.4 (second row) shows the results from simulated GR signals from a binary black hole with parameters described in the previous section. Apart from performing the analysis where the same waveform family is employed in estimating the parameters from the inspiral and post-inspiral parts, the figure also demonstrates the robustness of the consistency test when we employ one waveform family for estimating the parameters from the inspiral part and another to estimate the same from the post-inspiral part. In each case, the waveform family used to create a portion of the waveform, inspiral or merger-ringdown, is the same used to recover the parameters from that portion.

²⁰ Pürrer 106, Taracchini et al. 117

²¹ Hannam et al. 75, Khan et al. 88, Bohé et al. 44

²² Abbott et al. 15

3.4.3 *Fit formulae for the mass and spin of the final black hole*

The consistency test we have developed relies on NR fitting formulae to map the binary's initial masses and spins into the mass and spin of the remnant black hole. There are a number of such fits available in the literature, of varying degrees of accuracy and generality. Here we consider a variety of recent fits for the final mass and spin.²³ We consider one set that is only applicable to nonspinning binaries (so we do not use the estimated spins in applying this) given in equations (29) of Pan *et al.*²⁴, and two sets applicable to binaries with aligned spins. The first set is from Healy, Lousto and Zlochower (HLZ)²⁵ and involves reasonably complicated implicit expressions given in Eq. (14) and Eq. (16) in that paper, with coefficients given in Table XI (we use the fourth-order fits). The second, simpler, though somewhat less accurate set is from Eq. (3.6) and Eq. (3.8) in Husa *et al.*²⁶ and only uses a single effective spin. The latter two fits were used in²⁷ to infer the final mass and spin of GW150914 and the HLZ fits were used in the implementation of the current test in Paper I and²⁸. For these fits, we use the projection of the spins along the orbital angular momentum when using a precessing waveform model, e.g., IMRPhenomPv2. The final mass and spin used to determine the ISCO frequency is not changed throughout the analysis, even when we are changing the fitting formulae. The calculation of the ISCO frequency uses the HLZ fits.

It is also possible to augment aligned-spin fits for the final spin to include the contribution from the in-plane spins, as was done for the HLZ fit in²⁹ and significantly increases its accuracy for precessing systems. As that reference shows for the HLZ fit, the basic aligned-spin final mass fit is already accurate for precessing systems when evaluated using the components of the spins along the orbital angular momentum. This augmentation was applied to the HLZ fit to infer the final spin of the binary black hole events from Advanced LIGO's first observing run in³⁰. We thus also consider this extension of the final spin expression for the HLZ and Husa *et al.* fits (HLZ aug and Husa *et al.* aug), as well as a new final spin fit for precessing systems from Hofmann, Barausse and Rezzolla (HBR)³¹ (we use the one with the smallest number of coefficients, which the authors recommend), which we pair with the HLZ final mass fit. We also

²³ While there are fits for the final mass and spin used in the two waveform models we employ, we do not just use those here, since they are not the most accurate and up-to-date ones: see Jiménez-Forteza *et al.*, which compares the final mass fit used in SEOBNRv2 and the final mass and spin fits used in IMRPhenomPv2 with more accurate fits. Note, however, that the additional calibrated terms in the merger-ringdown parts of these models may compensate for some of the slight inaccuracies of the final mass and spin fits used.

²⁴ Pan *et al.* 98

²⁵ James Healy, Carlos O. Lousto, and Yosef Zlochower. Remnant mass, spin, and recoil from spin aligned black-hole binaries. *Phys. Rev. D*, 90(10):104004, 2014. DOI: 10.1103/PhysRevD.90.104004

²⁶ Husa *et al.* 84

²⁷ Benjamin P Abbott *et al.* Observation of gravitational waves from a binary black hole merger. *Physical review letters*, 116(6):061102, 2016; and Benjamin P Abbott, R Abbott, TD Abbott, MR Abernathy, F Acernese, K Ackley, C Adams, T Adams, P Addesso, RX Adhikari, *et al.* Properties of the binary black hole merger gw150914. *Physical review letters*, 116(24):241102, 2016

²⁸ Abbott *et al.* 14

²⁹ N. K. Johnson-McDaniel, A. Gupta, P. Ajith, D. Keitel, O. Birnholtz, F. Ohme, and S. Husa. Determining the final spin of a binary black hole system including in-plane spins: Method and checks of accuracy. Technical Report LIGO-T1600168, 2016. <https://dcc.ligo.org/LIGO-T1600168/public>

³⁰ Benjamin P Abbott *et al.* Binary black hole mergers in the first advanced ligo observing run. *Physical Review X*, 6(4):041015, 2016; Benjamin P Abbott *et al.* GW151226: Observation of gravitational waves from a 22-solar-mass binary black hole coalescence. *Physical Review Letters*, 116(24):241103, 2016; and B. P. Abbott *et al.* Improved analysis of GW150914 using a fully spin-precessing waveform Model. *Phys. Rev. X*, 6(4):041014, 2016. DOI: 10.1103/PhysRevX.6.041014

³¹ Hofmann *et al.* 80

consider the augmented versions of both new aligned-spin fits that extend those in Husa *et al.* to include the spin difference (UIB aug)³², as well as a small update to the HLZ fits from Healy and Lousto (HL aug)³³. An average of these fits (HBR, UIB aug, and HL aug for the final spin, and just the second two for the final mass) was used to infer the final mass and spin of the binary coalescence that produced GW170104, as well as in the application of the IMR consistency test to that system³⁴.

In Fig. 3.4 (third row), we show that for the simple test case we consider, the two aligned-spin fits give almost identical results, as do the extensions using the in-plane spins, while the nonspinning fits still give a posterior that is consistent with zero. Here we use the precessing waveform model IMRPhenomPv2³⁵ for both the injection and recovery. We use it for the recovery in order to have nonzero in-plane spins, and use it (in its aligned-spin limit) for the injection so we are only testing different fits, not different waveform models here. Since we apply the same fitting formulae to infer the final mass and spin from both the inspiral and post-inspiral portions of the waveform, systematic errors in the fitting formulae do not translate into systematic errors in the test. Nevertheless, having more accurate fitting formulae might help the test to identify modified GR signals.

³² Jiménez-Forteza *et al.* 86

³³ Healy and Lousto 76

³⁴ Benjamin P Abbott *et al.* Gw170104: Observation of a 50-solar-mass binary black hole coalescence at redshift 0.2. *Physical Review Letters*, 118:221101, 2017

³⁵ Hannam *et al.* 75, Khan *et al.* 88, Bohé *et al.* 44

3.4.4 Effects of spin precession and higher modes

Although gravitational wave emission in the leading order is quadrupolar, higher order (nonquadrupole) modes can contain nonnegligible power if the system has large asymmetries (e.g., highly unequal masses or large, misaligned spins). Due the unavailability of waveform models that are accurate and computationally fast to generate, currently the parameter estimation is mostly performed making use of waveform templates that only model the quadrupole ($\ell = 2, m = \pm 2$) modes. This can potentially introduce systematic errors in the estimated parameters, which could be falsely taken for a deviation from GR. However, the systematic errors due to neglecting nonquadrupole modes are expected to be negligible for the case of binary black holes with moderate mass ratios and aligned/antialigned spins³⁶. In this chapter's population study we considered binaries with spins aligned/antialigned with the orbital angular momentum

³⁶ Abbott *et al.* 15, Varma and Ajith 123

so that there is no precession. However, fast-to-evaluate waveform templates that take into account the dominant precession effects are available ³⁷, which have been used for performing the IMR consistency test on the LIGO events GW150914 ³⁸ and GW170104 ³⁹.

We investigate the robustness of the IMR consistency test against the effects of precession and higher modes, making use of injected NR waveforms from the SXS waveform catalog ⁴⁰. We select two unequal mass ($m_1/m_2 = 1.228$) waveforms used in ⁴¹: SXS:BBH:0307, which has aligned spins ($a_{1,z} = 0.32$, $a_{2,z} = -0.5798$ ⁴²), and SXS:BBH:0308, which is a precessing system with spin magnitudes $a_1 = 0.3406$, $a_2 = 0.6696$ and aligned components $a_{1,z} = 0.3224$, $a_{2,z} = -0.5761$. We inject both systems with total masses of $65M_\odot$ (so their individual masses are 36 and $29M_\odot$, the same as for the previous injections), and with inclination angles of 0 . For parameter estimation, we use SEOBNRv2_ROM_DOUBLESPIIN as our template. The results are summarized in Fig. 3.4 (bottom panel): the test is robust against the presence of higher modes and spin precession in the comparable-mass regime.

³⁷ Hannam et al. 75, Khan et al. 88, Bohé et al. 44

³⁸ Abbott et al. 14

³⁹ Benjamin P Abbott et al. Gw170104: Observation of a 50-solar-mass binary black hole coalescence at redshift 0.2. *Physical Review Letters*, 118:221101, 2017

⁴⁰ Mroué et al. 95, SXS 3, Schmidt et al.

111

⁴¹ Abbott et al. 15

⁴² The aligned spin components for the NR injections used in section 3.4.4 have signs opposite to the ones used in the rest of the section; this is not a typographical error.

3.4.5 Effect of splitting the signal in the frequency domain

In the IMR consistency test, we check the consistency of the posteriors of the final mass and spin estimated from the early part of the signal (inspiral) with the same estimated from the late part of the signal (merger–ringdown). The split between the inspiral and merger–ringdown parts is done in the Fourier domain. This choice is purely made for convenience, since, in the Fourier domain, this amounts to simply setting the lower and upper limits of the likelihood integral in Eqs. (2.11) and (2.12).⁴³ There is a possibility that a fraction of the power from the inspiral can get deposited at high Fourier frequencies, or the power from the merger–ringdown parts to get deposited at low Fourier frequencies. This effect will be particularly pronounced for the ringdown signal, whose power is spread over a large range of Fourier frequencies. One may worry that this spectral leakage would cause the posteriors derived from the two regions of Fourier frequency to be automatically consistent (although, we have already demonstrated that when certain kinds of deviations from GR are present in the signal, the IMR consistency test is able to

⁴³ This is different from splitting the signals in time domain and then taking the Fourier transform, which will introduce additional artefacts in the Fourier transform due to edge effects or windowing.

identify them; see Sec. 3.3.2).

Below we show that the effect of spectral leakage is small for the case of cutoff frequencies that we choose. In order to demonstrate this, we do the following: We compute the Fourier transform of the NR waveform SXS:BBH:0253 (an aligned-spin system with $m_1/m_2 = 2$ and $a_{1,z} = a_{2,z} = 0.5$)⁴⁴ making use of the *stationary phase approximation* (SPA) [e.g., Eq. (3.7) of ⁴⁵]. The approximation here is that the power at a Fourier frequency f comes entirely from the time t_f (the saddle point) when the instantaneous frequency $F(t) := (d\varphi(t)/dt)/2\pi$ is equal to f . Here $\varphi(t)$ is the phase of the waveform. In this approximation, the magnitude of the Fourier transform of the NR waveform can be computed as

$$|\tilde{h}(f)| = \frac{A(t_f)}{\sqrt{\dot{F}(t_f)}} \quad (3.7)$$

where $A(t)$ is the time-domain amplitude of the NR waveform, and a dot denotes a time derivative.

If the Fourier transform computed using the SPA agrees well with numerically computed Fast Fourier Transform (FFT), this gives a strong indication that the spectral leakage is negligible. Fig. 3.10 compares the Fourier transform computed using the SPA with the FFT. The corresponding ISCO frequency f_{ISCO} is also shown, which is used to demarcate the inspiral and merger–ringdown parts. The plot suggests that the power at Fourier frequencies less than f_{ISCO} can be fully explained to be coming from the early times of the waveform (i.e., with instantaneous frequency $F(t) < f_{\text{ISCO}}$). The excellent agreement between the SPA and FFT at frequencies less than f_{ISCO} suggests that there is no appreciable spectral leakage between the two bands — almost all the power in the $f < f_{\text{ISCO}}$ ($f > f_{\text{ISCO}}$) band should come from the early (late) times. However, if we choose a transition frequency much higher than f_{ISCO} to demarcate the inspiral and merger–ringdown (say, the dominant QNM frequency, which is also shown in the figure) we expect significant spectral leakage between the two bands.

The definition of when the Fourier transform of a waveform computed using the SPA can be considered a faithful representation of the exact Fourier transform, can be made a bit more rigorous following the discussion in Sec. II.C of ⁴⁶. We introduce the instan-

⁴⁴ Abdul H. Mroué et al. A catalog of 174 binary black-hole simulations for gravitational-wave astronomy. *Phys. Rev. Lett.*, 111:241104, 2013. DOI: 10.1103/PhysRevLett.111.241104; and URL <http://www.black-holes.org/waveforms/>. SXS Gravitational Waveform Database
⁴⁵ Thibault Damour, Bala R. Iyer, and B. S. Sathyaprakash. Frequency domain P approximant filters for time truncated inspiral gravitational wave signals from compact binaries. *Phys. Rev. D*, 62:084036, 2000. DOI: 10.1103/PhysRevD.62.084036

⁴⁶ Thibault Damour, Bala R. Iyer, and B. S. Sathyaprakash. Frequency domain P approximant filters for time truncated inspiral gravitational wave signals from compact binaries. *Phys. Rev. D*, 62:084036, 2000. DOI: 10.1103/PhysRevD.62.084036

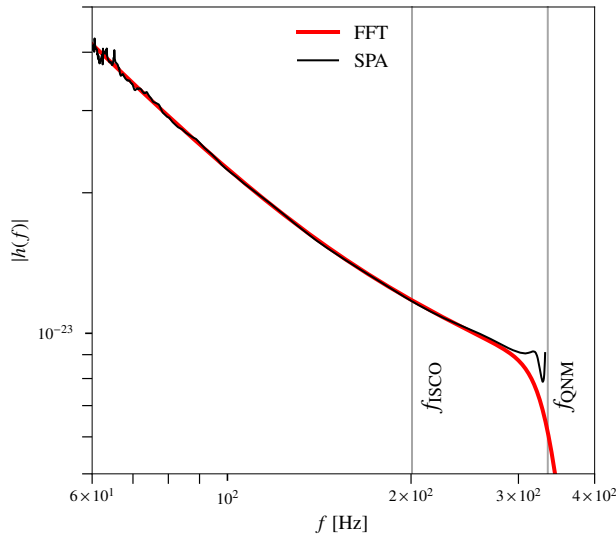


Figure 3.10: Comparison of the Fourier transform of the NR waveform SXS:BBH:0253 computed using the SPA with the exact Fourier transform computed using the FFT. The corresponding ISCO frequency f_{ISCO} is also shown, which is used to demarcate the inspiral and merger-ringdown parts. The plot suggests that the power at Fourier frequencies less than f_{ISCO} can be fully explained to be coming from the early times of the waveform. Also shown is the dominant QNM frequency, for reference. At high frequencies, the agreement between SPA and FFT becomes poor, indicating spectral leakage. The noise in the SPA at lower frequencies is due to the numerical noise in computing the frequency derivative.

taneous number of cycles spent near some instantaneous frequency $F(t)$, $N(F)$, defined as:

$$N(F) := \frac{F^2}{dF/dt} \quad (3.8)$$

It can then be shown that for the peak of the SNR logarithmic frequency-distribution f_p being comparable to the instantaneous frequency at which the signal itself shuts off, F_{max} , the simple frequency-windowed SPA will be a bad overlap $\tilde{h}(f)$ if $\sqrt{N_{F_{\text{max}}}}$ is not large. In other words, for the Fourier transform of a waveform computed using the SPA to be a faithful representation of the exact Fourier transform, $\tilde{h}(f)$, numerically computed by the Fast-Fourier-transform of the time-domain signal, $N_{F_{\text{max}}}$ should be large, or conversely $\frac{dF/dt}{F^2} \ll 1$, which is what we see in the third panel of Fig.3.11. Thus, if we need to perform this same analysis purely on the ringdown part (without including the merger), the analysis must be performed in the time domain. There is ongoing work in this direction about which more is described in Sec.3.5.

3.5 Future work

While we have investigated the reliability of our test to ensure its robustness, there remain further extensions of the test and more analyses to pursue. In particular, we have assumed that black holes in binaries have nonprecessing spins in the populations we simulate in

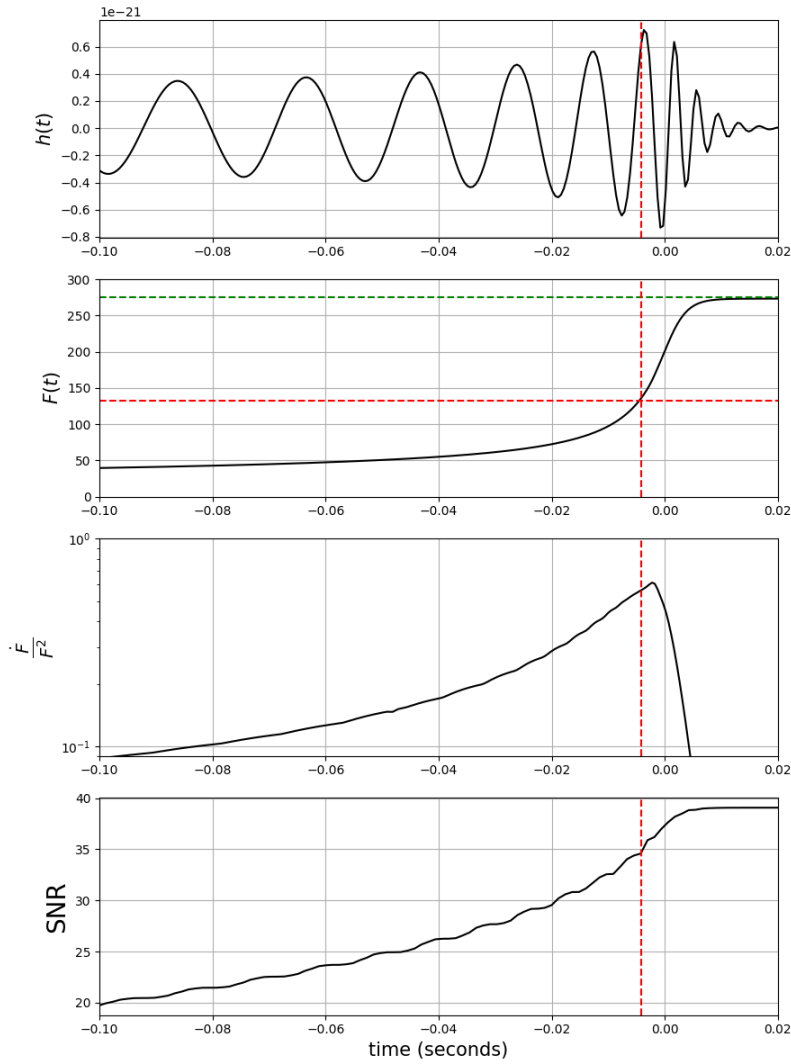


Figure 3.11: *Top Panel:* The time-domain gravitational signal $h(t)$ for a (non-spinning) binary black hole coalescence with initial masses $(36, 29)M_{\odot}$ directly overhead to the detector. *Second Panel:* The evolution of the instantaneous frequency of the gravitational wave chirp $F(t) = \frac{1}{2\pi} \frac{d\phi(t)}{dt}$. The red and green dashed horizontal lines represent the ISCO frequency of the remnant black hole, 132Hz, and the frequency of the dominant QNM of the remnant black hole, 274.9Hz, respectively. The red dashed vertical line represent the time corresponding to the ISCO frequency of 132Hz, and has the same definition in all four panels. *Third Panel:* The evolution of $\frac{dF}{dt}$ with time. *Bottom Panel:* The evolution of the SNR accumulated over time of the gravitational wave signal.

this chapter. We have also neglected the effect of nonquadrupole modes in the parameter estimation (although the fitting formulae for the remnant mass and spin include their contributions to the energy and angular momentum loss). While the effects of precession and nonquadrupole modes are expected to be negligible for the parameter estimation of comparable-mass binaries (see, e.g., ⁴⁷) their effects might be appreciable for binaries with large mass ratios and high spins. Waveform templates describing the spin precession through an effective spin parameter, notably the IMRPHENOMPv2 template ⁴⁸, are already available and have been used in parameter estimation. IMRPHENOMPv2 has been employed in the application of this test to GW150914 in ⁴⁹, to GW170104 in ⁵⁰, and in some of the robustness tests in Sec. 3.4. More recently, waveform templates describing the full double-spin precession effects have also become available ⁵¹. These templates can be employed in parameter estimation when precession effects are expected to be apparent. Fitting formulae for the remnant mass and spin valid for the case of precessing initial spins are already available; some of them have been used in this chapter itself. Waveform templates for binaries of spinning black holes that include the effect of nonquadrupole modes have started to become available ⁵², and they may help to avoid possible systematic errors due to neglecting nonquadrupole modes.

The robustness studies performed in this chapter are restricted to the case of single events with modest SNR. When a large number (~ 100) of events are combined to produce precise constraints on deviations from GR, even small systematic errors could become significant. Apart from the aspects discussed above, possible sources of errors include the finite accuracy of the GR waveform templates and the calibration of the gravitational wave detectors. We already have preliminary indications that combined posteriors from a large number of events could be dominated by such errors. Therefore, a careful characterisation of various systematic errors is required before we accumulate a large number of detections to analyse. We leave this as future work.

⁴⁷ Abbott et al. 15, Varma and Ajith 123

⁴⁸ Hannam et al. 75, Khan et al. 88, Bohé et al. 44

⁴⁹ Abbott et al. 14

⁵⁰ Abbott et al. 16

⁵¹ Pan et al. 99, Babak et al. 35

⁵² Lionel London, Sebastian Khan, Edward Fauchon-Jones, Xisco JimÁñez Forteza, Mark Hannam, Sascha Husa, Chinmay Kalaghatgi, Frank Ohme, and Francesco Pannarale. First higher-multipole model of spinning binary-black-hole gravitational waveforms. 2017

3.5.1 Implementation of the consistency test in the time-domain

The current generation of detectors is expected to be followed by a third generation of ground-based interferometric detectors, the Einstein Telescope⁵³ and Cosmic Explorer⁵⁴ (with ~ 10 times the sensitivity), as well as space-based detectors like the Laser Interferometer Space Antenna (LISA) (which is expected to observe super-massive binary black hole mergers in the frequency range $10^{-4} - 10^{-1}$ Hz). With these detectors one expects to observe binary black hole mergers with very high SNRs. Such an observation would allow us to isolate the ringdown and estimate the mass and spin of the final compact object directly from the QNM spectrum⁵⁵. This would allow us to do the consistency test as originally proposed in Hughes and Menou⁵⁶ in the context of the space-based LISA observatory, by isolating the early inspiral and late ringdown. In that case, considering a cutoff frequency in the ringdown signal increases the possibility of a fraction of power in the ringdown signal to get deposited to low frequencies. Hence, if one wants to perform the consistency test using only the inspiral and ringdown parts of the observed signal, the preferred method would be to split the signal and waveform in the time-domain, and estimate the parameters from each part independently. One can use a time $t = t_{cut}$ to separate $h(t)$ into two mutually-exclusive portions, like the inspiral and merger-ringdown portions, or can use two different times $t = t_{insp, end}$ and $t_{ring, start}$ to designate the times at which inspiral ends and ringdown starts respectively, while ignoring the merger phase completely. Since the data is, to a good approximation, coloured Gaussian, we could use the likelihood defined earlier in Eq.2.11, by taking a Fourier transform of the data truncated in the time-domain and applying appropriate window functions to take care of edge effects⁵⁷. Alternatively, one could whiten the data and template using the amplitude spectral density $\sqrt{S_n(f)}$ of the noise, and write the likelihood function in the time-domain as:

$$p_{\hat{n}}[\hat{d}(t) - \hat{h}(t)] \propto \exp\left[-\frac{1}{S_{\hat{n}}} \int_{t_{low}}^{t_{high}} (\hat{d}(t) - \hat{h}(t))^2 dt\right] \quad (3.9)$$

where $\{\hat{d}(t), \hat{h}(t)\}$ are the whitened data and template respectively, $\{t_{low}, t_{high}\}$ denote the interval during which the signal lasts and $S_{\hat{n}}$ is the frequency-independent PSD associated with the whitened

⁵³ Punturo et al. 105

⁵⁴ Dwyer et al. 66

⁵⁵ Swetha Bhagwat, Maria Okounkova, Stefan W Ballmer, Duncan A Brown, Matthew Giesler, Mark A Scheel, and Saul A Teukolsky. On choosing the start time of binary black hole ringdowns. *Physical Review D*, 97(10): 104065, 2018; and Gregorio Carullo, Laura van der Schaaf, Lionel London, Peter TH Pang, Ka Wa Tsang, Otto A Hannuksela, Jeroen Meidam, Michalis Agathos, Anuradha Samajdar, Archisman Ghosh, et al. On the empirical verification of the black hole no-hair conjecture from gravitational-wave observations. *arXiv preprint arXiv:1805.04760*, 2018

⁵⁶ Scott A. Hughes and Kristen Menou. Golden binaries for LISA: Robust probes of strong-field gravity. *Astrophys. J.*, 623:689, 2005. DOI: 10.1086/428826

⁵⁷ Miriam Cabero, Collin D Capano, Ofek Fischer-Birnholtz, Badri Krishnan, Alex B Nielsen, and Alex H Nitz. Observational tests of the black hole area increase law. *arXiv preprint arXiv:1711.09073*, 2017

noise $\hat{n}(t)$. A complete derivation of the process of whitening and the above form of the likelihood function is given in Appendix A.3.

As mentioned above, if a signal is observed with a high enough SNR, it might be possible to use two different times $t = t_{\text{insp, end}}$ and $t_{\text{ring, start}}$. In that case, one can isolate the ringdown and estimate the mass and spin of the remnant by fitting a QNM spectrum to the ringdown signal given by:

$$h_{\text{ring}}(t) = \sum_n A_n e^{((t-t_{\text{ring}})/\tau_n)} \cos(2\pi f_{n,\text{QNM}}(t - t_{\text{ring}}) - \phi_n) \quad (3.10)$$

where n runs over all the modes of the QNM spectrum and t_{ring} is the same as $t_{\text{ring, start}}$ mentioned above, denoting the start of the ringdown. If we restrict ourselves to just the leading order contribution to the QNM spectrum, then Eq. 3.10 becomes:

$$h_{\text{ring}}(t) = A_0 e^{((t-t_{\text{ring}})/\tau_0)} \cos(2\pi f_{0,\text{QNM}}(t - t_{\text{ring}}) - \phi_0) \quad (3.11)$$

where A_0 , τ_0 , $f_{0,\text{QNM}}$ and ϕ_0 are the amplitude, damping time, damping frequency and the phase of the dominant QNM mode. Since the energy and angular momentum emitted into gravitational waves is maximum during the merger phase, such an observation would allow us to do a consistency test by ignoring the merger altogether, and thus placing the tightest constraints possible on the energy and angular momentum loss during merger just from the early inspiral and late ringdown phases. This would then allow us to make statements on the Hawking's area theorem ⁵⁸, size of extra-dimensions ⁵⁹, and several other theoretical predictions.

⁵⁸ Miriam Cabero, Collin D Capano, Ofek Fischer-Birnholtz, Badri Krishnan, Alex B Nielsen, and Alex H Nitz. Observational tests of the black hole area increase law. *arXiv preprint arXiv:1711.09073*, 2017

⁵⁹ Kent Yagi, Norihiro Tanahashi, and Takahiro Tanaka. Probing the size of extra dimensions with gravitational wave astronomy. *Physical Review D*, 83(8): 084036, 2011

Summary

In this chapter we have provided a detailed description of a test of GR based on the consistency between the inspiral, merger and ringdown parts of observed gravitational wave signals from coalescing binary black holes. We demonstrate how the likelihoods from multiple binary black hole events can be combined to produce tighter

constraints on parameters describing a deviation from GR. In order to illustrate how this test might be able to detect certain types of deviations from GR, we generate internally consistent kludge waveforms which disagree with the GR prediction of the radiated energy and angular momentum, by increasing the flux radiated into gravitational waves. We then simulate a population of binaries modelled by these modified GR waveforms. By combining the results from multiple events, we demonstrate how this test might be able to detect small deviations from GR. For the case of single events with parameters similar to LIGO's first binary black hole observation, we also demonstrate the robustness of the consistency test against specific choices of various analysis parameters, such as the choice of the transition frequency used to demarcate the inspiral and merger-ringdown parts, the specific waveform approximant, fitting formulae for the mass and spin of the remnant black hole, etc. We finally end with a look at future work in this direction along with a possible implementation of the test in the time-domain keeping in mind future gravitational wave detectors which will come up in the upcoming years to decades.

4 | Gravitational Wave Observations by the Advanced Detectors and the Inspiral Merger Ringdown Consistency Test

The twin detectors of the Advanced LIGO network in Hanford, Washington and Livingston, Louisiana have concluded two observing runs, the first from September 2015-January 2016, and the second from December 2016-August 2017. During the first observing run, the Advanced LIGO detectors observed gravitational waves from two binary black hole mergers, GW150914 and GW151226, and a candidate event called LVT151012. During the second observing run, two more binary black hole events were detected, GW170104 and GW170608, before advanced Virgo joined the network of detectors in August, 2017. GW170814, a binary black hole merger and GW170817, a binary neutron star merger, were both detected by a three-detector network including Advanced Virgo. We summarise the basic properties of all the gravitational wave detections till date in Table 4.1.

Table 4.1: All published gravitational wave observations by the Advanced LIGO-Virgo detector network, along with a list of their relevant parameters. We do not have information about the spin of the remnant object of the binary neutron star merger, GW170817.

GW event	Primary mass (M_{\odot})	Secondary mass (M_{\odot})	Remnant mass (M_{\odot})	Remnant spin	Luminosity distance (Mpc)	SNR
GW150914	36^{+5}_{-4}	29^{+4}_{-4}	62^{+4}_{-4}	$0.67^{+0.05}_{-0.07}$	410^{+160}_{-180}	23
LVT151026	23^{+18}_{-6}	13^{+4}_{-5}	35^{+14}_{-5}	$0.66^{+0.09}_{-0.10}$	1000^{+500}_{-500}	10
GW151226	14^{+8}_{-4}	7.5^{+2}_{-2}	21^{+6}_{-2}	$0.74^{+0.06}_{-0.06}$	440^{+180}_{-190}	13.0
GW170104	31^{+8}_{-6}	19^{+5}_{-6}	49^{+6}_{-5}	$0.64^{+0.09}_{-0.20}$	880^{+450}_{-390}	13
GW170608	12^{+4}_{-2}	7^{+2}_{-2}	18^{+5}_{-1}	$0.69^{+0.04}_{-0.05}$	340^{+140}_{-140}	13
GW170814	31^{+6}_{-3}	25^{+3}_{-4}	53^{+3}_{-3}	$0.70^{+0.07}_{-0.05}$	540^{+130}_{-210}	18
GW170817	1.36 – 1.60	1.17 – 1.36	$< 2.74^{+0.04}_{-0.01}$		40^{+8}_{-14}	32

The signal-to-noise ratio (SNR) with which a gravitational wave is observed, is an important factor in reliable parameter estimation. The IMR consistency test involves estimating the final mass and spin of the remnant black hole using two different parts of the waveform through Bayesian inference. Hence for the purpose of the test, it is additionally important how the total SNR is split between the individual parts. We use the gravitational wave frequency of the innermost stable circular orbit (ISCO) of the remnant Kerr black hole ¹, f_{ISCO} , as the frequency to divide the signal into a low-frequency part and a high-frequency part, and consequently this is what determines how the SNR gets split. As we have seen in Sec.3.1, the mass M_f and dimensionless spin magnitude a_f of the final (remnant) black hole are functions of the initial masses and spins,

$$M_f = M_f(m_1, m_2, \mathbf{a}_1, \mathbf{a}_2), \quad a_f = a_f(m_1, m_2, \mathbf{a}_1, \mathbf{a}_2), \quad (4.1)$$

With the knowledge of the mass and spin of the final Kerr black hole, one can then compute the frequency at the Kerr ISCO radius as:

$$f_{\text{ISCO}} = \frac{1}{\pi} r_{\text{ISCO}}^{-3/2} (1 - a_f r_{\text{ISCO}}^{-3/2} + a_f^2 r_{\text{ISCO}}^{-3}) \quad (4.2)$$

where r_{ISCO} is the radius at ISCO, given by:

$$r_{\text{ISCO}} = M_f \left(3 + Z_2 \pm \sqrt{(3 - Z_1)(3 + Z_1 + 2Z_2)} \right) \quad (4.3)$$

$$Z_1 = 1 + (1 - a_f^2)^{1/3} \left[(1 + a_f)^{1/3} + (1 - a_f)^{1/3} \right] \quad (4.4)$$

$$Z_2 = \sqrt{3a_f^2 + Z_1^2} \quad (4.5)$$

We see that f_{ISCO} scales inversely as mass. This means that while heavier systems will coalesce at lower frequencies, systems with low mass will coalesce at higher frequencies. Hence, the IMR consistency test targets systems that coalesce near the most sensitive part of the sensitivity band of the detectors, such that there is appreciable SNR in both segments of the waveform to do parameter estimation. In that regard, we find GW151226, GW170608 and GW170817 to be extremely low mass systems, which coalesce near the higher frequency band of the detectors. At that point the SNR left in the merger-ringdown portion of the waveform is too low for reliable parameter estimation. ² Hence, we have performed the IMR consistency test on GW150914 and GW170104 (from which we have published results),

¹ James M. Bardeen, William H. Press, and Saul A Teukolsky. Rotating black holes: Locally nonrotating frames, energy extraction, and scalar synchrotron radiation. *Astrophys. J.*, 178:347, 1972. DOI: 10.1086/151796

² Of course in the case of the binary neutron star merger GW170817, there are various theories about the post-merger remnant object, a summary of which can be found here [26].

and work is currently ongoing for GW170814 (at the time of writing this thesis). We haven't performed the test on the LVT151012. For the remainder of the chapter we will discuss the analysis done on the events, GW150914, GW170104 and GW170814.

4.1 GW150914

On September 14, 2015, at around 3:20 PM Indian Standard Time, the twin detectors of the Advanced LIGO recorded a candidate event. The signal arrived at the Livingston detector first, and 7 milliseconds later, was observed at the Hanford detector. The signal was first picked up by a low-latency generic unmodelled search pipeline that looks for gravitational wave transients in the form of excess power over the background ³, and was reported within three minutes of data acquisition. The signals in both detectors showed similar pattern in which the power rose over the background as a function of time in the manner similar to a characteristic chirp of a gravitational wave signal from a compact binary coalescence. The initial *burst* search was followed by a more targeted search where data was cross-correlated with a family of theoretically predicted binary black hole template waveforms. There were two independent matched-filtering search pipelines ⁴, and both confirmed GW150914 to be a confident detection, rising above the noise background at more than 5σ confidence level, with a combined SNR of 23. At the same time, extensive investigations were done to rule out any environmental or non-astrophysical origin of the signal. Analyses of detector noise around the event suggested that the chances of a random noise fluctuation mimicking GW150814 was less than 1 in about 200,000 years.

The source properties of GW150914 were estimated using a coherent Bayesian analysis, using GR based waveform models. There were two waveform models used: a phenomenological model with an effective parameter describing precession (IMRPhenomPv2) and an effective-one-body waveform with the spins on the individual black holes parallel to the orbital angular momentum (SEOBNRv2). Parameter estimation established that GW150914 was consistent with the coalescence of a binary black hole system in GR with initial masses $35.4^{+5.0}_{-3.4}M_{\odot}$ and $29.8^{+3.3}_{-4.3}M_{\odot}$, resulting in the formation of a remnant black hole with mass $62.2^{+3.7}_{-3.4}M_{\odot}$ (Fig.4.1). Thus around

³BP Abbott, R Abbott, TD Abbott, MR Abernathy, F Acernese, K Ackley, C Adams, T Adams, P Addesso, RX Adhikari, et al. Observing gravitational-wave transient gw150914 with minimal assumptions. *Physical Review D*, 93(12):122004, 2016

⁴BP Abbott, R Abbott, TD Abbott, MR Abernathy, F Acernese, K Ackley, C Adams, T Adams, P Addesso, RX Adhikari, et al. GW150914: First results from the search for binary black hole coalescence with advanced ligo. *Physical Review D*, 93(12):122003, 2016

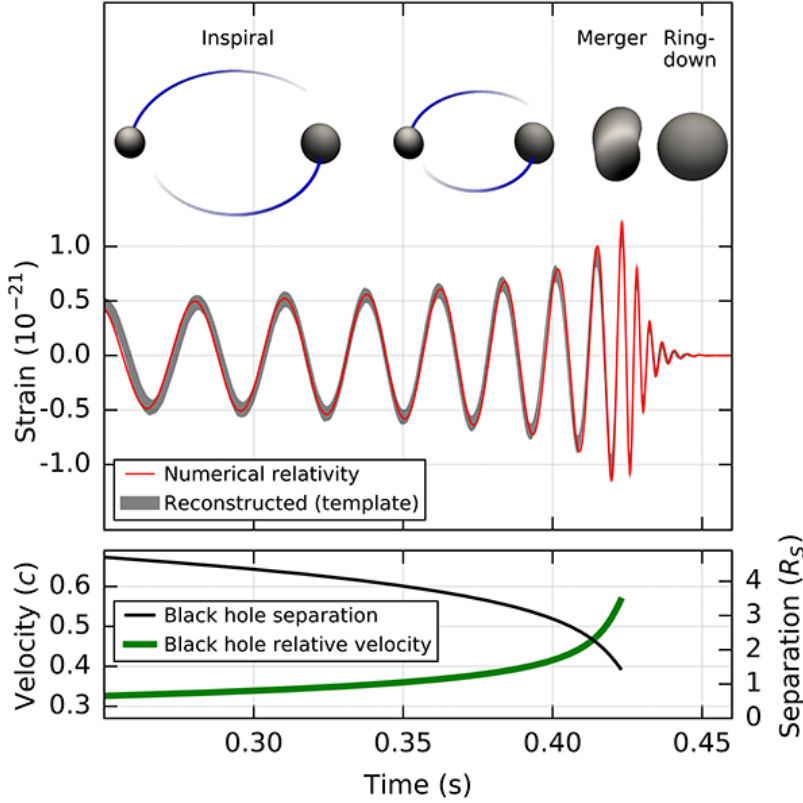


Figure 4.1: Top: Estimated gravitational-wave strain amplitude from GW150914. The inset images show numerical relativity models of the black hole horizons as the black holes coalesce. Bottom: The Keplerian effective black hole separation in units of Schwarzschild radii, R_s and the effective relative velocity given by the post-Newtonian parameter v/c . The figure and caption courtesy: GW150914 detection paper [13].

$3M_{\odot}$ was converted into gravitational waves, which led to a peak luminosity of $3.6_{-0.4}^{+0.5} \times 10^{56}$ erg/s which was more than ten times greater than the total luminosity of all the stars in the observable Universe put together. Although the measurements of the spins of the initial black holes were consistent with them being non-spinning, the final black hole was definitely spinning, with the dimensionless spin parameter $a_f = 0.67$. The distance to the binary was estimated at 410_{-180}^{+160} Mpc, or around 1.3 billion light years away.

We performed the inspiral-merger-ringdown consistency test on GW150914 to show that the entire GW150914 waveform does not deviate from the predictions of a binary black-hole coalescence in GR. For the purpose of this test, we chose $f_{\text{GW}}^{\text{end insp}} = 132$ Hz as the frequency at which the late inspiral phase ends. In Fig. 4.2 we plot the EOBNR maximum a posteriori probability (MAP) waveform ⁵ and its 90% credible intervals, as well as the corresponding instantaneous frequency; the vertical line marks $f^{\text{end insp}}$.

To perform the test, we first truncated the frequency-domain representation of the waveforms to lie between 20 Hz to $f_{\text{GW}}^{\text{end insp}}$, and

⁵ Abbott et al. 7

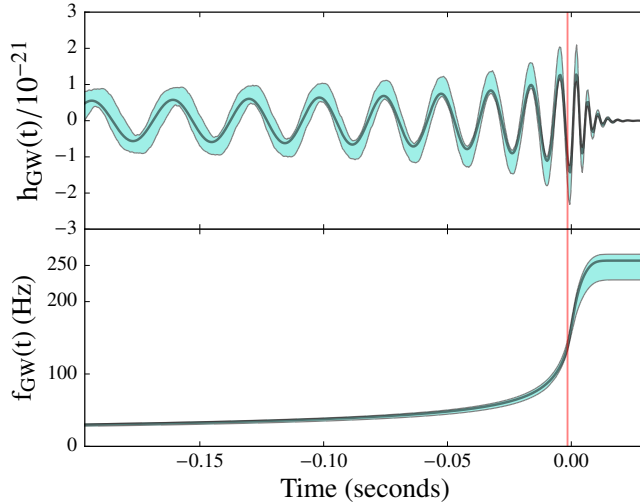


Figure 4.2: MAP estimate and 90% credible regions for (upperpanel) the waveform and (lower panel) the gravitational wave frequency of GW150914 as estimated by the LALINFERENCE analysis [7]. The solid lines in each panel indicate the most-probable waveform from GW150914 [7] and its gravitational wave frequency. We mark with a vertical line the instantaneous frequency $f_{\text{GW}}^{\text{end insp}} = 132$ Hz, which is used in the IMR consistency test to delineate the boundary between the frequency-domain inspiral and postinspiral parts. The figure and caption is from the GW150914 testing GR paper [14]

we estimated the posterior distributions of the binary’s component masses and spins using this “inspiral” (low-frequency) part of the observed signal, using the nested-sampling algorithm in the LALINFERENCE software library⁶. We then used the same fitting formulae as described in Chapter 3 to compute posterior distributions of the remnant’s mass and spin. Next, we estimated the final mass and spin from the complementary “post-inspiral” (high-frequency) signal, by restricting the waveform between $f_{\text{GW}}^{\text{end insp}}$ and 1024 Hz, the Nyquist frequency for a sampling rate of 2048 Hz used for the analysis. Again, we derived the posterior distributions of the component masses and spins, and (by way of NR-derived formulae) of the mass and spin of the final compact object. We note that the MAP waveform has an expected $\text{SNR}_{\text{det}} \sim 19.5$ if we truncate its frequency-domain representation to have support between 20 and 132 Hz, and ~ 16 if we truncate it to have support between 132 and 1,024 Hz. Finally, we compare these two estimates of the final mass M_f and dimensionless spin a_f , and compare them also against the estimate performed using full IMR waveforms. In all cases, we average the posteriors obtained with the EOBNR and IMRPHENOM waveform models, following the procedure outlined in Ref. 7.

This test is similar in spirit to the χ^2 gravitational wave search statistic⁸, which divides the model waveform into frequency bands and checks that the SNR accumulates as expected across those bands. Large matched-filter SNR values which are accompanied by large χ^2 statistic are very likely due either to noise glitches, or to a mismatch

⁶J. Veitch et al. Parameter estimation for compact binaries with ground-based gravitational-wave observations using the LALInference software library. *Phys. Rev. D*, 91(4):042003, February 2015. DOI: 10.1103/PhysRevD.91.042003

⁷ Benjamin P Abbott, R Abbott, TD Abbott, MR Abernathy, F Acernese, K Ackley, C Adams, T Adams, P Addesso, RX Adhikari, et al. Properties of the binary black hole merger gw150914. *Physical review letters*, 116(24):241102, 2016

⁸ Bruce Allen. A χ^2 time-frequency discriminator for gravitational wave detection. *Phys. Rev. D*, 71:062001, 2005. DOI: 10.1103/PhysRevD.71.062001; and BP Abbott, Richard Abbott, TD Abbott, MR Abernathy, Fausto Acernese, Kendall Ackley, Carl Adams, Thomas Adams, Paolo Addesso, RX Adhikari, et al. Gw150914: Implications for the stochastic gravitational-wave background from binary black holes. *Physical review letters*, 116(13):131102, 2016

between the signal and the model matched-filter waveform. Conversely, reduced- χ^2 values near unity indicate that the data are consistent with waveform plus the expected detector noise. Thus, large χ^2 values are a warning that some parts of the waveform are fit much worse than others, and thus the candidates may be due to instrument glitches that are very loud, but do not resemble binary-inspiral signals. However, χ^2 tests are performed by comparing the data with a single theoretical waveform, while in this case we allow the inspiral and post-inspiral partial waveforms to select different physical parameters. Thus, this test should be sensitive to subtler deviations from the predictions of GR.

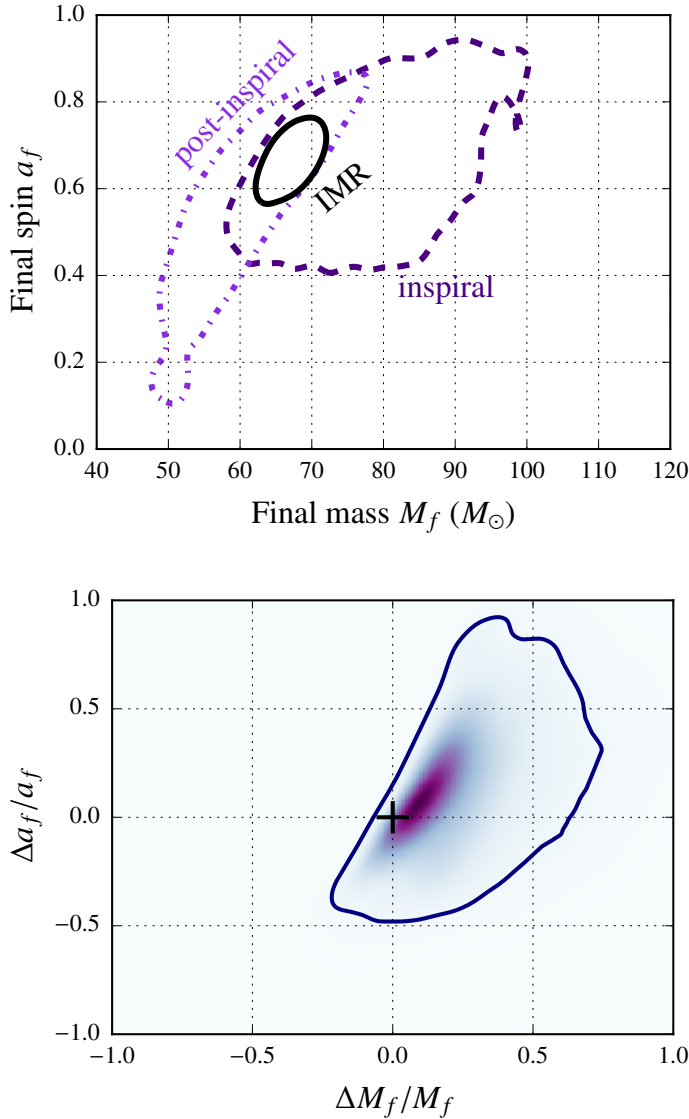


Figure 4.3: *Top panel:* 90% credible regions in the joint posterior distributions for the mass M_f and dimensionless spin a_f of the final compact object as determined from the inspiral (dark violet, dashed) and post-inspiral (violet, dot-dashed) signals, and from a full inspiral–merger–ringdown analysis (black). *Bottom panel:* Posterior distributions for the parameters $\Delta M_f/M_f$ and $\Delta a_f/a_f$ that describe the fractional difference in the estimates of the final mass and spin from inspiral and post-inspiral signals. The contour shows the 90% confidence region. The plus symbol indicates the expected GR value $(0,0)$. The figure and caption is from the GW150914 testing GR paper [14]

In Fig. 4.3 we summarise our findings. The top panel shows the posterior distributions of M_f and a_f estimated from the inspiral and post-inspiral signals, and from the entire IMR waveform. The plot confirms the expected behaviour: the inspiral and post-inspiral 90% confidence regions (defined by the isoprobability contours that enclose 90% of the posterior) have a significant region of overlap. As a sanity check (which strictly speaking is not part of the test of GR that is being performed) we also produced the 90% confidence region computed with the full IMR waveform; it lies comfortably within this overlap. We verified that these conclusions are not affected by the specific formula ⁹ used to predict M_f and a_f , nor by the choice of $f_{\text{GW}}^{\text{end insp}}$ within ± 50 Hz. To assess the significance of our findings more quantitatively, we define parameters $\Delta M_f / M_f$ and $\Delta a_f / a_f$ that describe the fractional difference between the two estimates of the final mass and spin, and calculate their joint posterior distribution, using for (M_f, a_f) the posterior distribution obtained from the full IMR waveform. The result is shown in the bottom panel of Fig. 4.3; the solid line marks the isoprobability contour that contains 90% of the posterior. The plus symbol indicates the null $(0, 0)$ result expected in GR, which lies on the isoprobability contour that encloses 28% of the posterior.

We checked that if we perform this analysis on NR signals added to Advanced LIGO instrumental noise, the null $(0, 0)$ result expected in GR lies within the iso-probability contour that encloses 68% of the posterior roughly 68% of the time, as expected from random noise fluctuations. By contrast, our test can rule out the null hypothesis (with high statistical significance) when analysing a simulated signal that reflects a significant GR violation in the frequency dependence of the energy and angular momentum loss ¹⁰, even when we choose violations which would be too small to be noticeable in double-pulsar observations ¹¹; for an explicit example we refer to Fig.3.1. This includes signals with χ^2 value close to unity, so that they would not have been missed by the modelled-signal searches. Thus, our inspiral–merger–ringdown test shows no evidence of discrepancies with the predictions of GR.

The IMR consistency test was among a handful of tests that was used to establish the consistency of GW150914, with a binary black hole coalescence predicted by GR, and was also one of the first tests

⁹ Healy et al. 77, Pan et al. 98, Husa et al. 84

¹⁰ Abhirup Ghosh, Archisman Ghosh, Nathan K Johnson-McDaniel, Chandra Kant Mishra, Parameswaran Ajith, Walter Del Pozzo, David A Nichols, Yanbei Chen, Alex B Nielsen, Christopher PL Berry, et al. Testing general relativity using golden black-hole binaries. *Physical Review D*, 94(2):021101, 2016

¹¹ Norbert Wex. Testing relativistic gravity with radio pulsars. *arXiv preprint arXiv:1402.5594*, 2014

of GR in the highly relativistic and strong-field dynamical regime of gravity.

4.2 GW_{170104}

On January 4, 2017 at 10:11:58.6 UTC (\sim 3:42 PM IST), the two Advanced LIGO detectors observed another gravitational wave signal produced by a high-mass binary black hole coalescence. The signal arrived at Hanford \sim 3 ms before Livingston and was detected with a combined SNR of 13. The detection was made on the first day after the resumption of the second observing run (after a winter-break) for the Advanced LIGO detectors, but at the time of GW_{170104} , both the detectors were in an observation-ready state, with sensitivities typical of the observing run to date. Subsequent data quality checks confirmed that there was no evidence of instrumental or environmental disturbances contributing to GW_{170104} . GW_{170104} was identified first by low-latency searches, and then by two offline matched-filter analyses, using 5.5 days of coincident data between 4-22 January 2017. It was a highly confident detection with false alarm rate of < 1 in 70000 years.

Parameter estimation confirmed that GW_{170104} was produced by the coalescence of two stellar-mass black holes of initial masses $31.2^{+8.4}_{-6.0}M_{\odot}$ and $19.4^{+5.3}_{-5.9}M_{\odot}$ respectively forming a remnant black hole of mass $48.7^{+5.7}_{-4.6}M_{\odot}$ and spin 0.64. Like in the case of GW_{150914} , the initial spin measurements were poor, but the measurement of the effective spin parameter χ_{eff} seemed to disfavour a large total spin positively aligned with the orbital angular momentum, but did not exclude zero spins. No meaningful constraints were obtained on the precession of the system through the measurement of the effective spin precession parameter χ_p . However, GW_{170104} might have originated much farther away than any of the other LIGO detections at a luminosity distance of 880^{+450}_{-390} Mpc.

Like GW_{150914} , GW_{170104} allowed us to test GR in the strong-field regime and constrain possible deviations from the expected behaviour of GR which only manifest in the most extreme conditions, where spacetime is highly dynamical. We performed the IMR consistency test to check whether the low-frequency, inspiral-dominated portion of the waveform was consistent with the high-frequency,

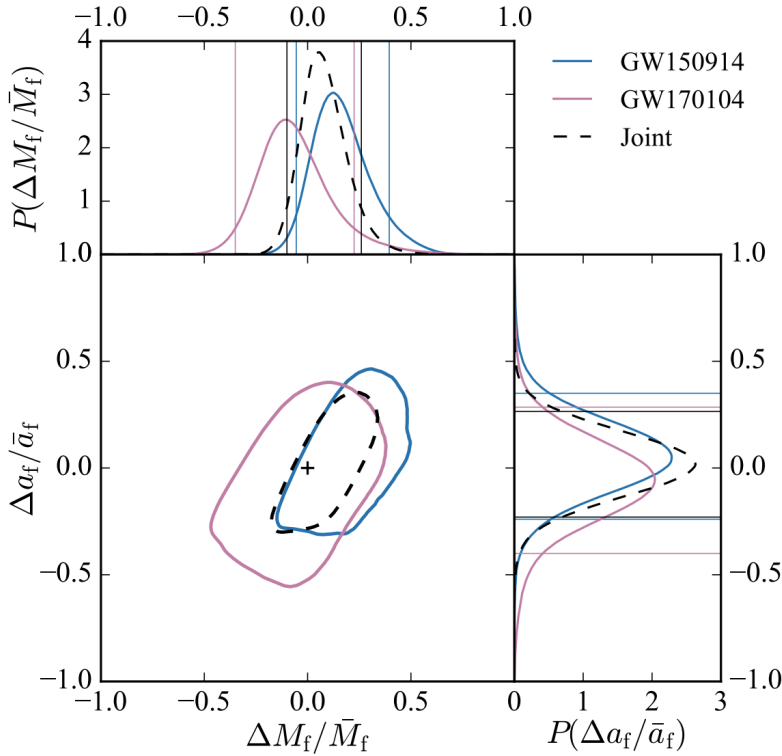


Figure 4.4: Posterior probability distributions for the fractional differences in the remnant black hole mass M_f/\bar{M}_f and spin a_f/\bar{a}_f calculated using the low-frequency (inspiral) and high-frequency (merger-ringdown) parts of the waveform. The GR solution is at $(0,0)$; shown in the two-dimensional plot as a black + marker. The contours show the 90% credible region, the lines in the one-dimensional histograms mark the 90% credible interval. We show the posteriors for GW170104 and GW150914, as well as the combined posterior using both. The figure and caption is from the GW170104 detection paper [16]

merger-ringdown portion. The two parts were divided at 143 Hz, a frequency close to the median inferred (detector-frame) innermost-stable-circular-orbit frequency of the remnant Kerr black hole. The two frequency ranges were analysed separately, and the inferred parameters were compared. The test used the estimated final black hole mass and spin (calculated from the component masses and spins using numerical-relativity fits. We know that if the waveform is compatible with the predictions of GR, we expect that the parameters inferred from the two pieces will be consistent with each other, although the difference will not, in general, be zero because of detector noise. In Fig. 4.4, we show the posteriors on the fractional difference in the two estimates of the final mass and spin for GW170104 and GW150914, as well as the combined posterior. The posterior for GW170104 is broader, consistent with this event being quieter, and having a lower total mass, which makes it harder to measure the post-inspiral parameters. The width of the 90% credible intervals for the combined posteriors of $\Delta M_f/\bar{M}_f$ are smaller than those computed from GW170104 (GW150914) by a factor of 1:6 (1:3), and the intervals for $\Delta a_f/\bar{a}_f$ are improved by a factor of 1:4 (1:2).

4.3 *GW170814*

GW170814 was the fourth confirmed binary black hole coalescence detected by the Advanced LIGO detectors. However, it was also observed by the advanced Virgo detector in Italy, making it the first three-detector observation of gravitational waves. The signal arrived first at the LIGO Livingston detector and then at Hanford and Virgo, 8ms and 14ms later, respectively, and was observed with a three-detector combined SNR of 18. *GW170814* was produced by the coalescence of two stellar-mass black holes of initial masses $30.5^{+5.7}_{-3.0}M_{\odot}$ and $25.3^{+2.8}_{-4.2}M_{\odot}$ producing a final black hole of mass $53.2^{+3.2}_{-2.5}M_{\odot}$. The binary was at a distance of 540^{+130}_{-210} Mpc and was observed with a false alarm rate of less than 1 in 27000 years.

We have performed the IMR consistency test on the event with a cutoff frequency of 161 Hz. At the time of writing this thesis, investigations are still ongoing with results expected to be published in an upcoming collaboration paper. The initial results reported in the *GW170814* detection paper, show that the mass and spin of the final remnant black hole as estimated from the inspiral and merger-ringdown portions respectively, are consistent with each other.

Summary and Conclusions

The IMR consistency test was among a handful of tests that was used to establish the consistency of LIGO's first gravitational wave observation, *GW150914*, with a binary black hole system predicted by GR. Since the test is based on estimating the final mass and spin of the binary black hole system independently from the inspiral and merger-ringdown portions of the waveform, it relies on the two independent portions having sufficient SNR to conduct reliable parameter estimation. The IMR consistency test has hence been demonstrated on the two high-mass binary black hole events, *GW150914* and *GW170104*, where this is indeed the case. The low-mass events are dominated by a long inspiral, and not enough (if any at all) SNR in the post-inspiral

regime to do parameter estimation. We further demonstrated that we can obtain tighter bounds on possible deviations from GR by combining posteriors from different events. Investigations on the other high-mass event GW170814 detected by the LIGO-Virgo network is ongoing at the time of writing this thesis.

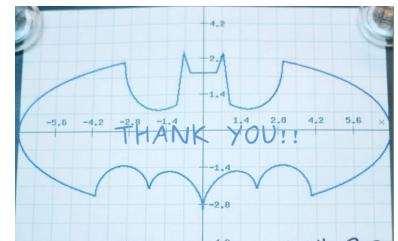
The IMR consistency test will continue to be demonstrated on gravitational wave observations by the Advanced LIGO-Virgo detector network as well as future gravitational wave detectors. The current generation of detectors are expected to be followed by a third generation of ground-based interferometric detectors, the Einstein Telescope and Cosmic Explorer (with ~ 10 times the sensitivity), as well as space-based detectors like the Laser Interferometer Space Antenna (LISA) (which is expected to observe super-massive binary black hole mergers in the frequency range $10^{-4} - 10^{-1}$ Hz). With the detection of seven gravitational wave events by the Advanced LIGO-Virgo detector network in their last two observing runs, we have firmly begun an exciting era of gravitational wave astronomy as well as multi-messenger astronomy. The upcoming years will be a period of active research which will help us address long-standing questions in theoretical physics, astrophysics and cosmology using information from gravitational waves. It will also perhaps lead us into the unknown, revealing new mysteries about our universe. The future is truly exciting!

5 | Acknowledgements

"My lamp burns low, and I have written far into the night."

David Copperfield, Charles Dickens, 1850

This moment in time is a culmination of a beautiful academic journey of nearly three decades that finally landed me at the International Centre for Theoretical Sciences and in the LIGO Scientific Collaboration. This moment in time is also a consequence of the love, support, encouragement, and criticism accumulated over that entire journey from a complex web of interactions that I call my family, friends, teachers, professors, colleagues and collaborators. For that, and to them, since I could never find the words to adequately express my gratitude, I simply say "Thank you". Finally, for the purpose of a doctoral dissertation, it is important to be a good academic. In life, it is more important to be a good human being. In that regard and a lot more, I am indebted to a few people in ways they would never know. Thank you, Arup, Ranjita, Jayita and Ajith.



"It was the best of times, it was the worst of times.

It was the age of wisdom, it was the age of foolishness."

A Tale of Two Cities, Charles Dickens, 1859

6 | Publications

Publications relevant to the thesis

- Abhirup Ghosh, Archisman Ghosh, N. K. Johnson-McDaniel, C. K. Mishra, P. Ajith, W. Del Pozzo, D. A. Nichols, Y. Chen, A. B. Nielsen, C. P. L. Berry, L. London; Testing general relativity using golden black-hole binaries; *Phys. Rev. D* 94, 021101(R) (2016); arXiv:1602.02453 [gr-qc]
- Abhirup Ghosh, Nathan K Johnson-McDaniel, Archisman Ghosh, Chandra Kant Mishra, Parameswaran Ajith, Walter Del Pozzo, Christopher PL Berry, Alex B Nielsen, Lionel London; Testing general relativity using gravitational wave signals from the inspiral, merger and ringdown of binary black holes; *Classical and Quantum Gravity* 35 (1), 014002; arXiv:1704.06784
- B. P. Abbott et al. [LIGO Scientific and Virgo Collaborations], Observation of Gravitational Waves from a Binary Black Hole Merger, *Phys. Rev. Lett.* 116, 061102 (2016).
- B.P. Abbott et al. [LIGO Scientific and Virgo Collaborations], Tests of general relativity with GW150914, *Phys. Rev. Lett.* 116, 221101 (2016)
- B.P. Abbott et al. [LIGO Scientific and Virgo Collaboration], Binary Black Hole Mergers in the first Advanced LIGO Observing Run, *Phys. Rev. X* 6, 041015
- B.P. Abbott et al. [LIGO Scientific and Virgo Collaboration], GW170104: Observation of a 50-Solar-Mass Binary Black Hole Coalescence at Redshift 0.2, *Phys. Rev. Lett.* 118, 221101
- B.P. Abbott et al. [LIGO Scientific and Virgo Collaboration], GW170814: A three-detector observation of gravitational waves from a binary black hole coalescence, *Phys. Rev. Lett.* 119, 141101

Other Publications

- Siddharth Dhanpal, Abhirup Ghosh, Ajit Kumar Mehta, P. Ajith, and B. S. Sathyaprakash; A “no-hair” test for binary black holes; arXiv:1804.03297 (Submitted to PRL)
- Abhirup Ghosh, Samit Bhattacharyya, Somdatta Sinha, Amit Apte; Parameter Estimation in Models with Complex Dynamics; arXiv: 1705.03868 (submitted to Chaos: An Interdisciplinary Journal of Nonlinear Science)
- B.P. Abbott et al. [LIGO Scientific and Virgo Collaboration], GW170608: Observation of a 19-solar-mass Binary Black Hole Coalescence, The Astrophysical Journal Letters, 851(2), L35; arXiv:1711.05578 (2017)

A | Appendix

A.1 Calculation of the posterior of the parameters describing deviations from GR

Here we describe the calculation of the posterior $P(\epsilon, \sigma | d)$ of the parameters (ϵ, σ) describing the fractional difference between the two independent estimates of the mass and spin of the remnant. We first make a change of variables in the joint posterior $P_I(M_f^I, a_f^I | d)$ $P_{MR}(M_f^{MR}, a_f^{MR} | d)$ from $\{M_f^I, a_f^I, M_f^{MR}, a_f^{MR}\}$ to $\{\epsilon, \sigma, \bar{M}_f, \bar{a}_f\}$ and then marginalize over \bar{M}_f and \bar{a}_f . Starting from the definitions given in Eqs. (3.2) and (3.4), we find that

$$\begin{aligned} M_f^I &= (1 + \frac{\epsilon}{2}) \bar{M}_f, & a_f^I &= (1 + \frac{\sigma}{2}) \bar{a}_f, \\ M_f^{MR} &= (1 - \frac{\epsilon}{2}) \bar{M}_f, & a_f^{MR} &= (1 - \frac{\sigma}{2}) \bar{a}_f, \end{aligned} \quad (\text{A.1})$$

so that the Jacobian of the transformation from $\{\epsilon, \sigma, \bar{M}_f, \bar{a}_f\}$ to $\{M_f^I, a_f^I, M_f^{MR}, a_f^{MR}\}$ is $\bar{M}_f \bar{a}_f$. Thus, the final expression is

$$\begin{aligned} P(\epsilon, \sigma | d) &= \int_0^1 \int_0^\infty P_I \left(\left[1 + \frac{\epsilon}{2}\right] \bar{M}_f, \left[1 + \frac{\sigma}{2}\right] \bar{a}_f | d \right) \\ &\times P_{MR} \left(\left[1 - \frac{\epsilon}{2}\right] \bar{M}_f, \left[1 - \frac{\sigma}{2}\right] \bar{a}_f | d \right) \bar{M}_f \bar{a}_f d\bar{M}_f d\bar{a}_f \end{aligned} \quad (\text{A.2})$$

A.2 Calculation of joint posterior obtained from multiple observations

We want to prove the statement:

$$P(\epsilon, \sigma | \{d_j\}) = P(\epsilon, \sigma) \prod_{j=1}^N \frac{P_j(\epsilon, \sigma | d_j)}{P_j(\epsilon, \sigma)} \quad (\text{A.3})$$

$$= \frac{1}{P^{N-1}(\epsilon, \sigma)} \prod_{j=1}^N P_j(\epsilon, \sigma | d_j) \quad (\text{A.4})$$

given that the overall prior $P(\epsilon, \sigma)$ is identical to the prior distribution $P_j(\epsilon, \sigma)$ used to compute the posterior $P_j(\epsilon, \sigma | d_j)$, which in this case is uniform in (ϵ, σ) within identical prior ranges of $(-2, 2)$.

We will try to prove a simpler case:

$$P(\epsilon | d_1, d_2) = \frac{1}{P(\epsilon)} P(\epsilon | d_1) P(\epsilon | d_2) \quad (\text{A.5})$$

consisting of two data sets, $\{d_1, d_2\}$ and a single parameter ϵ .

Bayes' Theorem:

$$P(\epsilon | d) = \frac{P(\epsilon) P(d | \epsilon)}{P(d)} \quad (\text{A.6})$$

Hence,

$$P(\epsilon | d_1, d_2) = \frac{P(\epsilon) P(d_1, d_2 | \epsilon)}{P(d_1, d_2)} \quad (\text{A.7})$$

$$= \frac{P(\epsilon) P(d_1 | \epsilon) P(d_2 | \epsilon)}{P(d_1) P(d_2)} \quad (\text{A.8})$$

$$= \frac{P(\epsilon) P(d_1 | \epsilon)}{P(d_1)} \frac{P(\epsilon) P(d_2 | \epsilon)}{P(d_2)} \frac{1}{P(\epsilon)} \quad (\text{A.9})$$

$$= \frac{1}{P(\epsilon)} P(\epsilon | d_1) P(\epsilon | d_2) \quad (\text{A.10})$$

The right-hand-side of Eq.A.10 follows from the left-hand-side *only if* Eq.A.8 follows from Eq.A.7, ie, the following two statements are true:

$$P(d_1, d_2 | \epsilon) = P(d_1 | \epsilon) P(d_2 | \epsilon) \quad (\text{A.11})$$

$$P(d_1, d_2) = P(d_1) P(d_2) \quad (\text{A.12})$$

So proving Eq.A.5 is equivalent to proving Eq.A.11-A.12.

Proving Eq.A.12: $P(d_1, d_2) = P(d_1) P(d_2)$

$$P(d_1, d_2) = P(d_1) P(d_2 | d_1) \quad (\text{A.13})$$

$$= P(d_1) P(d_2) \quad (\text{A.14})$$

The second statement is true if $P(d_2 | d_1) = P(d_2)$, which is true if d_1 and d_2 are statistically independent events. Since $\{d_1, d_2\}$ are data sets corresponding to two gravitational wave observations, the above statement will correspond to the fact that the two gravitational wave

observations were independent, i.e., the observation of the first gravitational wave event, in no way, affected the observation of the second gravitational wave event. If we assume this, then Eq.A.12 is proved correct.

Proving Eq.A.11: $P(d_1, d_2 | \epsilon) = P(d_1 | \epsilon)P(d_2 | \epsilon)$

The starting point of proving Eq.A.11 is to prove the identity:

$$P(d_1, d_2 | \epsilon) = P(d_1 | d_2, \epsilon)P(d_2 | \epsilon) \quad (\text{A.15})$$

We know:

$$P(a, b, c) = P(a, b | c)P(c) \quad (\text{A.16})$$

as well as,

$$P(a, b, c) = P(a | b, c)P(b, c) \quad (\text{A.17})$$

$$= P(a | b, c)P(b | c)P(c) \quad (\text{A.18})$$

Dividing throughout by $P(c)$ and then substituting back in Eq.A.16, we get:

$$P(a, b | c) = P(a | b, c)P(b | c) \quad (\text{A.19})$$

which is identical to Eq.A.15. $P(d_1 | d_2, \epsilon)$ defines the probability that the gravitational wave signal embedded in the data set d_1 , is described by the gravitational wave template defined by deviation parameter ϵ and another data set d_2 . However, if we make the assumption that the two gravitational wave observations were observed at different times and did not overlap at all, then the gravitational wave signal embedded in the data set d_1 , is only dependent on the deviation described through ϵ , and not on a data set corresponding to a different time. So, if we assume that the two gravitational wave signals are embedded in two non-overlapping and statistically independent stretches of interferometric data, then:

$$P(d_1 | d_2, \epsilon) = P(d_1 | \epsilon) \quad (\text{A.20})$$

and hence we prove Eq.A.11.

A.3 Definition of the Likelihood Function

The noise in a gravitational wave detector can be assumed to be a stationary ergodic Gaussian random process represented by the time series $n(t)$ ¹. We further assume that it has zero mean ($\langle n \rangle = 0$, where angular brackets represent ensemble average or expectation value) and a PSD, $S_n(f)$, which is defined as twice the Fourier transform of the *autocorrelation function* $R_n(\tau) := \langle n(t)n(t + \tau) \rangle$, as:

$$S_n(f) = 2 \int_{-\infty}^{\infty} R_n(\tau) e^{-2\pi i f \tau} d\tau \quad (\text{A.21})$$

The PSD can also be expressed in terms of the expectation value of the Fourier transform of the time series $n(t)$ as:

$$\langle \tilde{n}^*(f) \tilde{n}(f') \rangle = \frac{1}{2} S_n(f) \delta(f - f') \quad (\text{A.22})$$

where $\tilde{n}(f)$ is the Fourier transform of $n(t)$ and $\delta(f)$ is the Dirac delta function. The *coloured noise* $n(t)$ can be expressed in terms of a random process describing *white noise*, $\hat{n}(t)$ as:

$$n(t) = \int_{-\infty}^{\infty} K(t - t') \hat{n}(t') dt' \quad (\text{A.23})$$

where $K(t - t')$ is a kernel which determines the spectrum of $n(t)$. Using the convolution theorem, one can show that, in the Fourier domain, the above equation becomes:

$$\tilde{n}(f) = \tilde{K}(f) \tilde{\hat{n}}(f) \quad (\text{A.24})$$

It can also be shown that:

$$S_n(f) = |\tilde{K}(f)|^2 S_{\hat{n}} \quad (\text{A.25})$$

where $S_{\hat{n}}$ is the frequency-independent PSD of the random process $\hat{n}(t)$ (a more detailed derivation of the frequency-independent nature of $S_{\hat{n}}$ is given below). Thus, given coloured noise $n(t)$, one can obtain white noise $\hat{n}(t)$, by taking the Fourier transform of:

$$\tilde{\hat{n}}(f) = \frac{\tilde{n}(f)}{\tilde{K}(f)} = \frac{\tilde{n}(f) \sqrt{S_{\hat{n}}}}{\sqrt{S_n(f)}} \quad (\text{A.26})$$

where the second equality is obtained by substituting the expression for $\tilde{K}(f)$ from Eq.A.25. This process is called *whitening*. For the

¹ The discussion in this section is heavily influenced by the treatment presented in [54]

rest of the discussion, we work with the whitened random process, $\hat{n}(t)$. Considering an observation time T , $\hat{n}(t)$ can be assumed to be windowed signal within duration T , $0 \leq t < T$, and zero outside. If the signal is sampled at intervals of Δt , then the time series has N samples, $\hat{n}_j = \hat{n}(j\Delta t)$, $j = 0, \dots, (N-1)$, such that $N\Delta t = T$, and $1/\Delta t$ is the sampling rate. Since $\hat{n}(t)$ is Gaussian with a standard deviation say, σ and zero mean (follows from the fact that $n(t)$ had zero mean), then the underlying distribution can be written as:

$$p_{\hat{n}}(\{\hat{n}_j\}) = \left(\frac{1}{\sqrt{2\pi}\sigma} \right)^N \exp \left[-\frac{1}{2\sigma^2} \sum_{j=0}^{N-1} \hat{n}_j^2 \right] \quad (\text{A.27})$$

In the continuum limit, where $\Delta t \rightarrow 0$, for a fixed T :

$$\lim_{\Delta t \rightarrow 0} \sum_{j=0}^{N-1} \hat{n}_j^2 \Delta t = \int_0^T \hat{n}^2(t) dt \quad (\text{A.28})$$

Since the samples \hat{n}_j are independent, the autocorrelation function $R_{\hat{n}}(\tau) := \langle \hat{n}(t)\hat{n}(t+\tau) \rangle = \sigma^2\delta(\tau)$, and the PSD is:

$$S_{\hat{n}}(f) = 2 \int_{-\infty}^{\infty} R_{\hat{n}}(\tau) e^{-2\pi i f \tau} d\tau = \lim_{\Delta t \rightarrow 0} 2\sigma^2 \Delta t \quad (\text{A.29})$$

where $S_{\hat{n}}(f)$ is frequency independent and can simply be written as $S_{\hat{n}}$, a quantity that we have mentioned earlier. Thus, in Eq.A.27, one can simplify the exponential term as:

$$\lim_{\Delta t \rightarrow 0} \exp \left[-\frac{1}{2\sigma^2} \sum_{j=0}^{N-1} \hat{n}_j^2 \right] = \lim_{\Delta t \rightarrow 0} \exp \left[-\frac{1}{2\sigma^2 \Delta t} \sum_{j=0}^{N-1} \hat{n}_j^2 \Delta t \right] \quad (\text{A.30})$$

So, finally the likelihood for the white noise $\hat{n}(t)$ becomes:

$$p_{\hat{n}}[\hat{n}(t)] \propto \exp \left[-\frac{1}{S_{\hat{n}}} \int_0^T \hat{n}(t)^2 dt \right] \quad (\text{A.31})$$

A gravitational wave detector records strain data as a time series $d(t)$, which consists of noise $n(t)$ and a gravitational wave signal $h(t)$, i.e., $d(t) = h(t) + n(t)$. Thus one can rewrite the above likelihood in terms of the data and signal as:

$$p_{\hat{n}}[\hat{d}(t) - \hat{h}(t)] \propto \exp \left[-\frac{1}{S_{\hat{n}}} \int_0^T (\hat{d}(t) - \hat{h}(t))^2 dt \right] \quad (\text{A.32})$$

where $\{\hat{d}(t), \hat{h}(t)\}$ are the whitened data and template respectively. This equation can be generalised in terms of the duration $\{t_{low}, t_{high}\}$

for which the signal lasts as:

$$p_{\hat{n}}[\hat{d}(t) - \hat{h}(t)] \propto \exp \left[-\frac{1}{S_{\hat{n}}} \int_{t_{low}}^{t_{high}} (\hat{d}(t) - \hat{h}(t))^2 dt \right] \quad (\text{A.33})$$

Using this definition of the likelihood function, one proceeds to estimate the parameter set, ξ by stochastically sampling over the parameter space, using some appropriate sampler, like LALInference or emcee.

List of Figures

1.1	Gravitational wave polarisations	11
1.2	Burst source of gravitational waves	16
1.3	Spinning neutron stars as sources of gravitational waves	17
1.4	Stages of black-hole binary coalescence	20
1.5	Michelson interferometer set up	23
1.6	Sky and detector frames: relative orientations	24
1.7	Antenna pattern of an interferometric detector	26
1.8	PSD during GW150914	27
1.9	Future global gravitational wave detector network	29
1.10	Gravitational wave spectrum	34
2.1	Orbital parameters of a binary black hole system	39
2.2	Perihelion precession of Mercury around the Sun	45
2.3	Stages of black-hole binary coalescence	48
3.1	IMR consistency test on a single event	53
3.2	Distribution of SNR of Gaussian noise simulations of gravitational wave signals from binary black hole coalescences	55
3.3	IMR consistency test on simulations of GR signals in Gaussian noise	58
3.4	P-P plot of simulations of GR signals in Gaussian noise	59
3.5	Comparison of GR and modGR waveforms	60
3.6	Final mass and spin allowed by GR, and fractional differences between the final mass and spin for the kludge waveforms with $\alpha_2 = 20$, as a function of the mass ratio q .	60
3.7	Time series of the matched filter SNR, the reduced χ^2 and re-weighted SNR from an injected modified GR waveform, corresponding to the second entry in Table 3.1	63
3.8	IMR consistency test of simulations of modGR signals in Gaussian noise	64

- 3.10 Comparison of the Fourier transform of an NR waveform computed using the SPA with the exact Fourier transform computed using the Fast Fourier Transform 74
- 3.11 The evolution of instantaneous frequency, number of instantaneous cycles and SNR as a time series 75

- 4.1 The first gravitational wave observation by Advanced LIGO detectors: GW₁₅₀₉₁₄ 84
- 4.2 MAP estimate and 90% credible regions for (upperpanel) the waveform and (lower panel) the gravitational wave frequency of GW₁₅₀₉₁₄ as estimated by the LALInference analysis 85
- 4.3 IMR consistency test of GW₁₅₀₉₁₄ 86
- 4.4 IMR consistency test by combining information from GW₁₅₀₉₁₄ and GW₁₇₀₁₀₄ 89

List of Tables

3.1	Detectability of injected modGR signals using the PyCBC pipeline	62
4.1	Gravitational wave detections by the Advanced LIGO-Virgo detector network	81

B | Bibliography

- [1] <http://www.phy.olemiss.edu/~berti/qnms.html>.
- [2] <http://eob.ihef.fr>; we used the “1202” version of the code.
- [3] URL <http://www.black-holes.org/waveforms/>. SXS Gravitational Waveform Database.
- [4] Junaid Aasi, BP Abbott, Richard Abbott, Thomas Abbott, MR Abernathy, Kendall Ackley, Carl Adams, Thomas Adams, Paolo Addesso, RX Adhikari, et al. Advanced ligo. *Classical and quantum gravity*, 32(7):074001, 2015.
- [5] B. P. Abbott et al. Improved analysis of GW150914 using a fully spin-precessing waveform Model. *Phys. Rev. X*, 6(4):041014, 2016. DOI: 10.1103/PhysRevX.6.041014.
- [6] B. P. Abbott et al. GW150914: First results from the search for binary black hole coalescence with Advanced LIGO. *Phys. Rev. D*, 93(12):122003, 2016. DOI: 10.1103/PhysRevD.93.122003.
- [7] Benjamin P Abbott, R Abbott, TD Abbott, MR Abernathy, F Acernese, K Ackley, C Adams, T Adams, P Addesso, RX Adhikari, et al. Properties of the binary black hole merger gw150914. *Physical review letters*, 116(24):241102, 2016.
- [8] Benjamin P Abbott, R Abbott, TD Abbott, MR Abernathy, F Acernese, K Ackley, C Adams, T Adams, P Addesso, RX Adhikari, et al. The rate of binary black hole mergers inferred from advanced ligo observations surrounding gw150914. *The Astrophysical journal letters*, 833(1):L1, 2016.
- [9] Benjamin P Abbott, R Abbott, TD Abbott, MR Abernathy, F Acernese, K Ackley, C Adams, T Adams, P Addesso, RX Adhikari, et al. First search for gravitational waves from known

- pulsars with advanced ligo. *The Astrophysical Journal*, 839(1):12, 2017.
- [10] Benjamin P Abbott, R Abbott, TD Abbott, F Acernese, K Ackley, C Adams, T Adams, P Addesso, RX Adhikari, VB Adya, et al. Gw170817: implications for the stochastic gravitational-wave background from compact binary coalescences. *Physical review letters*, 120(9):091101, 2018.
- [11] Benjamin P Abbott et al. Binary black hole mergers in the first advanced ligo observing run. *Physical Review X*, 6(4):041015, 2016.
- [12] Benjamin P Abbott et al. Gw151226: Observation of gravitational waves from a 22-solar-mass binary black hole coalescence. *Physical Review Letters*, 116(24):241103, 2016.
- [13] Benjamin P Abbott et al. Observation of gravitational waves from a binary black hole merger. *Physical review letters*, 116(6):061102, 2016.
- [14] Benjamin P Abbott et al. Tests of general relativity with gw150914. *Physical review letters*, 116(22):221101, 2016.
- [15] Benjamin P. Abbott et al. Effects of waveform model systematics on the interpretation of GW150914. *Class. Quant. Grav.*, 34(10):104002, 2017. DOI: 10.1088/1361-6382/aa6854.
- [16] Benjamin P Abbott et al. Gw170104: Observation of a 50-solar-mass binary black hole coalescence at redshift 0.2. *Physical Review Letters*, 118:221101, 2017.
- [17] Benjamin P Abbott et al. Gw170608: Observation of a 19-solar-mass binary black hole coalescence. *arXiv:1711.05578*, 2017.
- [18] Benjamin P Abbott et al. Gw170814: A three-detector observation of gravitational waves from a binary black hole coalescence. *Physical Review Letters*, 119(14):141101, 2017.
- [19] Benjamin P Abbott et al. Gw170817: observation of gravitational waves from a binary neutron star inspiral. *Physical Review Letters*, 119(16):161101, 2017.

- [20] BP Abbott, R Abbott, TD Abbott, MR Abernathy, F Acernese, K Ackley, C Adams, T Adams, P Addesso, RX Adhikari, et al. Astrophysical implications of the binary black hole merger gw150914. *The Astrophysical Journal Letters*, 818(2):L22, 2016.
- [21] BP Abbott, R Abbott, TD Abbott, MR Abernathy, F Acernese, K Ackley, C Adams, T Adams, P Addesso, RX Adhikari, et al. Observing gravitational-wave transient gw150914 with minimal assumptions. *Physical Review D*, 93(12):122004, 2016.
- [22] BP Abbott, R Abbott, TD Abbott, MR Abernathy, F Acernese, K Ackley, C Adams, T Adams, P Addesso, RX Adhikari, et al. Gw150914: First results from the search for binary black hole coalescence with advanced ligo. *Physical Review D*, 93(12):122003, 2016.
- [23] BP Abbott, Richard Abbott, TD Abbott, MR Abernathy, Fausto Acernese, Kendall Ackley, Carl Adams, Thomas Adams, Paolo Addesso, RX Adhikari, et al. Gw150914: Implications for the stochastic gravitational-wave background from binary black holes. *Physical review letters*, 116(13):131102, 2016.
- [24] BP Abbott, R Abbott, TD Abbott, MR Abernathy, K Ackley, C Adams, P Addesso, RX Adhikari, VB Adya, C Affeldt, et al. Calibration of the advanced ligo detectors for the discovery of the binary black-hole merger gw150914. *Physical Review D*, 95(6):062003, 2017.
- [25] BP Abbott, R Abbott, TD Abbott, F Acernese, K Ackley, C Adams, T Adams, P Addesso, RX Adhikari, VB Adya, et al. Gravitational waves and gamma-rays from a binary neutron star merger: Gw170817 and grb 170817a. *The Astrophysical Journal Letters*, 848(2):L13, 2017.
- [26] BP Abbott, R Abbott, TD Abbott, F Acernese, K Ackley, C Adams, T Adams, P Addesso, RX Adhikari, VB Adya, et al. Search for post-merger gravitational waves from the remnant of the binary neutron star merger gw170817. *The Astrophysical Journal Letters*, 851(1):L16, 2017.
- [27] BP Abbott, R Abbott, TD Abbott, F Acernese, K Ackley, C Adams, T Adams, P Addesso, RX Adhikari, VB Adya, et al.

- Gw170817: Measurements of neutron star radii and equation of state. *arXiv preprint arXiv:1805.11581*, 2018.
- [28] F Acernese, M Agathos, K Agatsuma, D Aisa, N Allemandou, A Allocca, J Amarni, P Astone, G Balestri, G Ballardin, et al. Advanced virgo: a second-generation interferometric gravitational wave detector. *Classical and Quantum Gravity*, 32(2):024001, 2014.
- [29] Michalis Agathos, Walter Del Pozzo, Tjonnje G. F. Li, Chris Van Den Broeck, John Veitch, and Salvatore Vitale. TIGER: A data analysis pipeline for testing the strong-field dynamics of general relativity with gravitational wave signals from coalescing compact binaries. *Phys. Rev. D*, 89(8):082001, 2014. DOI: 10.1103/PhysRevD.89.082001.
- [30] Bruce Allen. A χ^2 time-frequency discriminator for gravitational wave detection. *Phys. Rev. D*, 71:062001, 2005. DOI: 10.1103/PhysRevD.71.062001.
- [31] Warren G Anderson, Patrick R Brady, Jolien DE Creighton, and Eanna E Flanagan. Excess power statistic for detection of burst sources of gravitational radiation. *Physical Review D*, 63(4):042003, 2001.
- [32] John W Armstrong. Low-frequency gravitational wave searches using spacecraft doppler tracking. *Living Reviews in Relativity*, 9(1):1, 2006.
- [33] KG Arun, Alessandra Buonanno, Guillaume Faye, and Evan Ochsner. Higher-order spin effects in the amplitude and phase of gravitational waveforms emitted by inspiraling compact binaries: Ready-to-use gravitational waveforms. *Physical Review D*, 79(10):104023, 2009.
- [34] Yoichi Aso, Yuta Michimura, Kentaro Somiya, Masaki Ando, Osamu Miyakawa, Takanori Sekiguchi, Daisuke Tatsumi, Hiroaki Yamamoto, KAGRA Collaboration, et al. Interferometer design of the kagra gravitational wave detector. *Physical Review D*, 88(4):043007, 2013.
- [35] Stanislav Babak, Andrea Taracchini, and Alessandra Buonanno. Validating the effective-one-body model of spin-

- ning, precessing binary black holes against numerical relativity. *Phys. Rev. D*, 95(2):024010, 2017. DOI: 10.1103/PhysRevD.95.024010.
- [36] Enrico Barausse and Thomas P. Sotiriou. Perturbed Kerr Black Holes can probe deviations from General Relativity. *Phys. Rev. Lett.*, 101:099001, 2008. DOI: 10.1103/PhysRevLett.101.099001.
- [37] James M. Bardeen, William H. Press, and Saul A Teukolsky. Rotating black holes: Locally nonrotating frames, energy extraction, and scalar synchrotron radiation. *Astrophys. J.*, 178:347, 1972. DOI: 10.1086/151796.
- [38] Emanuele Berti, Vitor Cardoso, and Andrei O. Starinets. Quasinormal modes of black holes and black branes. *Class. Quantum Grav.*, 26:163001, 2009. DOI: 10.1088/0264-9381/26/16/163001.
- [39] Swetha Bhagwat, Maria Okounkova, Stefan W Ballmer, Duncan A Brown, Matthew Giesler, Mark A Scheel, and Saul A Teukolsky. On choosing the start time of binary black hole ringdowns. *Physical Review D*, 97(10):104065, 2018.
- [40] Simeon Bird, Ilias Cholis, Julian B Munoz, Yacine Ali-Haïmoud, Marc Kamionkowski, Ely D Kovetz, Alvise Raccanelli, and Adam G Riess. Did ligo detect dark matter? *Physical review letters*, 116(20):201301, 2016.
- [41] Luc Blanchet. Gravitational radiation from post-newtonian sources and inspiralling compact binaries. *Living Reviews in Relativity*, 17(1):2, 2014.
- [42] Luc Blanchet, Thibault Damour, and Bala R Iyer. Gravitational waves from inspiralling compact binaries: Energy loss and waveform to second-post-newtonian order. *Physical Review D*, 51(10):5360, 1995.
- [43] Luc Blanchet, Thibault Damour, and Gilles Esposito-Farese. Dimensional regularization of the third post-newtonian dynamics of point particles in harmonic coordinates. *Physical Review D*, 69(12):124007, 2004.
- [44] A Bohé, M. Pürrer, M. Hannam, S. Husa, F. Ohme, P. Schmidt, et al. in preparation.

- [45] Alejandro Bohé, Guillaume Faye, Sylvain Marsat, and Edward K Porter. Quadratic-in-spin effects in the orbital dynamics and gravitational-wave energy flux of compact binaries at the 3pn order. *Classical and Quantum Gravity*, 32(19):195010, 2015.
- [46] Alessandra Buonanno, Gregory B. Cook, and Frans Pretorius. Inspiral, merger and ring-down of equal-mass black-hole binaries. *Phys. Rev. D*, 75:124018, 2007. DOI: 10.1103/PhysRevD.75.124018.
- [47] Alessandra Buonanno, Guillaume Faye, and Tanja Hinderer. Spin effects on gravitational waves from inspiraling compact binaries at second post-newtonian order. *Physical Review D*, 87(4):044009, 2013.
- [48] Miriam Cabero, Collin D Capano, Ofek Fischer-Birnholtz, Badri Krishnan, Alex B Nielsen, and Alex H Nitz. Observational tests of the black hole area increase law. *arXiv preprint arXiv:1711.09073*, 2017.
- [49] Gregorio Carullo, Laura van der Schaaf, Lionel London, Peter TH Pang, Ka Wa Tsang, Otto A Hannuksela, Jeroen Meidam, Michalis Agathos, Anuradha Samajdar, Archisman Ghosh, et al. On the empirical verification of the black hole no-hair conjecture from gravitational-wave observations. *arXiv preprint arXiv:1805.04760*, 2018.
- [50] J Casares. J. casares and pg jonker, space sci. rev. 183, 223 (2014). *Space Sci. Rev.*, 183:223, 2014.
- [51] S. Chandrasekhar and S. Detweiler. The quasi-normal modes of the schwarzschild black hole. *Proc. R. Soc. A*, 344(1639):441, 1975. DOI: 10.1098/rspa.1975.0112.
- [52] LIGO Scientific Collaboration, Virgo Collaboration, 1M2H Collaboration, Dark Energy Camera GW-EM Collaboration, DES Collaboration, DLT40 Collaboration, Las Cumbres Observatory Collaboration, VINROUGE Collaboration, MASTER Collaboration, et al. A gravitational-wave standard siren measurement of the hubble constant. *Nature*, 551(7678):85–88, 2017.

- [53] Samantha R. Cook, Andrew Gelman, and Donald B. Rubin. Validation of software for bayesian models using posterior quantiles. *J. Comp. Graph. Stat.*, 15(3):675–692, 2006. DOI: 10.1198/106186006X136976.
- [54] Jolien DE Creighton and Warren G Anderson. *Gravitational-wave physics and astronomy: An introduction to theory, experiment and data analysis*. John Wiley & Sons, 2012.
- [55] Curt Cutler and Eanna E. Flanagan. Gravitational waves from merging compact binaries: How accurately can one extract the binary’s parameters from the inspiral wave form? *Phys. Rev. D*, 49:2658–2697, 1994. DOI: 10.1103/PhysRevD.49.2658.
- [56] Curt Cutler and Kip S Thorne. An overview of gravitational-wave sources. In *General Relativity and Gravitation*, pages 72–111. World Scientific, 2002.
- [57] Thibault Damour. Coalescence of two spinning black holes: An effective one-body approach. *Physical Review D*, 64(12):124013, 2001.
- [58] Thibault Damour and Alessandro Nagar. Improved analytical description of inspiralling and coalescing black-hole binaries. *Physical Review D*, 79(8):081503, 2009.
- [59] Thibault Damour, Bala R. Iyer, and B. S. Sathyaprakash. Frequency domain P approximant filters for time truncated inspiral gravitational wave signals from compact binaries. *Phys. Rev. D*, 62:084036, 2000. DOI: 10.1103/PhysRevD.62.084036.
- [60] Thibault Damour, Alessandro Nagar, and Sebastiano Bernuzzi. Improved effective-one-body description of coalescing non-spinning black-hole binaries and its numerical-relativity completion. *Phys. Rev. D*, 87(8):084035, 2013. DOI: 10.1103/PhysRevD.87.084035.
- [61] Karsten Danzmann, LISA Study Team, et al. Lisa: Laser interferometer space antenna for gravitational wave measurements. *Classical and Quantum Gravity*, 13(11A):A247, 1996.
- [62] Gauri Sankar Datta and Trevor J Sweeting. Probability matching priors. *Handbook of statistics*, 25:91–114, 2005.

- [63] Mr C Davidson. IX. a determination of the deflection of light by the sun's gravitational field, from observations made at the total eclipse of may 29, 1919. *Phil. Trans. R. Soc. Lond. A*, 220 (571-581):291-333, 1920.
- [64] Oscar J. C. Dias, Mahdi Godazgar, and Jorge E. Santos. Linear Mode Stability of the Kerr-Newman Black Hole and Its Quasi-normal Modes. *Phys. Rev. Lett.*, 114(15):151101, 2015. DOI: 10.1103/PhysRevLett.114.151101.
- [65] Tim Dietrich, Niclas Moldenhauer, Nathan K. Johnson-McDaniel, Sebastiano Bernuzzi, Charalampos M. Markakis, Bernd Brügmann, and Wolfgang Tichy. Binary Neutron Stars with Generic Spin, Eccentricity, Mass ratio, and Compactness - Quasi-equilibrium Sequences and First Evolutions. *Phys. Rev. D*, 92(12):124007, 2015. DOI: 10.1103/PhysRevD.92.124007.
- [66] Sheila Dwyer, Daniel Sigg, Stefan W Ballmer, Lisa Barsotti, Nergis Mavalvala, and Matthew Evans. Gravitational wave detector with cosmological reach. *Physical Review D*, 91(8):082001, 2015.
- [67] Albert Einstein. Approximative integration of the field equations of gravitation. *Sitzungsber. Preuss. Akad. Wiss. Berlin (Math. Phys.)*, 1916:688-696, 1916.
- [68] Albert Einstein. Die grundlage der allgemeinen relativitätstheorie. *Annalen der Physik*, 354(7):769-822, 1916.
- [69] Albert Einstein. Über gravitationswellen. *Sitzungsberichte der Königlich Preußischen Akademie der Wissenschaften (Berlin)*, Seite 154-167., 1918.
- [70] Will M Farr, Niharika Sravan, Andrew Cantrell, Laura Kreidberg, Charles D Bailyn, Ilya Mandel, and Vicky Kalogera. The mass distribution of stellar-mass black holes. *The Astrophysical Journal*, 741(2):103, 2011.
- [71] Davide Gerosa and Christopher J. Moore. Black hole kicks as new gravitational wave observables. *Phys. Rev. Lett.*, 117(1):011101, 2016. DOI: 10.1103/PhysRevLett.117.011101.

- [72] Abhirup Ghosh, Archisman Ghosh, Nathan K Johnson-McDaniel, Chandra Kant Mishra, Parameswaran Ajith, Walter Del Pozzo, David A Nichols, Yanbei Chen, Alex B Nielsen, Christopher PL Berry, et al. Testing general relativity using golden black-hole binaries. *Physical Review D*, 94(2):021101, 2016.
- [73] Archisman Ghosh, Walter Del Pozzo, and Parameswaran Ajith. Estimating parameters of binary black holes from gravitational-wave observations of their inspiral, merger and ringdown. *Phys. Rev. D*, 94(10):104070, 2016. DOI: 10.1103/PhysRevD.94.104070.
- [74] Phil Gregory. *Bayesian Logical Data Analysis for the Physical Sciences: A Comparative Approach with Mathematica® Support*. Cambridge University Press, 2005.
- [75] Mark Hannam, Patricia Schmidt, Alejandro BohÁl, Leila Haegel, Sascha Husa, et al. A simple model of complete precessing black-hole-binary gravitational waveforms. *Phys. Rev. Lett.*, 113:151101, 2014. DOI: 10.1103/PhysRevLett.113.151101.
- [76] James Healy and Carlos O. Lousto. Remnant of binary black-hole mergers: New simulations and peak luminosity studies. *Phys. Rev. D*, 95(2):024037, 2017. DOI: 10.1103/PhysRevD.95.024037.
- [77] James Healy, Carlos O. Lousto, and Yosef Zlochower. Remnant mass, spin, and recoil from spin aligned black-hole binaries. *Phys. Rev. D*, 90(10):104004, 2014. DOI: 10.1103/PhysRevD.90.104004.
- [78] Norriss S Hetherington. Sirius b and the gravitational redshift—an historical review. *Quarterly Journal of the Royal Astronomical Society*, 21:246–252, 1980.
- [79] G Hobbs, A Archibald, Z Arzoumanian, D Backer, M Bailes, NDR Bhat, M Burgay, S Burke-Spolaor, D Champion, I Cognard, et al. The international pulsar timing array project: using pulsars as a gravitational wave detector. *Classical and Quantum Gravity*, 27(8):084013, 2010.

- [80] Fabian Hofmann, Enrico Barausse, and Luciano Rezzolla. The final spin from binary black holes in quasi-circular orbits. *Astrophys. J. Lett.*, 825(2):L19, 2016. DOI: 10.3847/2041-8205/825/2/L19.
- [81] Scott A. Hughes and Kristen Menou. Golden binaries for LISA: Robust probes of strong-field gravity. *Astrophys. J.*, 623:689, 2005. DOI: 10.1086/428826.
- [82] R. A. Hulse and J. H. Taylor. Discovery of a pulsar in a binary system. *The Astrophysical Journal*, 195:L51, jan 1975. ISSN 0004-637X. DOI: 10.1086/181708. URL <http://adsabs.harvard.edu/doi/10.1086/181708>.
- [83] RA Hulse and JH Taylor Jr. Nobel prize press release, 1993.
- [84] Sascha Husa, Sebastian Khan, Mark Hannam, Michael Pürrer, Frank Ohme, Xisco Jiménez Forteza, and Alejandro Bohé. Frequency-domain gravitational waves from nonprecessing black-hole binaries. I. New numerical waveforms and anatomy of the signal. *Phys. Rev. D*, 93(4):044006, 2016. DOI: 10.1103/PhysRevD.93.044006.
- [85] Bala Iyer, T Souradeep, CS Unnikrishnan, S Dhurandhar, S Raja, A Sengupta, IndIGO Consortium, et al. Ligo-india. *Report No. LIGO-M1100296 (Indian Initiative in Gravitational-wave Observations, 2011)*, 2011.
- [86] Xisco Jiménez-Forteza, David Keitel, Sascha Husa, Mark Hannam, Sebastian Khan, and Michael Pürrer. Hierarchical data-driven approach to fitting numerical relativity data for nonprecessing binary black holes with an application to final spin and radiated energy. *Phys. Rev. D*, 95(6):064024, 2017. DOI: 10.1103/PhysRevD.95.064024.
- [87] N. K. Johnson-McDaniel, A. Gupta, P. Ajith, D. Keitel, O. Birnholtz, F. Ohme, and S. Husa. Determining the final spin of a binary black hole system including in-plane spins: Method and checks of accuracy. Technical Report LIGO-T1600168, 2016. <https://dcc.ligo.org/LIGO-T1600168/public>.
- [88] Sebastian Khan, Sascha Husa, Mark Hannam, Frank Ohme, Michael Pürrer, Xisco Jiménez Forteza, and Alejandro Bohé.

- Frequency-domain gravitational waves from nonprecessing black-hole binaries. II. A phenomenological model for the advanced detector era. *Phys. Rev. D*, 93(4):044007, 2016. DOI: 10.1103/PhysRevD.93.044007.
- [89] A. Krolak and Bernard F. Schutz. Coalescing binaries — Probe of the universe. *Gen. Rel. Grav.*, 19:1163–1171, 1987. DOI: 10.1007/BF00759095.
- [90] Lionel London, Sebastian Khan, Edward Fauchon-Jones, Xisco Jiménez Forteza, Mark Hannam, Sascha Husa, Chinmay Kalaghatgi, Frank Ohme, and Francesco Pannarale. First higher-multipole model of spinning binary-black-hole gravitational waveforms. 2017.
- [91] Michele Maggiore. *Gravitational Waves: Volume 1: Theory and Experiments*, volume 1. Oxford university press, 2008.
- [92] Paolo Maraner. The effect of rotations on michelson interferometers. *Annals of Physics*, 350:95–104, 2014.
- [93] Saeed Mirshekari, Nicolás Yunes, and Clifford M Will. Constraining lorentz-violating, modified dispersion relations with gravitational waves. *Physical Review D*, 85(2):024041, 2012.
- [94] Chandra Kant Mishra, K. G. Arun, Bala R. Iyer, and B. S. Sathyaprakash. Parametrized tests of post-Newtonian theory using Advanced LIGO and Einstein Telescope. *Phys. Rev. D*, 82:064010, 2010. DOI: 10.1103/PhysRevD.82.064010.
- [95] Abdul H. Mroué et al. A catalog of 174 binary black-hole simulations for gravitational-wave astronomy. *Phys. Rev. Lett.*, 111:241104, 2013. DOI: 10.1103/PhysRevLett.111.241104.
- [96] Hiroyuki Nakano, Takahiro Tanaka, and Takashi Nakamura. Possible golden events for ringdown gravitational waves. *Phys. Rev. D*, 92(6):064003, 2015. DOI: 10.1103/PhysRevD.92.064003.
- [97] Feryal Özel, Dimitrios Psaltis, Ramesh Narayan, and Jeffrey E McClintock. The black hole mass distribution in the galaxy. *The Astrophysical Journal*, 725(2):1918, 2010.
- [98] Yi Pan, Alessandra Buonanno, Michael Boyle, Luisa T. Buchman, Lawrence E. Kidder, et al. Inspiral-merger-ringdown

- multipolar waveforms of nonspinning black-hole binaries using the effective-one-body formalism. *Phys. Rev. D*, 84:124052, 2011. DOI: 10.1103/PhysRevD.84.124052.
- [99] Yi Pan, Alessandra Buonanno, Andrea Taracchini, Lawrence E. Kidder, Abdul H. Mroué, Harald P. Pfeiffer, Mark A. Scheel, and Béla Szilágyi. Inspiral-merger-ringdown waveforms of spinning, precessing black-hole binaries in the effective-one-body formalism. *Phys. Rev. D*, 89(8):084006, 2014. DOI: 10.1103/PhysRevD.89.084006.
- [100] E. Poisson. *A relativist's toolkit : the mathematics of black-hole mechanics*. Cambridge University Press, Cambridge, UK, 2004.
- [101] Eric Poisson. Gravitational waves from inspiraling compact binaries: The quadrupole-moment term. *Physical Review D*, 57(8):5287, 1998.
- [102] Robert V Pound and Glen A Rebka Jr. Gravitational red-shift in nuclear resonance. *Physical Review Letters*, 3(9):439, 1959.
- [103] Robert V Pound and JL Snider. Effect of gravity on nuclear resonance. *Physical Review Letters*, 13(18):539, 1964.
- [104] W. H. Press. Long Wave Trains of Gravitational Waves from a Vibrating Black Hole. *Astrophys. J.*, 170:L105, December 1971. DOI: 10.1086/180849.
- [105] M Punturo, M Abernathy, F Acernese, B Allen, Nils Andersson, K Arun, F Barone, B Barr, M Barsuglia, M Beker, et al. The einstein telescope: a third-generation gravitational wave observatory. *Classical and Quantum Gravity*, 27(19):194002, 2010.
- [106] Michael Pürrer. Frequency domain reduced order model of aligned-spin effective-one-body waveforms with generic mass-ratios and spins. *Phys. Rev. D*, 93(6):064041, 2016. DOI: 10.1103/PhysRevD.93.064041.
- [107] A Samajdar et al. *In Preparation*, 2018.
- [108] Anuradha Samajdar and KG Arun. Projected constraints on the dispersion of gravitational waves using advanced ground- and space-based interferometers. *Physical Review D*, 96(10):104027, 2017.

- [109] B.S. Sathyaprakash and B.F. Schutz. Physics, Astrophysics and Cosmology with Gravitational Waves. *Living Rev. Relat.*, 12:2, 2009.
- [110] Patricia Schmidt, Mark Hannam, and Sascha Husa. Towards models of gravitational waveforms from generic binaries: A simple approximate mapping between precessing and non-precessing inspiral signals. *Phys. Rev. D*, 86:104063, 2012. DOI: 10.1103/PhysRevD.86.104063.
- [111] Patricia Schmidt, Ian W. Harry, and Harald P. Pfeiffer. Numerical Relativity Injection Infrastructure. 2017.
- [112] Bernard Schutz. *A first course in general relativity*. Cambridge university press, 2009.
- [113] Bernard F Schutz. Determining the hubble constant from gravitational wave observations. *Nature*, 323(6086):310, 1986.
- [114] D. H. Shoemaker. Advanced LIGO anticipated sensitivity curves. Technical Report LIGO-T0900288, 2010. <https://dcc.ligo.org/LIGO-T0900288/public>.
- [115] John Skilling et al. Nested sampling for general bayesian computation. *Bayesian analysis*, 1(4):833–859, 2006.
- [116] Leo C. Stein and Nicolas Yunes. Effective Gravitational Wave Stress-energy Tensor in Alternative Theories of Gravity. *Phys. Rev. D*, 83:064038, 2011. DOI: 10.1103/PhysRevD.83.064038.
- [117] Andrea Taracchini et al. Effective-one-body model for black-hole binaries with generic mass ratios and spins. *Phys. Rev. D*, 89(6):061502(R), 2014. DOI: 10.1103/PhysRevD.89.061502.
- [118] Joseph H Taylor and Joel M Weisberg. Further experimental tests of relativistic gravity using the binary pulsar psr 1913+16. *The Astrophysical Journal*, 345:434–450, 1989.
- [119] Matt Taylor, David Cinabro, Ben Dilday, Lluís Galbany, Ravi R Gupta, R Kessler, John Marriner, Robert C Nichol, Michael Richmond, Donald P Schneider, et al. The core collapse supernova rate from the sdss-ii supernova survey. *The Astrophysical Journal*, 792(2):135, 2014.

- [120] KIMIO Tsubono. 300-m laser interferometer gravitational wave detector (tama300) in japan. In *First Edoardo Amaldi conference on gravitational wave experiments*, pages 112–114. World Scientific, 1995.
- [121] CS Unnikrishnan. Indigo and ligo-india: Scope and plans for gravitational wave research and precision metrology in india. *International Journal of Modern Physics D*, 22(01):1341010, 2013.
- [122] Samantha A. Usman et al. The PyCBC search for gravitational waves from compact binary coalescence. *Class. Quantum Grav.*, 33(21):215004, 2016. DOI: 10.1088/0264-9381/33/21/215004.
- [123] Vijay Varma and Parameswaran Ajith. Effects of non-quadrupole modes in the detection and parameter estimation of black hole binaries with nonprecessing spins. 2016.
- [124] J. Veitch et al. Parameter estimation for compact binaries with ground-based gravitational-wave observations using the LAL-Inference software library. *Phys. Rev. D*, 91(4):042003, February 2015. DOI: 10.1103/PhysRevD.91.042003.
- [125] Robert FC Vessot, Martin W Levine, Edward M Mattison, EL Blomberg, TE Hoffman, GU Nystrom, BF Farrel, Rudolph Decher, Peter B Eby, CR Baugher, et al. Test of relativistic gravitation with a space-borne hydrogen maser. *Physical Review Letters*, 45(26):2081, 1980.
- [126] C. V. Vishveshwara. Scattering of Gravitational Radiation by a Schwarzschild Black-hole. *Nature (London)*, 227:936, August 1970. DOI: 10.1038/227936a0.
- [127] CV Vishveshwara. Scattering of gravitational radiation by a schwarzschild black-hole. *Nature*, 227(5261):936, 1970.
- [128] Joseph Weber. Detection and generation of gravitational waves. *Physical Review*, 117(1):306, 1960.
- [129] S Weinberg. Gravitation and cosmology. ed. John Wiley and Sons, New York, 1972.
- [130] Joel M Weisberg and Joseph H Taylor. Relativistic binary pulsar b1913+ 16: Thirty years of observations and analysis. *arXiv preprint astro-ph/0407149*, 2004.

- [131] Joel M Weisberg, Joseph H Taylor, and Lee A Fowler. Gravitational waves from an orbiting pulsar. *Scientific American*, 245(4):74–83, 1981.
- [132] Joel M Weisberg, David J Nice, and Joseph H Taylor. Timing measurements of the relativistic binary pulsar psr b1913+ 16. *The Astrophysical Journal*, 722(2):1030, 2010.
- [133] Norbert Wex. Testing relativistic gravity with radio pulsars. *arXiv preprint arXiv:1402.5594*, 2014.
- [134] Clifford M. Will. Bounding the mass of the graviton using gravitational wave observations of inspiralling compact binaries. *Phys. Rev. D*, 57:2061, 1998. DOI: 10.1103/PhysRevD.57.2061.
- [135] Benno Willke, P Ajith, B Allen, P Aufmuth, C Aulbert, S Babak, Ramachandran Balasubramanian, BW Barr, S Berukoff, A Bunkowski, et al. The geo-hf project. *Classical and Quantum Gravity*, 23(8):S207, 2006.
- [136] Kent Yagi, Norihiro Tanahashi, and Takahiro Tanaka. Probing the size of extra dimensions with gravitational wave astronomy. *Physical Review D*, 83(8):084036, 2011.
- [137] Nicolas Yunes and Frans Pretorius. Fundamental theoretical bias in gravitational wave astrophysics and the parametrized post-einsteinian framework. *Phys. Rev. D*, 80(12):122003, 2009. DOI: 10.1103/PhysRevD.80.122003.